UPPSALA
UNIVERSITET

Digital Comprehensive Summaries of Uppsala Dissertations from the Faculty of Science and Technology 303

Ordering in Crystalline Short-Chain Polymer Electrolytes

ANTI LIIVAT

ACTA
UNIVERSITATIS
UPSALIENSIS
UPPSALA
2007

ISSN 1651-6214
ISBN 978-91-554-6885-9
urn:nbn:se:uu:diva-7853

Dissertation presented at Uppsala University to be publicly examined in Häggsalen, Ångström Laboratory, Lägerhyddsvägen 1, Uppsala, Friday, May 11, 2007 at 10:15 for the degree of Doctor of Philosophy. The examination will be conducted in English.

Abstract

Liivat, A. 2007. Ordering in Crystalline Short-Chain Polymer Electrolytes. Acta Universitatis Upsaliensis. *Digital Comprehensive Summaries of Uppsala Dissertations from the Faculty of Science and Technology* 303. 50 pp. Uppsala. ISBN 978-91-554-6885-9.

Polymer electrolytes are the most obvious candidates for safe "all-solid" Li-ion batteries and other electrochemical devices. However, they still have relatively poor ionic conductivities, which limits their wider adoption in commercial applications. It has earlier been the conventional wisdom that only amorphous phases of polymer electrolytes show usefully high ionic conduction, while crystalline forms are insulators. However, this has been challenged in the last decade by the discovery of highly organized, low-dimensional ion-conducting materials. Specifically, the crystalline phases of $LiXF_6.PEO_6$ exhibit higher ionic conductivities than their amorphous counterparts, with the Li-ion conduction taking place along the PEO channels. Polymer chain-length and chain-end registry has emerged as potentially significant in determining ionic conduction in these materials.

Molecular Dynamics simulations have therefore been made of short-chain, monodisperse (M_w~1000), methoxy end-capped $LiPF_6.PEO_6$ to examine relationships between ion conduction and mode of chain-ordering. Studies of smectic and nematic arrangements of PEO chains have revealed that ion-transport mechanisms within the smectic planes formed by cooperative chain-end registry appear to be more suppressed by ion-pairing than in-channel conduction. Disorder phenomena in the chain-end regions emerge as a critical factor in promoting Li-ion migration across chain-gaps, as does the structural continuity of the PEO channels.

Simulations incorporating ~1% aliovalent SiF_6^{2-} dopants further suggest an increase in Li-ion conduction when the extra Li-ions reside within the PEO channels, with the anion influencing charge-carrier concentration through enhanced ion-pair formation.

XRD techniques alone are shown to be inadequate in ascertaining the significance of the various short-chain models proposed; atomistic modelling is clearly a helpful complement in distinguishing more or less favourable situations for ion conduction.

Though providing valuable insights, it must be concluded that this work has hardly brought us significantly closer to breakthroughs in polymer electrolyte design; the critical factors which will make this possible remain as yet obscure.

Keywords: polymer electrolytes, molecular dynamics, ionic conductivity, crystalline ordering, polymer chain length, smectic, nematic

Anti Liivat, Department of Materials Chemistry, Box 538, Uppsala University, SE-75121 Uppsala, Sweden

ISSN 1651-6214
ISBN 978-91-554-6885-9
urn:nbn:se:uu:diva-7853 (http://urn.kb.se/resolve?urn=urn:nbn:se:uu:diva-7853)

List of Papers

This thesis is a summary based on the following papers, which are referred to in the text by their Roman numerals:

I. **Development of a force-field for Li_2SiF_6**
A. Liivat, A. Aabloo and J.O. Thomas, *J. Comput. Chem.,* **26** (2005) 716-724.

II. **Molecular dynamics simulation of the crystalline short-chain polymer system $LiPF_6{\cdot}PEO_6$ (M_w~1000)**
D. Brandell, A. Liivat, A. Aabloo and J.O. Thomas, *J. Mater. Chem.,* **15** (2005) 4338-4345.

III. **A molecular dynamics study of short-chain ordering in crystalline $LiPF_6{\cdot}PEO_6$**
A. Liivat, D. Brandell, A. Aabloo and J.O. Thomas, Submitted to *Electrochim. Acta*.

IV. **A molecular dynamics study of ion conduction mechanisms in crystalline low-M_w $LiPF_6{\cdot}PEO_6$**
A. Liivat, D. Brandell and J.O. Thomas, Submitted to *J. Mater. Chem.*

Some comments on my own contribution to this work:

Papers I, III and IV: The majority of the work in all its phases.

Paper II: A significant part of the project planning, model preparation and data analysis.

Thesis: I was helped with the writing of the *Populärvetenskaplig Sammanfattning* by my supervisor Dr. Daniel Brandell.

Other papers not included in this thesis:

Molecular dynamics simulation of the $LiPF_6 \cdot PEO_6$ structure
D. Brandell, A. Liivat, H. Kasemägi, A. Aabloo and J.O. Thomas,
J. Mater. Chem., **15** (2005) 1422.

Conduction mechanisms in crystalline $LiPF_6 \cdot PEO_6$ doped with SiF_6^{2-} and SF_6
D. Brandell, A. Liivat, A. Aabloo and J.O. Thomas,
Chem. Mater., **17** (2005) 3673.

Molecular dynamics simulations of Li- and Na-Nafion membranes
D. Brandell, A. Ainla, A. Liivat and A. Aabloo,
Proc. SPIE Int. Soc. Opt. Eng., **6168** (2006) 61680G.

Molecular dynamics studies of the Nafion®, Dow® and Aciplex® fuel-cell polymer membrane systems
D. Brandell, J. Karo, A. Liivat and J.O. Thomas,
Submitted to *Journal of Molecular Modeling.*

Contents

Abbreviations

ADF	Atomic Displacement Factors
CN	Coordination Number
EO	Ethylene Oxide
HF	Hartree-Fock theory
MD	Molecular Dynamics
MP2	Møller-Plesset second-order perturbation theory
M_w	Molecular Weight
NMR	Nuclear Magnetic Resonance
PEO	Poly(Ethylene Oxide)
PE	Polymer Electrolyte
RDF	Radial Distribution Function
TFSI	*bis*-(TriFluoroMethylSulphonyl)Imide

Introduction

A weak link in energy storage technologies

Electrical energy is the most universal form of energy used today because it can be readily converted to other usable forms. Electrical energy now represents *ca.* 13 % [1] of the total energy consumption in the World, with power plants supplying stationary locations with electricity through their distribution networks. A somewhat overlooked but critical contribution in the development of this technology was made by the English scientist Stephen Gray, who invented electrically conducting wire in 1729.

It took until 1799 and the invention of the first battery by Alessandro Volta for the importance of a "closed circuit" to emerge [2]. This evolution peaked with Michael Faraday's discovery of the solid ion conductors (PbF_2) in 1839 [3] – "ion-conducting wire" or *solid electrolytes*. The significance of this discovery resurfaced during recent decades with the rapid development of portable electronics, which has shaped the lifestyle of a whole generation. This has led to the parallel development of small and medium-size batteries to supply this wide diversity of electronic equipment with safe portable power. While energy densities of the best Li-ion based batteries are today high enough for most applications, and the prospect of reducing the price of the materials involved is promising [4], the batteries still contain volatile (unsafe) liquid or gel-type electrolytes. This is a result of the poor ionic conductivity and mechanical brittleness of known dry solid electrolytes, which makes "all solid" wiring in batteries still a challenging task. This, indeed, remains the weak link in electrochemical energy storage technologies.

Polymer electrolytes

Polymer-based materials are the most obvious battery electrolytes by virtue of their mechanical strength combined with elasticity, making them easily formable to any desired shape. In principle, polymers offer unlimited possibilities in functionality, while still being a cost effective solution. A small subset has been found to solvate salts such as $LiPF_6$, $LiClO_4$, $LiBF_4$, Li-*bis*(trifluoromethylsulphonyl)imide ("Li-TFSI"), *etc.*; salts which are used in

today's Li-ion batteries and show usable Li-ion conductivity. The most prominent polymer host for alkaline ion salts is Poly(Ethylene Oxide) (PEO) – a polymer with repeat unit –(CH_2-CH_2-O)- [5].

Ion conductivity in PEO-based polymers was discovered by Wright in 1973 [6], and their potential for use in "all-solid-state" batteries was later proposed by Armand in 1979 [7]. In fact, this property of PEO actually dates back to the 1960's, when Pedersen discovered that crown-ethers – a ring-like relative of PEO – could form complexes with alkali ions. For this and related supramolecular discoveries, Pedersen, Cram and Lehn were awarded the Nobel Prize in Chemistry in 1987.

Evidence was found in the early 1980's to suggest the importance of polymer segmental motion in driving ion transport and making the amorphous phase more favourable than the crystalline for ion conduction [8,9]. Since the intrinsic conductivity of PEO-Li salts at room temperature is rather low ($\approx 10^{-7}$ S/cm) due to their high degree of crystallinity, the main research effort has focussed on promoting the amorphous phase [10,11].

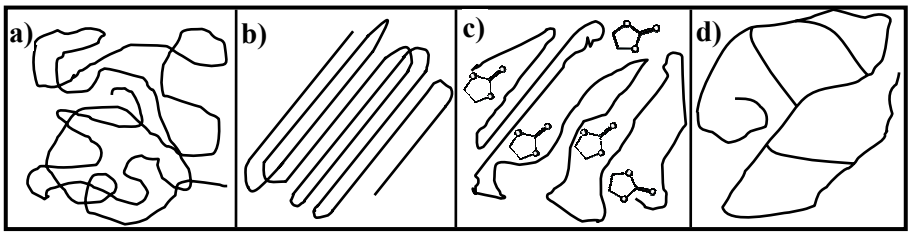

Figure 1 Schematic representations of a) amorphous, b) crystalline, c) plasticized and d) cross-linked PEO-salt complexes.

Several routes have been successful in this context: chain cross-linking, incorporating small plasticizing molecules [5] or inorganic nanoparticles [12] (see *Fig. 1*). Room temperature conductivity has been brought above 10^{-5} S/cm which is, nevertheless, still lower than what is considered a minimal requirement for battery applications: 10^{-3} S/cm. Moreover, ion-pairing and anionic transport further reduce the performance of polymer electrolytes. At this point, the research field needs to move in some new direction.

Ordering in polymer electrolytes

Paradoxically, the highest room-temperature Li-ion conductivities are seen in crystalline ceramics, like the perovskite $Li_{0.34}La_{0.51}TiO_{2.94}$ [13] or Li-β-alumina [14], where it reaches 10^{-3} S/cm. This has been attributed to the high concentration of available sites and low migration barriers [15]. Rotator

phases exhibiting “paddle-wheel” type promotion of ion conduction have also been seen to give much higher ionic conductivities in inorganic materials, but only at greatly elevated temperatures [16]. This has inspired the research community to seek to design polymer structures that provide analogous low-energy pathways for Li-ions.

To this end, Wright *et al.* have synthesized and characterized two-dimensional smectic liquid crystals to overcome the underlying problems of amorphous polymer electrolytes. The molecules involved in these crystals comprise oligo-ethoxy fragments attached to alkyl chains. The latter order locally and confine the Li-ions to planes of compressed oligo-ethoxy loops, where conduction pathways are created. The relaxation of oligo-ethoxy fragments is inhibited and coordination to cations is weakened. Conductivities as high as 10^{-3} S/cm at 20 °C have been reported. [17-20].

In a similar fashion, Armand *et al.* have studied the Li-ion conductivity in PEO together with anions with attached aliphatic side-chains, and found an enhancement effect on conductivity [21]. Interestingly, conductivity increases by an order of magnitude have been reported for several PEO-salt complexes when mechanically stretched. This has been attributed to the alignment of crystallites in the partially crystalline material [22].

In known crystalline PEO/Li-salt complexes with EO:Li ratios from 1:1 to 4:1 [23], each cation is coordinated by only one helical PEO chain in such a way that there are no vacancies available into which Li-ions can migrate without forming ion-pairs. However, the discovery of new crystalline phases of $LiXF_6{\cdot}PEO_6$ (for X = P, As or Sb) [24,25] with conductivities higher than their amorphous counterparts raised questions as to the basis of the conductivity mechanism in these materials [26,27]. Diffraction studies could show that the polymer forms hemi-helices, which arrange pair-wise to form cylindrical channels for the Li-ions, while the anions are situated outside these channels [24,25]; see *Fig. 2*.

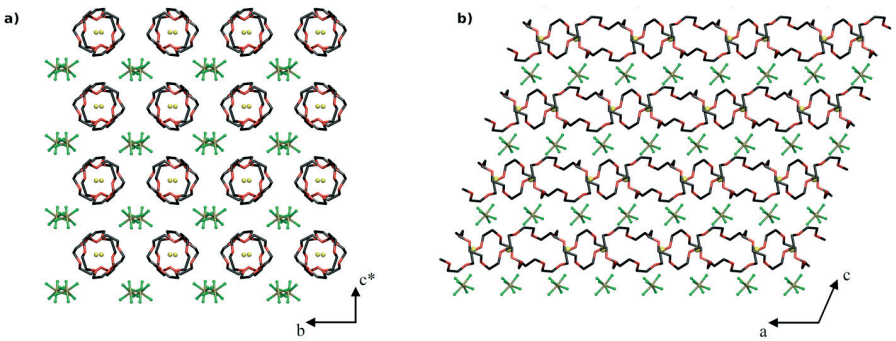

Figure 2 The structure of crystalline $LiPF_6{\bullet}PEO_6$ viewed a) along the polymer channel axis, showing Li ions inside the channels and PF_6^- ions outside, and b) along the unique monoclinic axis perpendicular to the channels, showing the anion and cation positions and chain configuration

NMR measurements suggest the ion conductivity to be dominated by *cation* transport; *i.e.,* t_+ is close to unity [26]. Conductivity is shown to be enhanced through doping with the larger isovalent anion $N(SO_2CF_3)_2^-$ [28] or with the aliovalent anion SiF_6^{2-} [29] to give conductivities on a par with the very best amorphous PEO-Li electrolytes.

Short-chain $LiPF_6{\cdot}PEO_6$ crystal structures

The majority of experimental structure work and especially conductivity studies has been performed using fairly short methoxy end-capped polymer chains, typically with average M_w in the range 1000–2000. These chain-lengths are below the entanglement limit of *ca.* 3200 for PEO, and introduce a significant concentration of chain-end defects into the structure. Nevertheless, powder XRD studies show that $LiXF_6{\cdot}PEO_6$ crystals prepared from high-M_w PEO (M_w=100000) and from short-chain PEO were isostructural [25], with even higher crystallinity observed in the short-chain structures. This situation implies directional alignment of the short chains, as shown in *Fig. 3*.

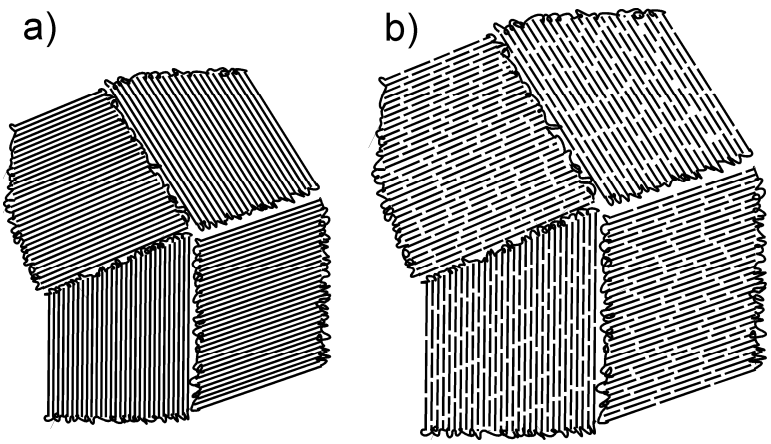

Figure 3 Schematic representations of crystallites formed by (a) a long-chain polymer (chain-length>>crystallite size), and (b) a short-chain polymer (chain-length <<crystallite size).

An increase in ionic conductivity by two orders of magnitude on decreasing the molecular weight of PEO from 2000 to 1000 in crystalline phases of $LiPF_6{\cdot}PEO_6$ has also been reported. This phenomenon was attributed to the increase in crystallite size, thereby facilitating longer pathways for ion transport and lower grain-boundary resistance (shown in *Fig. 3*) [30]. However, the experimental evidence to support this increase in crystallite size (from 200 to 250 nm) on decreasing the M_w of the PEO chains from 2000 to 1000 was based on peak-width analysis (using the Scherrer equation) of a single

XRD peak – the (0 2 1) reflection [30]. Since this reflection is insensitive to crystallite size along the *a*-axis, which is the direction of the PEO channels (see *Fig. 2*), all this tells us is that crystallite size increases slightly in directions perpendicular to the PEO channels. This situation can imply the possible existence of ion-conduction pathways perpendicular to PEO channel axis, as will be discussed below.

In a recent paper [31], Bruce *et al.* specifically address the question of chain-end ordering when interpreting XRD and impedance spectroscopy data for crystalline systems containing mono- and polydisperse methoxy-capped (M_w ~1000) PEO chains. They attribute the lower observed ionic conductivity in the monodisperse system to a more ordered distribution of end-groups [31]; such order is clearly unfeasible in polydisperse systems. It has therefore now become relevant to consider the effect of increasing the concentration of chain-end defects (see *Fig. 4*) as we go to short-chain PEO-salt systems.

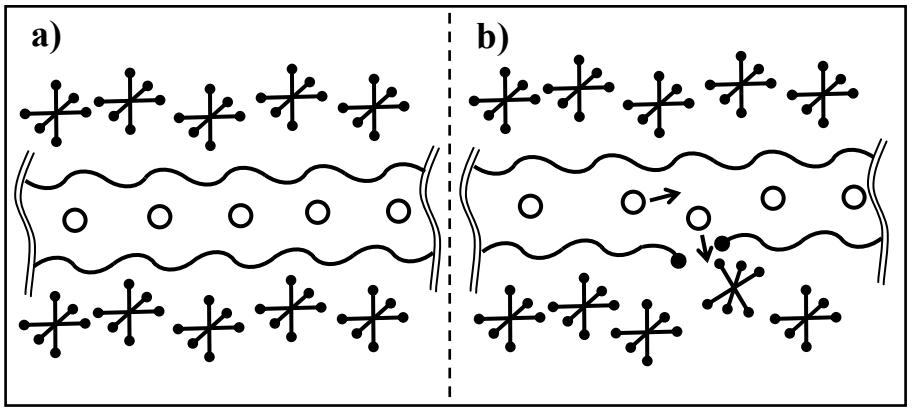

Figure 4 A schematic representation of a PEO channel fragment in infinite (a) and short-chain (b) systems; anions occupy the space between the polymer channels and Li-ions (circles) occupy the channels.

Computer simulation of the crystalline polymer electrolytes

Developments in computational resources and software have made it possible to model the structure and dynamics of PEO-based polymer electrolytes at the atomic level; see [32-34] and references therein. This has helped to elucidate the mechanisms of ion transport [35,36] using Molecular Dynamics (MD) simulation methods. More demanding quantum mechanical

calculations have also been used to map the energy landscape of polymer conformations and polymer interaction with ions [37-41], and to design polymer-salt additives in a systematic manner [42]. Of these studies, few have addressed crystalline systems, such as PEO_3.NaI [43]. This is partially due to lack of structural information for crystals that can be potentially good ion-conductors, but can also be a result of the unavailability of the relevant interatomic force-fields.

The crystal structure determinations of $LiXF_6 \cdot PEO_6$ (for X = P, As or Sb) [24, 25] facilitate the computation of activation energies [44], and the simulation of structural and dynamical properties for $LiPF_6 \cdot PEO_6$ [45]. This present thesis focuses on fundamental questions relating to the structural and dynamical properties of the crystalline phases of these $LiXF_6 \cdot PEO_6$ crystals, involving short-chain PEO (M_w~1000) polymers. Chain-ordering and the effect of aliovalent doping with SiF_6^{2-} are both addressed at the atomic level by MD methods. Identification of charge-carriers and of likely pathways for ion migration are also discussed. The content of the four papers summarized in this thesis is as follows:

Paper **I**: Force-field development for potential Li-ion donor dopant Li_2SiF_6, for use in crystalline polymer electrolytes. The ability of the force-field to predict the crystal structure for Li_2SiF_6 on the basis of available experimental information on isostructural Na_2SiF_6 was tested.

Paper **II**: Smectic and nematic arrangements of a short-chain (n=22, methoxy-terminated) $LiPF_6 \cdot PEO_{5.75}$ system are compared with the long-chain system studied earlier. These systems show *ca.* 50% ion-pairing, increased dynamics and disorder, resulting in the loss of crystallographic periodicity but maintained PEO/Li channel structure, although the channel-ends misalign near the smectic interface.

Paper **III**: The stoichiometric short-chain (n=23) $LiPF_6 \cdot PEO_6$ structure was studied in 5 different possible arrangements to assess the most likely situations in a real material. All 5 models resemble more the infinite structures than the n=22 systems of Paper **II**. An important factor emerges: Li-ion coordination in the chain-defect regions determines local order and dynamics; short PEO channels of smectically aligned PEO chains are quasi-continuous in the presence of cross-linking Li-ions.

Paper **IV**: Ion conduction in the three most realistic models taken from Paper **III** was studied under an applied external electric field. The systems ranked in order of ion conductivity are: *nematic-R* > *nematic-B* > *smectic-B*; ordering of the chain-ends in these systems follows the reverse order, with *nematic-R* the most disordered. Conductivity within the smectic plane is lower than along the channels and is hindered by ion-pairing.

Methodology

Molecular dynamics simulations

The Molecular Dynamics (MD) simulation technique involves the routine integration of Newton's classical equations of motion for a many-atom system. If this is done sequentially at sufficiently short time-intervals, the procedure should result in a complete history of atomic trajectories over a limited time period. The interatomic forces are described by simple analytical functions (the force-field) involving parameters evaluated empirically or from quantum mechanical calculations (see the next section). MD simulations of an infinite solid system use periodic boundary conditions and an Ewald summation routine to treat long-range electrostatic forces [46].

Specific details of the performed simulations are as follows: the short-range cut-off used is 16 Å and the Verlet sphere used in the construction of the Verlet neighbour-list has a 0.5 Å radius. A NVT Nose-Hoover thermostat is used with a temperature relaxation time of 0.1ps. Longer relaxation times were tested but led to increased temperature fluctuations. Additionally, to allow the MD-box size to vary, simulations were run with a constant anisotropic pressure (NσT Nose-Hoover) thermostat with a corresponding relaxation time of 0.3ps (Paper **III)**; the short-range cut-off was then reduced to 15 Å. A multiple time-step technique was used, with a longer time-step of 0.5 fs at longer distances and a shorter time-step of 0.1 fs inside a sphere of radius 6 Å.

The simulation temperature was 293K, except for the external electric field studies in Paper **IV**, where the temperature was set to 328K (to match the experimental temperature used in [29]). A constant volume ensemble (NVT) was used for 1 ns, followed by a constant anisotropic pressure (NσT) simulation for 1ns. Trajectory data were sampled at 0.1ps intervals for subsequent analysis. A parallelized simulation program DL_POLY: Version 2.14 was used [47]. Applications of this program are reviewed in [48] for a variety of problem types.

Force field

The potential functions involved in the applied force-fields are listed in the **Appendix**. All inter- and intramolecular force-field parameters for PEO were taken from Neyertz *et al.* [49], except for the bond-stretching and methyl-group rotation potentials; these are taken from Jaffe *et al.* [50] and Borodin *et al.* [51], respectively. The set of PEO potentials was developed originally by Gejji *et al*. [38] from MP2/6-311++G**//HF/3-21G energy minimisation of the diglyme system and was validated for crystalline PEO [49], $NaI{\cdot}PEO_3$ [43], a PEO surface [52-54], and for various amorphous polymer electrolytes [55-63].

The parameters for the interaction of PEO, Li^+ and PF_6^- are taken from [39,64], while those involving an aliovalent dopant SiF_6^{2-} have been developed in Paper **I** and are given in *Table A-I* of the **Appendix**. In these potentials, an averaged polarisation contribution to the total energy has been taken into account by introducing a polarization term (with parameter D). These potentials were also tested in the simulation of the crystal structure of Li_2SiF_6 (see Paper **I**). Standard Lorentz-Berthelot combination rules were used to obtain force-field parameters for the interactions of PEO with the dopant [65].

Starting structures

The starting structures in the MD simulation boxes comprise 4 × 2 × 4 unit cells of crystalline $LiPF_6{\cdot}PEO_6$ [25] (see *Fig. 1*), with dimensions: a = 46.928 Å, b = 34.750 Å, c = 34.768 Å, β = 107.8°, involving 32 PEO hemihelices of CH_3-$(OCH_2CH_2)_n$-OCH_3, along with 128 $LiPF_6$ units.

The starting structures used in Paper **II** (n=22) and in Papers **III** and **IV** (n=23) were generated from the asymmetric unit resulting from the neutron diffraction study [25], with no internal symmetry conditions imposed within the periodic simulation box. Terminal methyl groups were incorporated either by removing one EO unit (Paper **II**) or breaking a C-C bond (Papers **III** and **IV**) in the chain and attaching an extra hydrogen atoms to each end-carbon, with the H-C-H angles constrained to 109.45° and C-H distances to 1.1 Å. Both CH_3-groups were constrained to preserve (C_{3v}) symmetry, and rotated about the C-O and O-C_{meth} bonds using a Monte-Carlo procedure to arrive at an orientation free from steric hindrance. In Paper **II**, the removal of ether oxygens using this method resulted in an effective formula

$LiPF_6 \cdot PEO_{5.75}$ and a lowering of the density by 2.5%. This was chosen as a compromise to provide space for the end-groups to redistribute, and corresponds to the average molecular weight of PEO used in the experimental studies [30,31]. Two models were generated with n=22, representing ordered and disordered extremes in the spatial distributions of the methoxy end-groups:

- In the *smectic* model (*Fig. 5*, left), all end-groups were initially situated in a single plane perpendicular to the polymer-chain direction.
- In the *nematic* arrangement (*Fig. 5*, right), one of each pair of hemi-helices in the smectic model was shifted by one crystallographic asymmetric unit (6 EO-units) in the positive or negative helical direction with respect to its hemi-helical partner, thus creating a system without chain-end pairs.

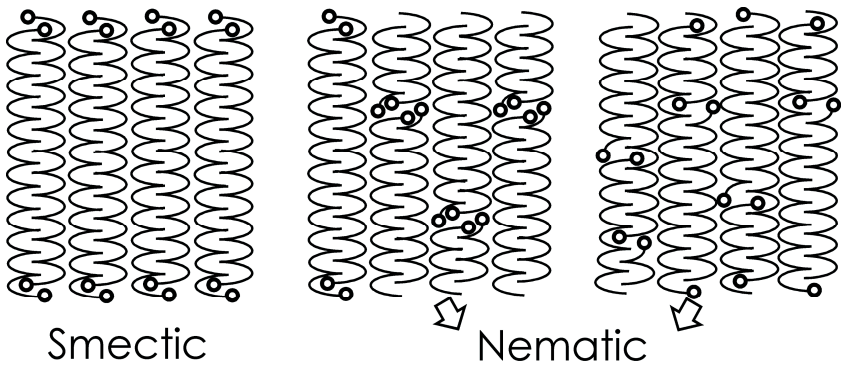

Figure 5 Schematic representation of the smectic and nematic models for short-chain monodisperse PEO.

A model with the exact formulation $LiPF_6 \cdot PEO_6$, containing 23 EO monomers (n=23) facilitates the study of the situation in which the end-groups are packed more tightly, and is more compatible with the size of the experimentally determined unit cell [25]. Also, to learn more about the structural conditions which relate to ion mobility, it was necessary to create a range of models to represent different structural situations one might reasonably expect to encounter in this type of system. In Paper **III**, five models were simulated: two *smectic* and three *nematic*; see models 1-5 in *Fig. 6*:

- *Smectic-A* (**1** in *Fig. 6*): the chain-ends are here all arranged in planes to form a common interface, with the Li-ions all 6-fold coordinated to ether oxygens within the same PEO double hemi-helix (three from each); see also the upper figures in *Fig. 6*.

- *Smectic-B* (**2** in *Fig. 6*): same as *smectic-A* except that Li-ions now bridge the interface and are coordinated to PEO chains on both sides

of the *smectic* plane. In this way, we introduce a disorder feature into the Li-ion coordination at the interface. Again, see the upper figures in *Fig. 6*.

- *Nematic-A* and *nematic-B* (**3** and **4** in *Fig. 6*): these models derive from their corresponding *smectic* counterparts through random displacement of neighbouring hemi-helical PEO pairs along the channel direction. These types of configuration were suggested by Bruce *et al.* to best represent the crystal structure for monodisperse systems [31].

- *Nematic-R* (**5** in *Fig. 6*): this is the most disordered of the models simulated, in which all chain-breaks occur randomly throughout the structure. This model corresponds to that proposed in [31] as the most rational structure for polydisperse systems.

Within this *smectic*/*nematic* classification of starting structures for n=23, we also distinguish two types of chain-end coordination around the Li-ions: *ideal* coordination, in which chain termination does not disrupt either of the polymer chains involved in the 6-fold coordination sphere of a Li-ion, and *broken* coordination, where this is not the case.

As shown in *Fig. 6, smectic-A*, and *nematic-A* involve *ideal* coordination, while *smectic-B* and *nematic-B* contain *broken* coordination. *Nematic-R* involves both types of coordination, but where the majority are broken. This issue of order/disorder in Li-ion coordination has largely been overlooked earlier because the crystalline oligoether-salt complexes studied have involved either very short monodisperse PEO oligomers [66-69], where the coordination in stoichiometric complexes is well defined, or much longer polydisperse chains, where the lower concentration of chain-ends renders them of minor significance. However, a study of single crystals of $PEO_3(M_w{\sim}500).LiCF_3SO_3$ has revealed a high selectivity to polymer chain-lengths on crystal formation [70].

Chain ordering is therefore analysed in terms of two distinct structural features: *(i)* ordering in neighbouring chain-ends; and ii) the coordination (*ideal* or *broken*) of Li-ions to the polymer chain.

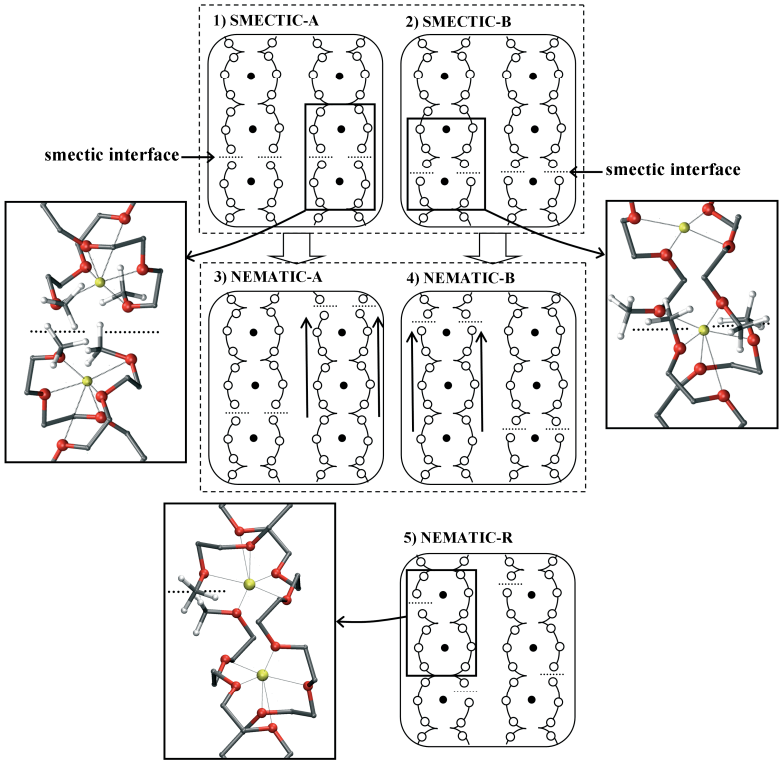

Figure 6 A schematic representation of the models simulated for $LiPF_6$•PEO_6; 1) smectic-A with the chain-breaks outside the 6-fold Li-O coordination sphere; 2) smectic-B with the chain-breaks perturbing the 6-fold Li-O coordination; 3) and 4) nematic-A and nematic-B, derived from the corresponding smectic models by shifting adjacent PEO channels along their axes (see arrows); 5) nematic-R has randomised chain-break locations. Typical snapshots of structural detail within chain-break regions are given at the top of the figure.

Non-equilibrium molecular dynamics

When an external perturbation like an electric field is imposed on the simulation box (as in Paper **IV**), the system response, in this case ion migration, can be investigated by MD. The major challenge in such a study is to choose an appropriate strength for the external electric field. As we see below, too high field strength can induce unwanted structural transformations, while the effect of too low a field strength remains unnoticed throughout the duration of the simulation. In Paper **IV**, a series of static electric fields (ranging from 3 to 6 × 10^6 V/m) were applied parallel to the hemi-helical axes of models *smectic-B, nematic-B* and *nematic-R*, and simulated for a further 300 ps.

The same range of fields was also applied in the *c*-direction parallel to the end-plane of the *smectic-B* system. Some tests were also made to apply the fields in the *b*-direction within the smectic plane; these gave qualitatively identical results. The *smectic-A* model was also simulated under the conditions shown in *Table 1* for the *smectic-B* system, to assess the effect of complete *vs.* broken coordination.

Ion transport

Rather than calculating ionic conductivity values from diffusion coefficients derived from mean-square displacements of different ion-types (an unreliable procedure in view of the poor statistics from short simulation times), comparative values are derived for the different systems by counting *ion-jumps* in the direction of the imposed field.

Ion conductivity (σ) in electric field E can be derived from the frequency of ion jumps (n) for the 1-D case using the expression:

$$\sigma = \frac{j}{E} = \frac{\Delta q}{\Delta t \cdot s \cdot E} = n \cdot \frac{r \cdot e}{a} \cdot \frac{1}{\Delta t \cdot b \cdot c \cdot \sin\beta \cdot E} \approx 5 \cdot 10^3 \, \frac{n}{E} \left[\frac{S}{cm} \right]$$

where we use the MD-box geometry (*a, b, c,* sinβ), the characteristic Li jump-length (r = 2Å) and $E = 10^8$ V/m (an estimate of the thermal excitation at the temperature of the simulation: 328K); the value of r corresponds to a Li-ion propagation distance of one O_{et} - O_{et} distance. This gives an estimated jump frequency (n) of 0.05 jumps/ns for an experimentally observed conductivity (σ) of 10^{-6} S.cm^{-1}. Under these circumstances, it is quite unrealistic to hope to quantify conductivity values on the basis of observed jump frequency, but rather to establish the most likely pathways for ion transport, as evidenced by observed ion migration modes under the electric field. However, local conductivity measurements in amorphous polymer electrolytes using microelectrodes suggest that conductivities along the most conducting pathways can be 10^3 times higher than the macroscopically measured average conductivity [71].

It was established from several test simulations that a very narrow window of electric field strength exists within which ion migration can be observed without structural instability. Ion conductivities have therefore been quantified for the different short-chain systems modelled at the electric field-strength threshold values where ion jumps clearly begin to occur. Additionally, an in-depth analysis of typical ion-jump events is carried out by looking at related local coordination situations and attempting to relate these to differences in the models.

Simulation of XRD profiles

An effective diffraction pattern was calculated by accumulating the scattering contributions from 500 MD-generated "snapshots" of the positions of all the atoms in the MD box. This is done using an adapted version of the DISCUS program [72]. No symmetry constraints are applied to the system during this calculation – the program treats the entire MD box as a primitive unit-cell. Only Bragg reflections are sampled; peak-widths are all constrained to 0.16^{o} (in 2Θ) to roughly match experimental values.

Results

As in our earlier study (Paper **III**), the general form of the "infinite-chain" structure is retained throughout the various simulations of the n=23 system, despite the high concentration of end-group "defects". Isotropic atomic displacement factors (ADF's) averaged over all 32 PEO chains in the MD-box have been extracted for the backbone ether-oxygen atoms along the chain (see *Fig. 7*). Higher displacements at the chain-ends are clearly reproduced, and are seen to agree quite well with the overall experimental value for salt-free PEO (*ca.* 0.11 $Å^2$).

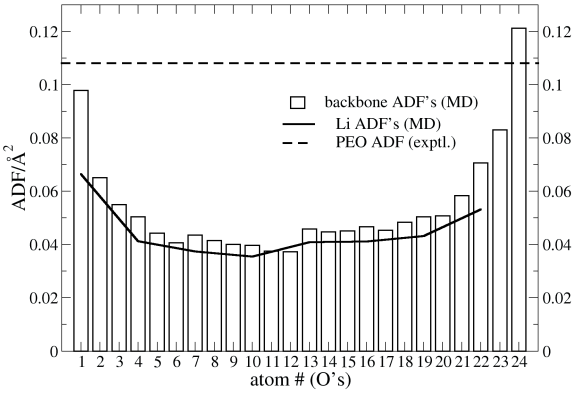

Figure 7 The atomic displacement factors (ADF's) for the backbone oxygens along the chain (n=23); the lines show our MD values for Li-ions and the experimental value for long-chain crystalline PEO.

Structural stability

Visual inspection of the sampled snapshots could readily confirm that all the simulated systems maintain the general characteristics of their start structures – with cylindrical double hemi-helical PEO channels still separating the Li-ions within the channels from the PF_6^- anions outside the channels.

In the n=23 systems, all structural disruption occurs only in the vicinity of the end-groups, and ion-pairing is noted only in systems involving broken Li-ion coordination in the defect regions. However, in the n=22 systems

(Paper **II**), distortions are significantly larger, and many more ion-pairs form in defect-free regions, with the PEO channels tilting as shown in *Fig 8*.

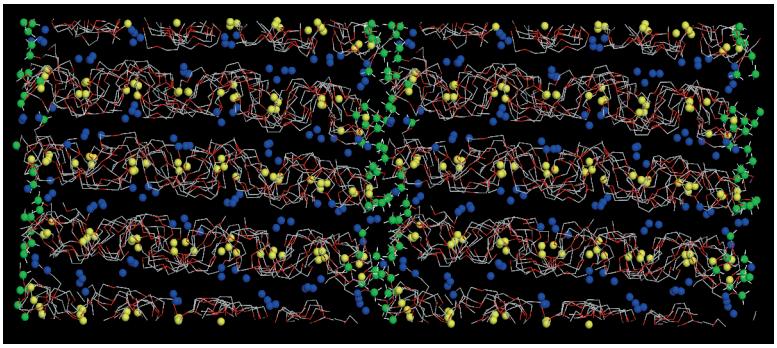

Figure 8 A snapshot of the MD-box at the end of the simulation (doubled in the a-direction) for the smectic model of $LiPF_6$·$PEO_{5.75}$ (M_w = 1015 for "PEO"); Li^+ are yellow, P are blue, CH_3-groups are green; H and F are omitted for clarity.

Another observation is that the shape and size of all MD boxes for n=23 are generally retained for all models, when their geometry is released on going from NVT to NσT ensemble simulation. All boxes tend to shift in the same general way: the *a*-axes (the polymer-chain direction) all expand (on average by 2.5%), while the *b*- and *c*-axes both contract by roughly the same amounts.

All types of double hemi-helices modelled undergo breakdown within the 300 ps simulation sampling time beyond the structural instability threshold value. This value was lowest for the n=22 systems. Among the systems with n=23, the *smectic-B* model is the most stable, while the *nematic-R* model is the least stable. Also, the crystalline structure is less stable when the electric field is applied in the direction of the PEO channel compared to perpendicular to the channel. Notably, no significant differences in stability could be detected between the doped and undoped systems. The breakdown process when the system becomes amorphous can be correlated to the extraction of Li-ions from inside the double hemi-helices. Since Li-ions can more easily leave the PEO channels near the chain-ends and methoxy end-groups tend to retain their coordination to the Li-ions, they are dragged away from their normal locations into the anion channel. Given the more uniform distribution of chain-ends in the *nematic-R* arrangement, chain breakdown is initiated simultaneously at a number of sites throughout the structure, thus explaining the lower stability of this system. Generally, when two adjacent Li-ions leave a channel, this region of the polymer loses it original conformation, and the individual chains straighten out and separate from one another; see the dashed region in *Fig. 9*. It was also pointed out earlier by Henderson *et al.* [68] that the cylindrical two-chain configuration is unlikely to be preserved if ether oxygen atoms do not coordinate Li-ions.

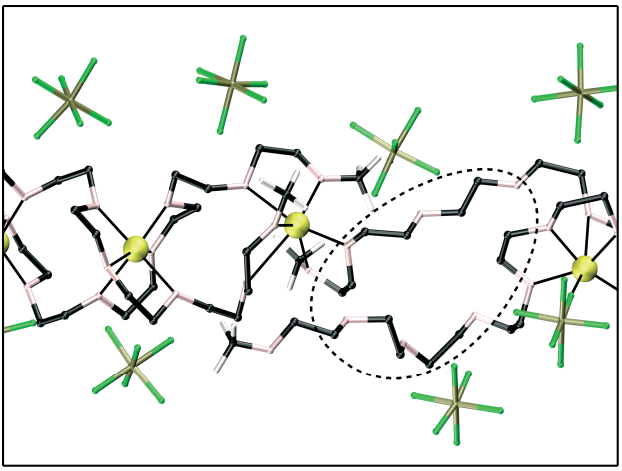

Figure 9 An example of the breakdown in continuity of the helical chain structure (the circled region) across a defect under the effect of an applied electric field.

Li-O coordination and ion-pairing

Chain-shortening as in the n=22 systems leads to a redistribution of Li-ion coordination compared to infinite systems: CN(Li-O) decreases to 5 while CN(Li-P) increases to 0.5, *i.e.,* 50% of the Li-ions form contact pairs with anions both in defect and defect-free regions.

More detailed analysis has been undertaken for the n=23 systems. The models involving ideal 6-fold Li-O coordination all maintain this coordination number throughout the simulations, even in defect regions (see *Fig. 10*; *smectic-A* and *nematic-A*), while CN(Li-O) is seen to vary from 4 to 7 in the remainder of the systems simulated. Such variations in broken-coordination situations occur mainly in defect regions involving 2-3 Li-ions.

The 7-fold Li-O coordination (the dashed line in *Fig. 11*) is unstable, with the 7th coordinating oxygen spending typically < 5 ps at a Li-O distance less than 3Å.

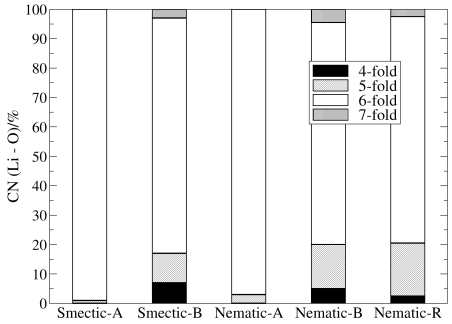

Figure 10 Distribution of Li coordination numbers CN(Li-O) for the five simulated $LiPF_6$·PEO_6 systems (see Fig. 6).

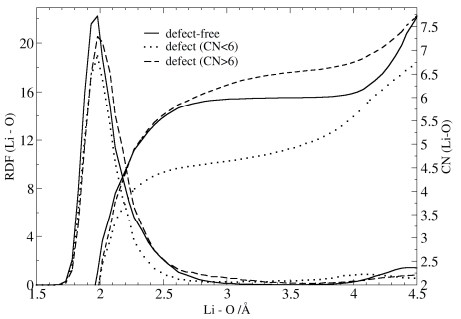

Figure 11 Li-O radial distribution functions RDF(Li-O) and coordination numbers CN(Li-O) for the nematic-B $LiPF_6$·PEO_6 model with defect-free and defect regions plotted separately.

A typical *smectic-B* broken-coordination situation is demonstrated in Fig. 12: in the left-hand channel, the Li-ion on the lower side of the defect region remains coordinated by one end-group oxygen belonging to the next polymer chain (**A**), whereas another oxygen has migrated to coordinate to the Li-ion on the upper side of the defect (**B**). In the right-hand channel, however, both chain-ends from the polymer channel at the upper end of the defect have left the coordination sphere of the Li-ion on the lower side of the defect, resulting in two uncoordinated methoxy-groups in the defect region (**C**). This deficit in coordinating oxygens around the Li-ion on the lower side of the gap causes the end-region of this channel to contract, allowing ion-pair formation (**D**). The persistence of the "Li-bridging" coordination (**A**) shown in Fig. 12 can have an important impact on the overall stability of the structure.

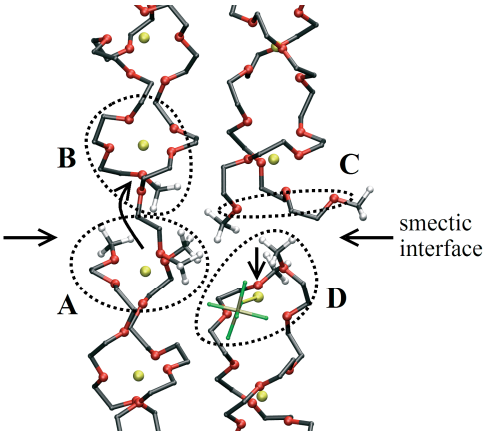

Figure 12 PEO-chain conformation rearrangements and corresponding Li coordination in the defect region of the smectic-B model of $LiPF_6$·PEO_6.

Ion-pairing thus occurs predominantly in coordination situations which involve exclusively Li-ions with low CN(Li-O); see *Fig. 12*. Through competition with the coordinating ether oxygens, Li-F coordination is always 1-fold, unless the Li-ion has migrated outside the PEO channel. Since defect regions contain uncoordinated methoxy groups (*Fig. 12* **C**), ion-pairs occasionally dissociate, thereby restoring the bridging configuration **A** shown in *Fig. 12*. These ion association-dissociation events occur on a nanosecond time-scale and correlate with changes in CN(Li-O); pair formation leads to a decrease in CN(Li-O) and *vice versa*.

The proportion of Li ions with 4-fold coordination decreases in the systems simulated in the order: *smectic-B* > *nematic-B* > *nematic-R*, which correlates well with the observed decrease in ion-pair concentration. The *nematic-R* system incorporates predominantly situations in which only one of the PEO hemi-helices in any Li-O coordination sphere is broken; as illustrated in *Fig. 6*. This reduces the possibilities for lower Li-O coordination, and thus leads to a higher incidence of 5-fold coordinated Li (*Fig. 10*). In the *nematic-R* system, almost 50% of the ion pairs form outside the defect region, which corresponds well with the more dispersed nature of the imposed isolated defect distribution.

Considering the specific role of terminal groups in promoting ion-pair formation, we see that the further the methyl-group pairs move away from their positions along the channel walls (*Fig. 13b*), the more they avoid one another and thereby provide more space for ion-pair formation. From Figs. *13a-c*, we see that the methyl end-group separation correlates well with the incidence of ion-pair formation.

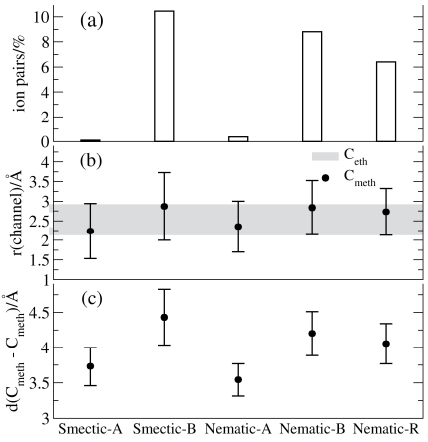

Figure 13 (a) Percentage of Li-ions participating in ion-pairing for the five simulated models for $LiPF_6{\cdot}PEO_6$, as described in Fig. 6; (b) chain-end methyl carbon (C_{meth}) displacements from the PEO channel axes compared to the displacements in defect-free PEO; and (c) corresponding C_{meth}-C_{meth} separations across the chain-break regions.

It is possible that comparative *vibrational spectroscopy* data for mono- and polydisperse systems could distinguish ion-pairing and Li-O coordination for the different models simulated. All broken Li-O coordination regions should involve a detectable number of ion-pairs. Several spectroscopic studies have already addressed structural issues regarding $LiPF_6{\cdot}PEO_6$ and its isostructural crystal forms [73-75]; there is some evidence to suggest "spectroscopically free" anions in these materials.

The channel structure

Let us first consider how the channel structures differ in the *smectic* and *nematic* models depending on the nature of the chain-break defect (A, B or R) (*Fig. 6*). The Li-Li distances are found to reflect well the different structural situations for the Li ions, especially in the chain-break regions. In the *smectic-A* and *nematic-A* systems, the average distance from a Li-ion in a defect region to its nearest Li neighbour is closely similar to that in a defect-free region (5.8 Å compared to 5.9 Å), while the Li-Li distance across the defect region is *ca.* 7.5 Å. This appears as an extra peak in the RDF(Li-Li) plot for the *nematic*-A case; *Fig. 14a*. This peak is also present for the *smectic-A* case (not shown). In this model, a slight lateral displacement was noted in successive PEO channels in adjacent blocks. Interestingly, these displacements were larger in the n = 22 PEO system.

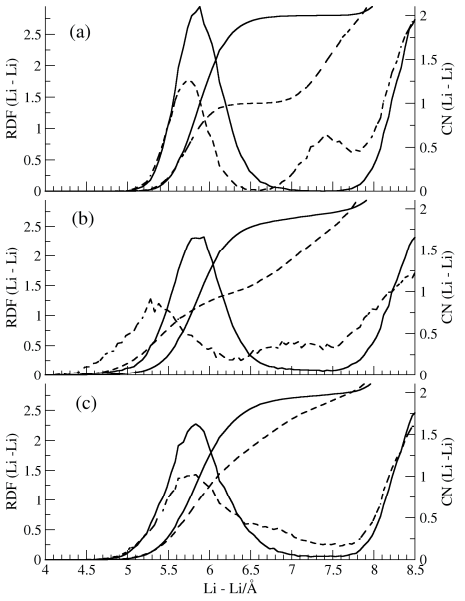

Figure 14 Li-Li radial distribution functions RDF(Li-Li) and coordination numbers CN(Li-Li) in defect-free and chain-defect regions for different conformations of $LiPF_6$·PEO_6: (a) nematic-A; (b) nematic-B, and (c) nematic-R.

Li-ions in channel-end defect regions for CN(Li-O) < 6 (*i.e.,* B-type systems) tend to move closer to the Li ions in the end-regions of successive PEO channels; with Li-Li distances *ca.* 5.2 Å compared to 5.9 Å in defect-free regions (*Fig. 14b*). The Li-Li distances *across* the defect region vary over a broad range (6-8 Å) compared to this distance in A-type systems (*Fig. 14*), with the shorter *ca.* 6 Å Li-Li distance corresponding to the "chain-bridging" configuration shown in *Fig. 12*. This type of local structural arrangement provides regular continuity in the Li-ion sequence across a channel break, and could therefore facilitate the experimentally observed enhanced Li-ion transport [30]. On the basis of such structural considerations, the B-type defect would therefore seem the more reasonable.

Chain defects in the *nematic-R* model situation rarely involve both hemihelices around a given Li-ion. This appears to cause Li-Li distances in these defect regions to vary less than in the *smectic-B* and *nematic-B* models; typically 2 Å *vs.* 3Å. This is also evident from RDF(Li-Li) plots (*Figs. 14a-c*).

In *A-type* models involving 6-fold coordinated Li ions, the methyl-groups also remain somewhat closer to the PEO channel axis compared to the B- and R-type situations (*Fig. 13b*). The shorter distance of methoxy- compared to ethoxy-carbons from the central channel-axis indicates that the Li ions in the defect regions are tightly bound to the surrounding polymers, and may well be immobilised by high activation-energy barriers to Li transport. Interestingly, even if the Li-Li distances across the gap in the *A-type*

models (as discussed above) are larger than in *B-type* systems, the distance between the methyl-groups across the defect are consistently shorter (*Fig. 13c*). This is because *ca.* 50% of the methoxy-groups in *B-type* systems are not coordinated to Li ions and are therefore free to migrate away from their normal positions near the PEO channel walls into the space outside the channels (see *Fig. 12*).

The smectic surface

One of the prime goals of this study has been to endeavour to set up what could best be described as a smectic interface model. This has been done by creating an MD box in which registry has been established between an array of parallel monodisperse short-chain (n=23) PEO double hemi-helices, thereby creating an extended plane of methyl chain-ends at either end of "nano-crystalline blocks". The periodic symmetry relating the blocks generates the required smectic interface; see *Fig. 15*.

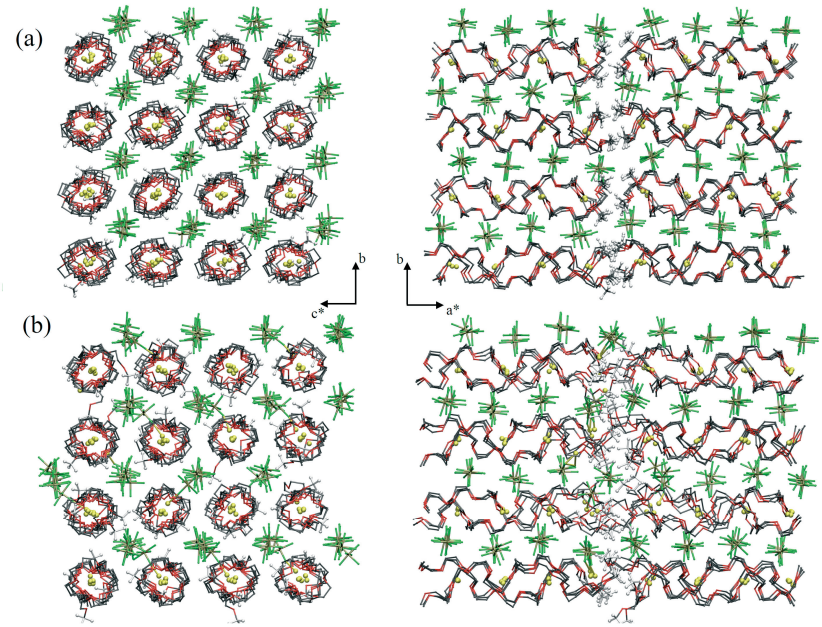

Figure 15 MD snapshots for (a) smectic-A and (b) smectic-B models of short-chain $LiPF_6$·PEO_6.

As described earlier, two types of smectic model (*A* and *B*) are studied, differing only in the position of the chain-breaks with respect to the Li-ions. The behaviour of the two models is found to be quite different: in the *smectic-B* model (*Fig. 15b*), the PEO-tunnels link together *via* "bridging" methoxy groups, and the defect region involves disordered Li-ions, which could

favour ion transport. In contrast, the *smectic-A* system (*Fig. 15a*) exhibits neither bridging groups nor disordered Li-ions. Furthermore, the double hemi-helical PEO channels in the *smectic-A* system show small (~ 0.5 Å) lateral displacements which slightly perturb the translational symmetry of the crystallite; see *Fig. 15*.

Simulated XRD profiles

The calculated XRD profiles are shown in *Fig. 16*. These can be compared with the experimental XRD profile (*Fig. 16*, bottom) [76]. In this context, however, it is most important that we first consider the basis for the appearance of particularly the experimental profile. Since experimental XRD intensities (to a good approximation) only contain information regarding translational features in the unit-cell structure, these will therefore not contain any direct information relating to surface or chain-end features present in the material. Two interesting possibilities thus arise:

- The experimental XRD data will lack information on such "defect regions" lying at the surfaces of the effective diffracting mosaic blocks in the real material, and refinement of the data will therefore only reflect the structure of the defect-free regions inside these blocks. This is the situation for a *smectic* arrangement; or
- When the "defect regions" are more or less randomly distributed throughout the real structure (as is the case for the various *nematic* models simulated), the XRD data will actually contain partial information on these defects, and refinement of the resulting XRD data will include an "averaged-in" weighted component of the defect regions superposed on the defect-free structure. In other words, the resulting refined model will fit less well to the data – but will, in this case, include the averaged-in effect of the defect distribution.

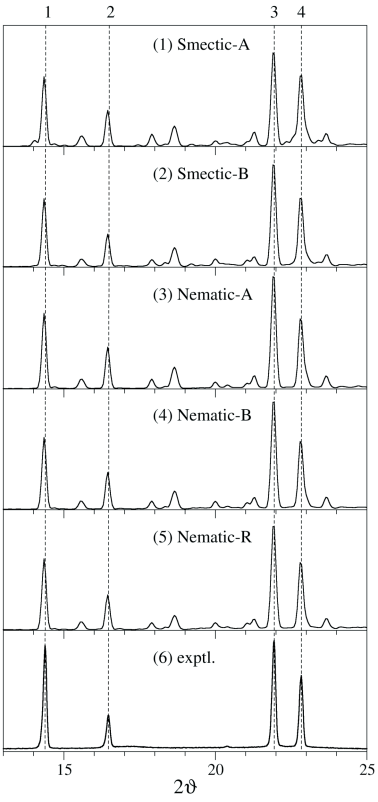

Figure 16 Calculated XRD "powder" profiles for the five MD models for $LiPF_6{\cdot}PEO_6$, as summarised in Fig. 6, with cell parameters constrained to values determined from the experimental XRD profile in the bottom figure.

We are left therefore with the paradoxical situation that a better fit to experimental data could imply a *smectic* situation but would actually tell us little about the end-chain defects in the system, whereas a poorer fit could imply a *nematic*-type structure, since the effect of defects is now present in the experimental data but not in the refined model.

In practise, we see no significant differences in agreement with experiment for the *smectic* and *nematic* models. There are, however, added complications, *e.g.,* there is no direct correspondence between MD-box dimensions and the size of the scattering "mosaic blocks"; nor have we considered the coherence length of the diffraction process in relation to the size of the MD-box or the "mosaic blocks". In short, XRD is an inappropriately crude and uncertain technique for distinguishing between possible short-chain ordering models.

Effect of ordering on ion transport in PEO channels

A detailed analysis of ion migration events has been undertaken for the n=23 systems *smectic-B*, *nematic-B* and *nematic-R*, containing mobile and "bridging" methoxy groups in the defect regions. Two types of ion-jump can be distinguished in the direction of the PEO channels: longer jumps corresponding to typical Li-Li distances in the material (~6 Å), and shorter jumps of around 2-3 Å (see *Fig. 17*). These short jumps correspond to Li migration within the PEO channel involving only a few (up to 4) ether oxygen atoms. From *Table 1*, it is clear that shorter jumps are more common for Li-ions, whereas anions tend to undergo longer jumps (also ~6 Å). These occur cooperatively, involving the chain-sequence of neighbouring anions.

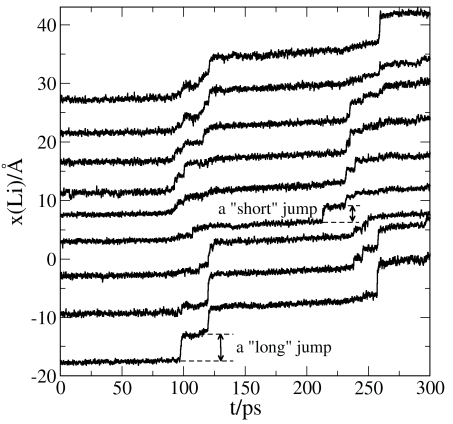

Figure 17 The x-coordinates (along the polymer-chain direction) for the Li-ions along a PEO channel plotted over 300 ps for the short-chain $LiPF_6$·PEO_6 (n=23) system at $E=4.5 \times 10^6$ V/m.

The differences compared to the *infinite* systems are: 1) the increase in the number of Li-ion jumps with respect to number of anion jumps, and 2) the large variations in anion jump-rates from system to system. In most of the models simulated here, Li-ions undergo fewer longer jumps than the PF_6^- ions, since longer jumps require a collective sequence of participating sites, which is inhibited by the strong local Li-O_{et} interactions. Predominantly short Li-ion jumps were also seen in the infinite-chain system [77], but in the short-chain situations simulated here, they clearly dominate, even over short anion jumps. This raises the question as to whether it would be possible to observe only short jumps at lower electric fields if longer simulation times were feasible. Indeed, only short jumps occurred in the undoped *nematic-R* simulation (*Table 1*), which would appear to support the notion of the dominance of Li-ion transport, as suggested by Bruce *et al.* on the basis of NMR measurements [26]. It is certainly clear that the transport number for Li-ions

is here considerably higher than in the infinite-chain systems, where it was only 0-0.1 [77], but where poor statistics disallowed any attempt at further quantification.

Table 1 Number of ion-jumps/300 ps for the various systems simulated.

System		Field/ 10^6 V/m		Li^+ jumps < 4.5 Å	Li^+ jumps > 4.5 Å	PF6- jumps < 4.5 Å	PF6- jumps > 4.5 Å
Smectic-B	Undoped	∥	4.75	13	2	9	33
		⊥	6	12	0	8	4
	SiF_6^{2-} -doped	∥	4.75	18	1	16	15
		⊥	6	11	3	11	6
Nematic-B	Undoped	4.5		18	3	6	48
	SiF_6^{2-} -doped	4.5		18	7	0	4
Nematic-R	Undoped	4.0		7	0	2	0
	SiF_6^{2-} -doped	4.0		12	1	1	9

Li-ion conduction mechanisms

A basic requirement for Li-ion migration inside the PEO channels seems to be the availability of a low-CN to ether oxygen atoms. In Paper **III**, we found generally that more ion-pairs and uncoordinated ether oxygens are found near the chain-ends. In the *smectic-B* system, these ether oxygens are therefore confined to the smectic interface, separated by highly ordered regions; while they are more uniformally distributed throughout the nematic systems. The concentration of 5-fold coordinated Li-ions (Fig. 10) is found to be highest in the *nematic-R* (18%) and lowest in the *smectic-B* case (10%). Unlike in the *smectic-B* case, however, a substantial number of Li-ions with CN(Li-O)<6 are found in defect-free regions of the nematic systems. Li-ion coordination would appear to be more stable in the ordered regions of the *smectic-B* system. This would all suggested that Li-ion conductivity within the PEO channels is lower in the *smectic-B* than in the *nematic-B* and *nematic-R* systems, which is consistent with the higher electric field needed to trigger Li-ion migration in the *smectic-B* system.

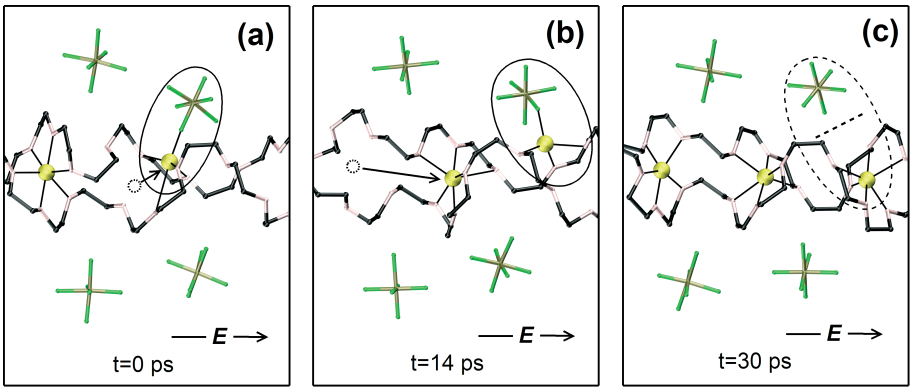

Figure 18 An anion-mediated Li-ion conduction mechanism inside a PEO channel: (a) ion-pair formation followed by (b) ion-pair migration and simultaneous Li-occupation of the vacancy site left as a result of the pair formation; and finally (c) ion-pair breaking and Li-occupation of an available vacancy site.

A new, anion-mediated Li-ion transport mode appears in the short-chain systems which was not seen in the earlier infinite-chain model simulations. Li-ions move along the PEO channel in the steps illustrated in *Fig. 18* for the *nematic-B* model. Li-ion displacement to create an ion-pair leaves behind it a vacancy and an uncoordinated O_{et} atom (*Fig. 18a*). This vacancy is subsequently occupied by a Li-ion (*Fig. 18b*), and the ion-pair finally breaks (*Fig. 18c*). In this way, a sequence of Li-ions has moved along the channel. The important difference compared to the Li-ion conduction mechanism described for the *infinite* system is that longer jumps occur here, as seen in *Table 1*.

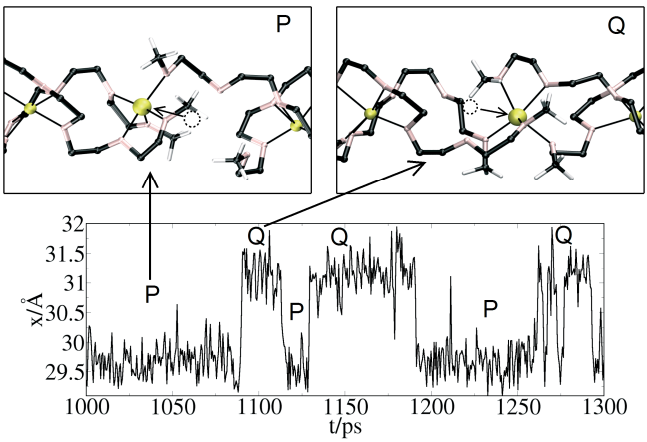

Figure 19 Li-ion dynamics (without external electric field) in the defect region; P and Q are snapshots of two Li positions before (P) and after (Q) jumps across the defect gap. The lower figure exemplifies the times spent in these two types of site.

Poor statistics in the Li-ion jump-count makes it difficult to compare the barriers for Li-ion migration across the two types of defect gap *(Fig. 6*; *nematic-B* and *nematic-R*). This barrier can be low in *nematic-B* systems, where local hopping (*Fig. 19*; P⇔Q) occurs across the gap during 300ps under zero applied external field. Generally, Li-ion migration is observed for 3-6 available (uncoordinated) ether oxygens in the jump-target region (*Fig. 20b*). With less available ether oxygens, ion-pair formation is more likely (see *Fig. 20a*). When a vacancy extends over more than one Li site, *i.e.,* when we have > 6 uncoordinated ether oxygen atoms, Li-ion migration is suppressed, since the PEO double hemi-helical channels break down; as shown in *Fig. 9*.

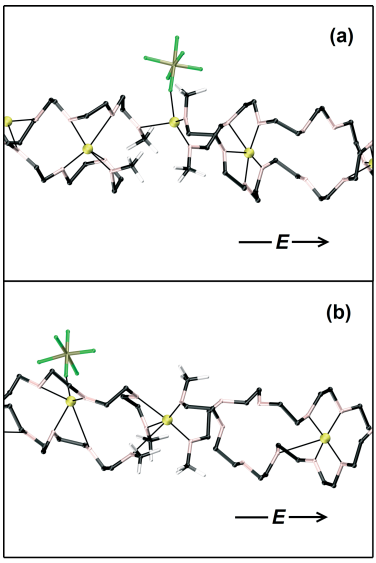

Figure 20 Li-ion migration mechanisms across the defect gap under an imposed electric field along the chains: (a) when mediated by ion-pair formation, and (b) direct migration into an available vacancy site.

Anion conduction mechanisms

In the *infinite* system, the longer anion jumps always occurred sequentially for a row of PF_6^- ions along the inter-helical channels. This mechanism was shown to be related to ion displacements perpendicular to the polymer chains (the *yz*-direction), whereby one anion is paired with a Li-ion still within the double hemi-helix. Such *yz*-displacements of the anions are often precursors to motion in the channel-direction, thereby creating a vacancy into which a neighbouring anion can move.

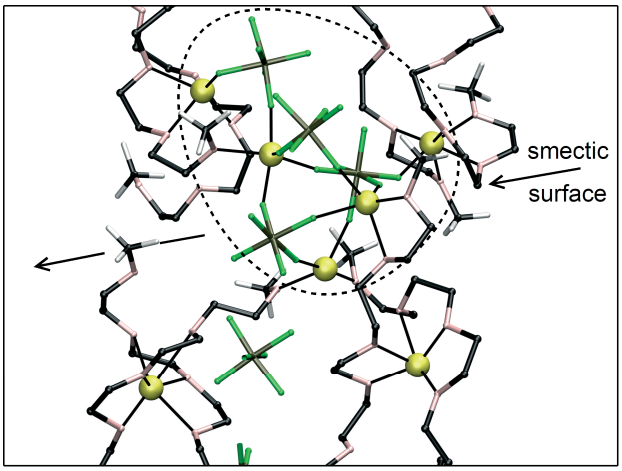

Figure 21 Ion-clustering in the smectic interface, which suppresses anion migration along the channel. The dashed region marks the boundary of a +1-charged ion-cluster region involving 5 Li-ions and 4 anions.

Long PF_6^- jumps still occur predominately between different anion sites, but the sequential movement is always interrupted somewhere along the anion column. In the *smectic-B* case, this often occurs at the interface region in conjunction with ion-pair formation. As shown earlier (*Fig. 20a*), an ion-pair formed at the interface can dissociate and reopen the channel for subsequent ion motion, but high carrier concentration at the smectic interface promotes aggregation of ionic species, and ion-clusters so formed block migration in the corresponding anion channel (*Fig. 21*). This explains the large difference in the number of long anion jumps between undoped (48 jumps) and SiF_6^{2-}-doped (4 jumps) *nematic-B* and *smectic-B* systems (see *Table 1*) for the same field strength.

In the *short-chain* systems, in addition to long correlated anion jumps, shorter uncorrelated jumps occur in isolation or sequentially in pairs. This process has two origins: *(i)* the more mobile methoxy groups create space near the chain defects for anions close to the PEO channel; and *(ii)* ion-pairs are formed near the chain defects with longer lifetimes than in the *infinite* system; these influence the available positions for the neighbouring anions. A typical anion transport sequence is shown in *Fig. 22*, as taken from the *nematic-B* simulation; non-coordinating methoxy groups move deep into the anion channel, but do not block it. Instead, space is provided into which anions can migrate, leaving behind vacancy.

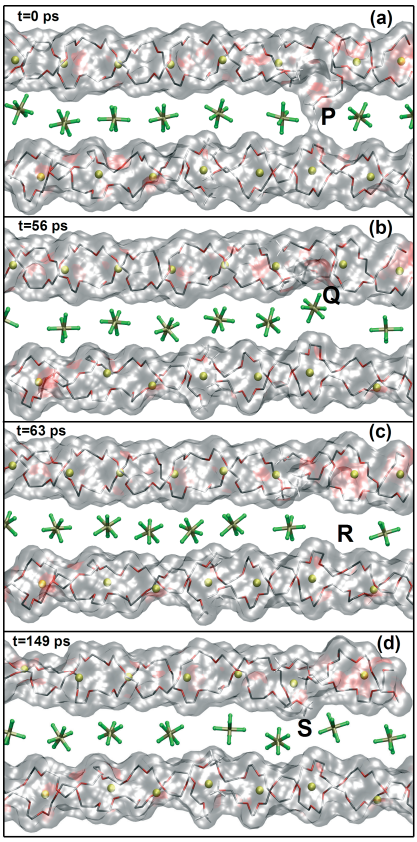

Figure 22 Typical events in the anion and Li/PEO channels (shown as excluded volumes) in the nematic-B model: (a) an uncoordinated methoxy group (P) moves into the anion channel; (b) a mobile chain-end provides space which becomes occupied by an anion (Q) and leaves behind a vacancy; (c) this vacancy-site (R) is not occupied immediately if there is structural blockage; (d) the vacancy-site is then occupied by an anion, but the anion channel is blocked as a result of structural chain rearrangement.

Ion transport within the smectic interface

Two types of jump occur within the smectic plane: shorter jumps of up to 4.5 Å, and long jumps of ~8 Å (*Table 1*). These distances correspond to the half and full distance between neighbouring channels (anion or cation), with longer jumps occurring considerably more infrequently. Longer anion jumps are also correlated, but the higher degree of disorder in the smectic plane means that this correlation and also the types of site occupied are less well defined than within the more ordered channels. Clearly, ion conduction is less in the smectic plane than along the PEO channels, as indicated by the

higher electric field needed to induce it (see *Table 1*). This is not unexpected, since there is no structural continuity (typically in the form of ion channels) perpendicular to the PEO channel direction, especially for Li ions which have to cross the gap between two approximately aligned PEO channels. The limiting factor for this to occur is ion-pairing in the interchannel space.

Li-ion conduction mechanism

The migration of Li-ions within the smectic plane is governed by two mechanisms: *(i)* direct migration, where PEO chain-ends move far enough into the anion channel to come into contact with one another - allowing Li-ions to use this as a bridge (see *Fig. 15b*); and *(ii)* indirect migration involving ion-pair formation as an intermediate step. Direct Li-ion migration is a fast process, while Li-ions are immobilised in the anion channel for the full duration of the simulation in the course of indirect migration. The first process is much less frequent, from which we can conclude that Li-ion conduction is very low. The reason for this is that the mobile methoxy groups within the smectic plane, which assist Li-ion transfer by coordinating it to both sides of the gap, provide only 2-3 fold Li-O coordination. Such an interaction is too weak to compete with ion-pairing.

Anion conduction mechanism

Anions appear to migrate more easily within the smectic interface than Li-ions (*Table 1*). The process involves two steps: migration into the gap between the two PEO chain-ends and transient pairing with Li-ions, followed by breaking the ion-pair and migrating into the neighbouring anion channel (see also *Fig. 23*). This process appears to involve local correlation – a vacant site is needed nearby to which the anion can migrate.

We can note a clear difference in ordering within the smectic interface: the coordination of Li-ions in the interface region is broken in the *smectic-B* system studied in Paper **III**. This leads to ion-clustering, which involves typically three or more anions and cations (see *Fig. 21*), since the electric field forces them more easily out of their normal positions. The ion-exchange rate between these clusters and the solvating polymer appears to be a limiting factor for ion transport. This behaviour can be compared with that in the more ordered smectic interface of the *smectic-A* model (*Fig. 6*) under the same in-plane electric field; much longer anion jumps were observed and no ion-clustering, since the Li-ions could not leave their sites (*Fig. 23*).

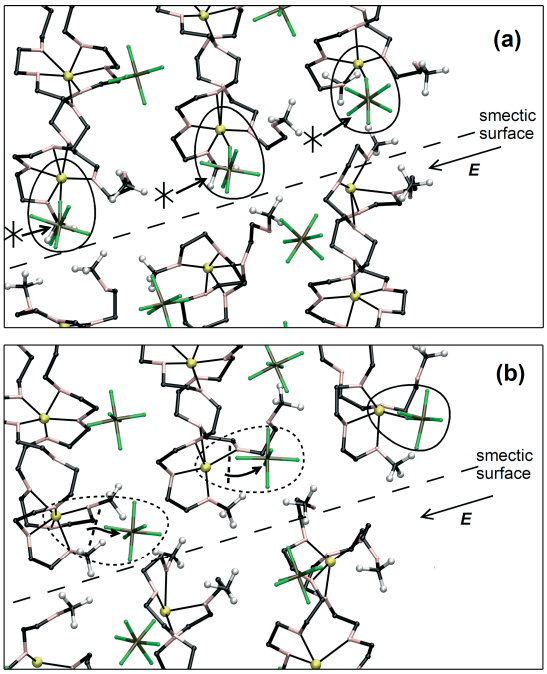

Figure 23 The two significant steps in the anion migration mechanism within the smectic plane: (a) anions move into the gap between the chain-ends to form ion-pairs (this can be accompanied by a change in CN(Li-O) and chain-end movement into the space of the anion channel); (b) these ion-pairs break and the anions move into the next anion channel.

Doping effects

Doping $LiPF_6{\cdot}PEO_6$ with ~1% SiF_6^{2-} ions has been shown experimentally to enhance its ionic conductivity [30,78]. This is seen in MD simulations of the *infinite* system as a lowering of the threshold field needed for ion motion [77]. The effect is less clear for the short-chain case (*Table 1*), with all systems exhibiting ion mobility irrespective of doping. The only significantly higher conductivity is seen for the *nematic-B* model, where a sequence of Li-ion jumps occurs in the channel containing the compensating Li-ion (see *Fig. 11* in Paper **IV**). The mechanism is of the "anion-mediated" type discussed earlier. The SiF_6^{2-} dopant ion itself does not actively participate in the conduction process, but remains immobile or diffuses to defect regions throughout the simulations. It remains uncoordinated if is far away from a structural defect, *i.e.,* away from chain-ends. However, Li-ions which have migrated to a metastable site in the PEO channel form ion-pairs in defect-free regions. Otherwise, SiF_6^{2-} ions either forms ion-pairs with one Li-ion in

an energetically favourable C_{3v} conformation ([79]) or clusters (involving two Li^+ ions, one in C_{3v}, another in C_{2v} conformation; see *Fig. 24*). Li ions are pulled out from the channel when CN(Li-O)<6, but continue to coordinate to ether oxygens, which distort to point outward from the channel. This configuration appears to suppress nearest-neighbour Li-ion migration, since there are no ether oxygens available for coordination.

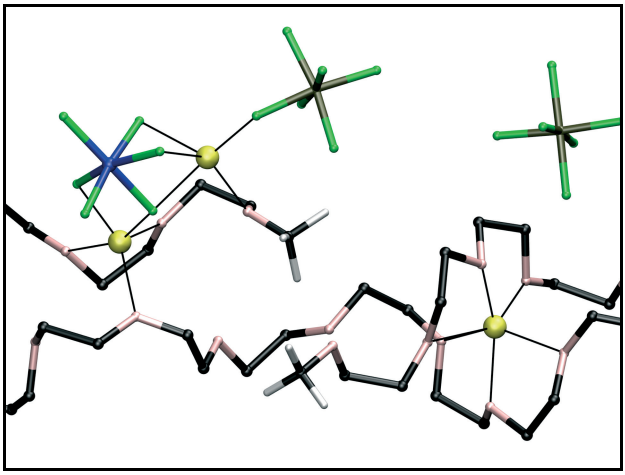

Figure 24 A typical ion-pairing situation for the SiF_6^{2-} dopant near the defect region, shown for the nematic-R system.

Conclusions and future work

Liquid crystal type ordering of short PEO chains (M_W~1000) in *smectic* (chain-ends confined to a two-dimensional plane) and *nematic* arrangements have been studied using Molecular Dynamics (MD) simulation. Highly ordered crystalline $LiPF_6{\cdot}PEO_6$ systems have provided an ideal model structure to probe such features, where the chains represent an immediate situation between high-M_W PEO complexes with negligible effect of chain-ends and the complexes involving short PEO ("glyme") molecules. While these molecules can readily find their most efficient packing, this is more complicated for longer oligomers, due to both slower kinetics and polydispersity. On this intermediate scale, the nature of chain-ordering defects plays a crucial rôle in determining its macroscopic behaviour - including ion conductivity.

XRD and MD simulation analyses both constrain the true structure into models: a crystallographic unit-cell and a quasi-periodic MD box, respectively. While MD simulation can provide unique information about local defects, it is still inadequate in describing long-range order; the opposite is true of the diffraction experiment. It is therefore challenging to find a common meeting ground for the two approaches where we can endeavour to construct a clearer picture of reality.

The poor statistics obtained for Li-ion mobility in the simulations means that, rather than attempting here to identify the "correct" local structure, it is more realistic to draw upon the somewhat fragmentary evidence available from the simulation of the multiple models investigated, and try to piece together some picture of the nature of the disorder in the material. Indeed, it is most unlikely that any genuinely "correct" structure actually exists, but rather a superposition of many metastable local structures. Nevertheless, some important findings can be highlighted:

- Slight non-stoichiometry (imposed by the removal of EO-groups from chain-defect regions in $LiPF_6{\cdot}PEO_{5.75}$) leads to a significant disruption of crystallinity.
- Three models (*nematic-R*, *nematic-B* and *smectic-B*), containing chain-breaks in the Li-ion coordination sphere ("bridging" arrangement), all provide a structural basis for the continuous transport of Li-ions along discontinuous short-chain PEO molecules.

- The transfer of Li-ions compared to anions is significantly increased in the short-chain systems compared to the long PEO-chain systems studied earlier. This can be explained by the increase in the proportion of Li-ions with lower coordination numbers (CN(Li-O)<6) and by the effect of the temporary formation of ion-pairs.
- The more disordered *nematic* phases require a lower threshold field to promote ion conduction than the *smectic* phases. This can be related to the spatially more uniform distribution of chain-end defects in the *nematic* systems.
- Likewise, the field threshold for ion conduction within the *smectic* interface is higher than that along the PEO channels.
- The interstitial Li-ions in the PEO channel, introduced through doping with Li_2SiF_6, enhance Li-ion conduction.
- Simulated XRD peak intensities for models with "bridging" arrangements (*nematic-R, nematic-B* and *smectic-B*) agree reasonably well with experimental data. However, it is difficult to assess the stability of these "bridging" arrangements on a macroscopic scale using MD techniques.

In a broader sense, however, it must be admitted that this work has hardly brought us much closer to making any significant breakthroughs in polymer electrolyte design; the critical structural factors which will make this possible remain as yet undiscovered.

In future work, it would be interesting to look into the possibility of growing such nano-crystalline structures on nano-architectured electrode materials [80,81], with potential applications in 3D micro- and nano-batteries, *e.g.,* [82], where the one-dimensional character of the ion conduction can be a great asset. Simulation could then also help improve our understanding of local structure and dynamics at such interfaces. Modelling of this kind of interface requires much larger systems than studied in this thesis, but numerous simulation studies of interfaces between amorphous polymers and inorganic nanoparticles have demonstrated the feasibility of such studies (see, for example [83, 84]).

Ion transport in low-dimensional channels is also highly relevant to biosystems, since this is a vital function of living-cell membranes. It would also be tempting to speculate on the possibility of designing a highly ordered polymer structures to support higher temperature anhydrous proton transport, without the need for a mediator molecule, *e.g.,* the rôle of water in the Nafion® fuel-cell membrane. To my knowledge, only amorphous systems have shown usable proton conductivity in anhydrous polymer materials (see [85]).

Populärvetenskaplig sammanfattning

Betydelsen av ordning i polymerelektrolyter

Ett envist problem

Elektrisk energi är en högst användbar form av energi, då den lätt kan konverteras till andra energiformer. Idag representerar elektrisk energi ca 6% av världens totala energikonsumtion, och distribueras främst genom globala och lokala elnät. Men elektriciteten kan också komma från andra små elektrokemiska enheter, som batterier och bränsleceller.

Alessandro Volta var först med att i modern tid konstruera ett fungerande batteri. Detta skedde år 1799. Som alla batterier bestod detta av två elektriska poler – en anod och en katod – med ett mellanliggande skikt som kallas elektrolyt. När de negativa elektronerna vandrar genom en ledning från anoden till katoden (och därmed kan driva t ex en lampa eller en mobiltelefon; se figur nedan), så kompenseras detta elektriskt med att positivt laddade atomer, så kallade joner, samtidigt vandrar genom elektrolyten från anoden till katoden.

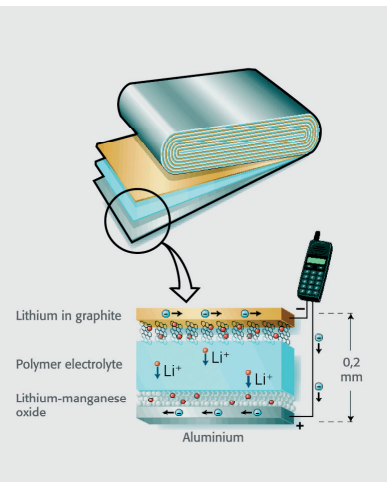

Fyrtio år senare, 1839, togs ytterligare ett avgörande steg i batteriutvecklingen när Michael Faraday upptäckte elektrolyter i fast fas, istället för de tidigare flytande. Detta har varit av stor betydelse under senare år, då säker-

hetskraven på moderna batterier gjort fasta elektrolyter efterfrågade. Dessa batterier används i stor utsträckning till den bärbara elektronik som så tydligt formar vår tidsålder. Ett envist problem med dessa fasta elektrolyter är dock att jonerna vandrar för dåligt genom dem när batteriet laddas ur – man säger att jonkonduktiviteten är för låg, och man forskar intensivt för att höja den.

Polymerelektrolyter

Polymerer är långa kedjeliknande molekyler, och har en rad olika användningsområden och finns flitigt förekommande i naturen. Plaster är typiska exempel på polymerer. Polymerer är ofta billiga och mekaniskt flexibla, och vissa polymerer – som polyetylenoxid, PEO – leder också joner bra, vilket Peter Wright upptäckte 1973. Därför kan de användas i batterier, vilket Michel Armand insåg 1979.

Efter Armands upptäckt tog forskningen om polymerelektrolyter fart på allvar. Snart kom man till slutsatsen att polymerernas rörelse var av stor betydelse för jontransporten genom dem, och därmed att jonledningen ägde rum i polymerens amorfa, oordnade fas, och inte i dess kristallina, ordnade fas. Forskningen därefter syftade därför mycket till att försöka öka de amorfa delarna på de kristallina delarnas bekostnad. På det sättet lyckades man höja jonkonduktiviteten, men fortfarande inte tillräckligt för de flesta batterier.

Ordning

Med denna kunskap om polymerelektrolyter kan det tyckas paradoxalt att de högsta jonkonduktiviteterna för fasta elektrolyter har upptäckts för kristallina material. Perovskiten $Li_{0.34}La_{0.51}TiO_{2.94}$, eller Li-β-alumina, är ett exempel på en sådan kristallin jonledare. Att dessa uppvisar hög jonkonduktivitet anses bero på att det finns gott om lämpliga plaster för jonerna att hoppa till när de vandrar genom materialet, och att det inte krävs så mycket energi för att hoppa mellan dessa platser. I andra kristallina material har man upptäckt hur vissa delar utgör små molekylära ”vattenhjul” som effektivt slussar jonerna genom materialet.

Dessa ordnade, kristallina fasta elektrolyter har varit en inspirationskälla när forskarna försökt förbättra sina polymerelektrolyter, och skapa motsvarande transportvägar i polymerer. Ett sådant exempel är den grupp polymerer som kartlades av Peter Bruce och hans medarbetare åren kring millennieskiftet: $LiXF_6 \cdot PEO_6$ (där X = P, As eller Sb). I dessa material så bildar polymeren (PEO) långa tunnlar för de positivt laddade Li-jonerna (Li^+), samtidigt som de negativt laddade hexafluoridjonerna (XF_6^-) ligger för sig själva utanför tunnlarna. Det visade sig att denna kristallina elektrolyt förvisso inte hade anmärkningsvärt hög jonkonduktivitet, men väl högre än den amorfa formen av samma material. Vissa forskare menar därför att förståelsen av detta system kan erbjuda en nyckel till hur man upptäcker polymerelektrolyter med högre jonkonduktivitet. Det är därför den här avhandlingen fokuserar på detta material.

Korta kedjor

Polymerer är som sagt långa molekylkedjor, men de kedjor som använts i fallet med $LiXF_6.PEO_6$ kan sägas vara anmärkningsvärt korta i flera fall då materialet studerats. Att de är korta har gjort att materialen är fulla med brott på polymerkedjan, och där brotten finns så sitter det också en speciell slutgrupp på polymeren. Dessa brott och slutgrupper kan i sin tur också vara ordnade enligt olika mönster i materialet. Emellertid är detta något som det inte tagits någon större hänsyn till hittills i forskningen, och det är dessa effekter som står i centrum i den här avhandlingen.

Molekyldynamikstudier

Den fantastiska förbättringen av datorer och datorprogram har gjort det möjligt att modellera hur material ser ut och beter sig på den atomära nivån. Inte minst har Molekyldynamik (MD) varit ett hjälpmedel för att studera hur joner rör sig i olika material. Molekyldynamik använder klassisk mekanik för att teckna en kort ”film” av ett material bestående av några tusentals atomer; man simulerar alltså materialet dynamiskt. Det är den metodik som använts i det här arbetet, vilket består av följande fyra vetenskapliga artiklar:

Artikel **I**: Här har kvantmekaniska studier gjorts för att kartlägga interaktionerna mellan partiklarna i materialet Li_2SiF_6. En god beskrivning av dessa interaktioner behövs nämligen för att kunna möjliggöra en senare MD-simulering, och interatomära interaktionerna mellan jonerna Li^+ och SiF_6^{2-} behövdes för vår studie av $LiXF_6{\cdot}PEO_6$ med små mängder SiF_6^{2-} (så kallad dopning) skulle studeras.

Artikel **II**: Den här artikeln behandlar en jämförelse mellan de situationer som uppstår när polymerernas brott och slutgrupper samlas i ett vidsträckt plan (denna struktur kallas smectic) eller när de är slumpvis utspridda (denna kallas nematic).

Artikel **III**: Denna studie går in i djupare detalj på hur de olika brottsituationerna ser ut – i vissa ligger en litiumjon mitt i själva brotten, i andra inte.

Artikel **IV**: Denna artikel beskriver hur jonkonduktiviteten i de ovan beskrivna systemen har studerats. En avgörande slutsats är att jonkonduktiviteten är som högst, där ordningen mellan slutgrupperna är som minst. En annan är att konduktiviteten blir mindre i det plan som bildas i smectic struktur beroende på att positiva och negativa joner möts där och fastnar i varandra – så kallade jonpar bildas.

Acknowledgements

First of all, I would like to thank my supervisor Professor Josh Thomas. You have always found time for me, encouraged me and helped to move in the right direction when I was hesitant. It is impossible to overestimate your efforts in getting my thoughts and ideas written down in plain English. Thank you for constant reminding that it is not computers and algorithms which matter but rather the solving of scientific problems!

I am also very thankful to my other supervisor Dr Daniel Brandell for being very patient and pragmatic in all our scientific discussions. And Daniel, what great discussions we have had on Politics and History!

Professor Alvo Aabloo - my advisor in Tartu University - thank you for introducing me to MD and for help in getting me started.

I am grateful to all the people at the Department of Materials Chemistry for creating such a pleasant research and social environment. ("No one mentioned, ….. ")

The Archimedes Foundation and Kami Forskningsstiftelse are acknowledged for financial support.

I am very thankful to my parents and brother in Estonia for everything they have done for me and given to me.

Katrin! Your love and support have given me the strength to continue.
Suur aitäh!

Arvi Liivat

References

[1] USDOE, *International Energy Information at a Glance*, http://www.eia.doe.gov/international, retrieved in April 2007.

[2] A. Volta, *Philos. T. Roy. Soc.*, 90 (1800) 403.

[3] M. Faraday, *Experimental Researches in Electricity*, Vol. 1, London, 1849.

[4] A. Nytén, A. Abouimrane, M. Armand, T. Gustafsson, J.O. Thomas, *Electrochem. Commun.*, 7 (2005) 156.

[5] F. Gray, *Polymer Electrolytes*, The Royal Society of Chemistry, Cambridge, 1997.

[6] P.V. Wright, *Brit. Polym. J.*, 7 (1975) 319.

[7] M. Armand, *Annu. Rev. Mater. Sci.*, 16 (1986) 245.

[8] D.F. Shriver, R. Dupon, M. Stainer, *J. Power Sources*, 9 (1983) 383.

[9] C. Berthier, W. Gorecki, M. Minier, M. Armand, J.M. Chabagno, P. Rigaud, *Solid State Ionics*, 11 (1983) 91.

[10] J. MacCallum, C. Vincent (eds.), *Polymer Electrolyte Reviews 1 and 2*, Elsevier, London, 1987.

[11] M.A. Ratner, D.F. Shriver, *Chem. Rev.*, 88 (1988) 109.

[12] F. Croce, G.B. Appetecchi, L. Persi, B. Scrosati, *Nature*, 394 (1998) 456.

[13] Y. Inaguma, C. Liquan, M. Itoh, T. Nakamura, T. Uchida, H. Ikuta, M. Wakihara, *Solid State Commun.*, 86 (1993) 689.

[14] J.L. Briant, G.C. Farrington, *J. Electrochem. Soc.*, 128 (1981) 1830.

[15] P. Bruce (ed.), *Solid State Electrochemistry*, Cambridge University Press, Cambridge, 1995.

[16] R. Kaber, L. Nilsson, N.H. Andersen, A. Lundén, J.O. Thomas, *J. Phys. Condens. Matt.*, 4 (1992) 1925.

[17] P.V. Wright, Y. Zheng, D. Bhatt, T. Richardson, G. Ungar, *Polym. Int.*, 47 (1998) 34.

[18] Y. Zheng, P.V. Wright, G. Ungar, *Electrochim. Acta*, 45 (2000) 1161.

[19] Y. Zheng, A. Gibaud, N. Cowlam, T.H. Richardson, G. Ungar, P.V. Wright, *J. Mater. Chem.*, 10 (2000) 69.

[20] Y. Zheng, J. Lui, G. Ungar, P.V. Wright, *Chem. Rec.*, 4 (2004) 176.

[21] S. Béranger, M.H. Fortier, D. Baril, M.B. Armand, *Solid State Ionics*, 148 (2002) 437.

[22] D. Golodnitsky, E. Livshits, E. Peled, *Macromol. Symp.*, 203 (2003) 27.

[23] Y.G. Andreev, P.G. Bruce, *J. Phys. Condens. Matt.*, 13 (2001) 8245.
[24] G.S. MacGlashan, Y.G. Andreev, P.G. Bruce, *Nature*, 398 (1999) 792.
[25] Z. Gadjourova, D. Martin y Marero, K.H. Andersen, Y.G. Andreev, P.G. Bruce, *Chem. Mater.*, 13 (2001) 1282.
[26] Z. Gadjourova, Y.G. Andreev, D.P. Tunstall, P.G. Bruce, *Nature*, 412 (2001) 520.
[27] W.A. Henderson, S. Passerini, *Electrochem. Commun.*, 5 (2003) 575.
[28] P.G. Bruce, *Solid State Sci.*, 7 (2005) 1456.
[29] C. Zhang, E. Staunton, Y.G. Andreev, P.G. Bruce, *JACS*, 127 (2005) 18305.
[30] Z. Stoeva, I. Martin-Litas, E. Staunton, Y.G. Andreev, P.G. Bruce, *JACS*, 125 (2003) 4619.
[31] E. Staunton, Y.G. Andreev, P.G. Bruce, *Faraday Discuss.*, 134 (2007) 143.
[32] F. Müller-Plathe, *Acta Polymer.*, 45 (1994) 259.
[33] W. Paul, G.D. Smith, *Rep. Prog. Phys.*, 67 (2004) 1117.
[34] O. Borodin, G.D. Smith, *Computational Materials Chemistry: Methods and Applications*, Ch. 2, Kluwer Academic Publishing, 2004.
[35] O. Borodin, G.D. Smith, *Macromolecules*, 39 (2006) 1620.
[36] M.A. Ratner, P. Johansson, D.F. Shriver, *MRS Bull.*, 25 (2000) 31.
[37] G.D. Smith, D.Y. Yoon, R.L. Jaffe, *Macromolecules*, 26 (1993) 5213.
[38] S.P. Gejji, J. Tegenfeldt, J. Lindgren, *Chem. Phys. Lett.*, 226 (1994) 427.
[39] G.D. Smith, R.L. Jaffe, H. Partridge, *J. Phys. Chem.*, A 101 (1997) 1705.
[40] P.M. Anderson, M.R. Wilson, *Mol. Phys.*, 103 (2005) 89.
[41] N.R. Dhuaml, S.P. Gejji, *Theor. Chem. Acc.*, 115 (2006) 308.
[42] P. Johansson, P. Jacobsson, *J. Power Sources*, 153 (2006) 336.
[43] S. Neyertz, D. Brown, J.O. Thomas, *Electrochim. Acta*, 40 (1995) 2063.
[44] P. Johansson, P. Jacobsson, *Electrochim. Acta*, 48 (2003) 2279.
[45] D. Brandell, A. Liivat, H. Kasemägi, A. Aabloo, J.O. Thomas, *J. Mater. Chem.*, 15 (2005) 1422.
[46] D. Frenkel, B. Smit, *Understanding Molecular Simulation*, Academic Press, London, 2002.
[47] W. Smith, T. Forester, *The DL_POLY project.*, Technical report, TCS Division, Daresbury Laboratory, Daresbury, Warrington, WA4 4AD, UK.
[48] W. Smith, C.W. Yong, P.M. Rodger, *Mol. Simulat.*, 28 (2002) 385.
[49] S. Neyertz, D. Brown, J.O. Thomas, *J. Chem. Phys.*, 101 (1994) 10064.
[50] R.L. Jaffe, G.D. Smith, D.Y. Yoon, *J. Phys. Chem.*, 97 (1993) 12752.
[51] O. Borodin, G.D. Smith, *J. Phys. Chem.*, B 107 (2003) 6801.
[52] A. Aabloo, J.O. Thomas, *Comput. Theor. Polym. S.*, 7 (1997) 47.

[53] A. Aabloo, J.O. Thomas, *Electrochim. Acta*, 43 (1998) 1361.
[54] A. Aabloo, J.O. Thomas, *Solid State Ionics*, 143 (2001) 83.
[55] S. Neyertz, D. Brown, J.O. Thomas, *Comput. Polymer Sci.*, 5 (1995) 107.
[56] D. Brandell, M. Klintenberg, A. Aabloo, J.O. Thomas, *Int. J. Quant. Chem.*, 80 (2000) 799.
[57] D. Brandell, M. Klintenberg, A. Aabloo, J.O. Thomas, *J. Mater. Chem.*, 12 (2002) 565.
[58] D. Brandell, M. Klintenberg, A. Aabloo, J.O Thomas, *Macromol. Symp.*, 186 (2002) 51.
[59] H. Kasemägi, M. Klintenberg, A. Aabloo, J.O. Thomas, *J. Mater. Chem.*, 11 (2001) 3191.
[60] H. Kasemägi, M. Klintenberg, A. Aabloo, J.O. Thomas, *Solid State Ionics*, 147 (2002) 367.
[61] H. Kasemägi, M. Klintenberg, A. Aabloo, J.O. Thomas, *Electrochim. Acta*, 48 (2003) 2273.
[62] A. Hektor, M. Klintenberg, A. Aabloo, J.O. Thomas, *J. Mater. Chem.*, 13 (2003) 214.
[63] J. Karo, A. Aabloo, J.O. Thomas, *Solid State Ionics*, 176 (2005) 3041.
[64] O. Borodin, G.D. Smith, R.L. Jaffe, *J. Comput. Chem.*, 22 (2001) 641.
[65] T.A. Halgren, *JACS*, 114 (1992) 7827.
[66] W.A. Henderson, N.R. Brooks, W.W. Brennessel, V.G. Young, *Chem. Mater.*, 15 (2003) 4679.
[67] Y.G. Andreev, V. Seneviratne, M. Khan, W.A. Henderson, R.E. Frech, P.G. Bruce, *Chem. Mater.*, 17 (2005) 767.
[68] W.A. Henderson, N.R. Brooks, V.G. Young, *Chem. Mater.*, 15 (2003) 4685.
[69] V. Seneviratne, R. Frech, J. Furneaux, M. Khan, *J. Phys. Chem.*, B 108 (2004) 8124.
[70] W.A. Henderson, N.R. Brooks, V.G. Young, *JACS*, 125 (2003) 12098.
[71] A. Bhattacharyya, J. Fleig, Y.G. Guo, J. Maier, *Adv. Mater.*, 17 (2005) 2630.
[72] T. Proffen, R.B. Neder, *J. Appl. Crystallogr.*, 30 (1997) 171.
[73] C. Burba, R. Frech, *J. Phys. Chem.*, B 109 (2005) 15161.
[74] J. Grondin, L. Ducasse, J.L. Bruneel, L. Servant, J.-C. Lassègues, *Solid State Ionics*, 166 (2004) 441.
[75] L. Ducasse, M. Dussauze, J. Grondin, J.-C. Lassègues, C. Naudin, L. Servant, *Phys. Chem. Chem. Phys.*, 5 (2003) 567.
[76] Y.G. Andreev, *Private Communication*.
[77] D. Brandell, A. Liivat, A. Aabloo, J. Thomas, *Chem. Mater.*, 17 (2005) 3673.
[78] A.M. Christie, S.J. Lilley, E. Staunton, Y.G. Andreev, P.G. Bruce, *Nature*, 433 (2005) 50.
[79] A. Liivat, A. Aabloo, J.O. Thomas, *J. Comput. Chem.*, 26 (2005) 716.

[80] J.-M. Tarascon, M. Armand, *Nature*, 414 (2001) 359.
[81] J. Maier, *Nat. Mater.*, 4 (2005) 805.
[82] F. Vullum, D. Teeters, A. Nytén, J.O. Thomas, *Solid State Ionics*, 177 (2006) 2833.
[83] H. Kasemägi, A. Aabloo, M. Klintenberg, J.O. Thomas, *Solid State Ionics*, 168 (2004) 249.
[84] D. Barbier, D. Brown, A.C. Grillet, S. Neyertz, *Macromolecules*, 37 (2004) 4695.
[85] G. Scharfenberger, W.H. Meyer, G. Wegner, M. Schuster, K.D. Kreuer, J. Maier, *Fuel Cells*, 6 (2006) 237.

Appendix

Interatomic interactions are described by the sum:

$$U = \sum_{i,j} U_{bond}(r_{ij}) + \sum_{i,j,k} U_{bend}(\theta_{ijk}) + \sum_{i,j,k,n} U_{tors}(\varphi_{ijkn}) + \sum_{i,j} U_{non-bond}(r_{ij}),$$

where bond-stretching: $U_{bond}(r_{ij}) = \frac{k_{ij}}{2}(r_{ij} - r_{0ij})^2$,

valence-angle bending: $U_{bend}(\theta_{ijk}) = \frac{k_{ijk}}{2}(\theta_{ijk} - \theta_{0ijk})^2$

and torsional rotation potentials (different for methyl-group hydrogens):

$$U_{tors}(\varphi_{ijkn}) = \sum_{x=1}^{6} a_{x,ijkn}(-1)^x \cos^x(\varphi_{ijkn}),$$

$$U_{tors}^{meth}(\varphi_{ijkn}) = \frac{k^{meth}}{2}\left[1 - \cos(3\varphi_{ijkn})\right]$$

are imposed on bonded atoms with indices i,j,k,n. For interactions between non-bonded atoms, the following forms apply:

$$U_{non-bond}(r_{ij}) = A_{ij}^B \exp(-B_{ij}^B r_{ij}) - \frac{C_{ij}^B}{r_{ij}^6} - \frac{D_{ij}^B}{r_{ij}^4} + \frac{q_i q_j}{4\pi\varepsilon_0 r_{ij}}$$

$$U_{non-bond}(r_{ij}) = \frac{A_{ij}^{LJ}}{r_{ij}^{12}} - \frac{C_{ij}^{LJ}}{r_{ij}^6} + \frac{q_i q_j}{4\pi\varepsilon_0 r_{ij}}$$

where k_{ij}, k_{ijk}, r_{0ij}, θ_{0ijk}, $a_{x,ijkn}$, A^B_{ij}, B^B_{ij}, C^B_{ij}, D^B_{ij}, A^{LJ}_{ij}, C^{LJ}_{ij}, q_i, q_j are constants depending on atom-types.

Table A-I. force-field parameters for SiF_6^{2-}/$LiPF_6$-PEO_6. Energy in unit of kcal/mol; F_P and F_{Si} refer to fluorine atoms in PF_6^- and SiF_6^{2-} respectively.

Atom pair	**A**	**B**	**C**	**D**
Si-Si	678890	6.0900	88	225
F_{Si}-F_{Si}	14678	3.2008	225	33
Si-F_{Si}	99823	4.6454	160	210
Si-Li	441133	6.0628	7	65
Si-F_P	303613	5.3181	84	277
Si-P	1842400	5.5451	455	496
Si-C	146503	4.6979	239	0
Si-O	198944	5.0572	130	5
Si-H	69726	5.1241	67	0
F_{Si}-Li	19039	4.0099	12	75
F_{Si}-P	270906	4.1004	727	121
F_{Si}-F_P	44643	3.8734	134	36
F_{Si}-C	21542	3.2533	382	0
F_{Si}-C	29253	3.6126	208	0
F_{Si}-H	10252	3.6794	107	0

Acta Universitatis Upsaliensis

Digital Comprehensive Summaries of Uppsala Dissertations from the Faculty of Science and Technology 303

Editor: The Dean of the Faculty of Science and Technology

A doctoral dissertation from the Faculty of Science and Technology, Uppsala University, is usually a summary of a number of papers. A few copies of the complete dissertation are kept at major Swedish research libraries, while the summary alone is distributed internationally through the series Digital Comprehensive Summaries of Uppsala Dissertations from the Faculty of Science and Technology. (Prior to January, 2005, the series was published under the title "Comprehensive Summaries of Uppsala Dissertations from the Faculty of Science and Technology".)

Distribution: publications.uu.se
urn:nbn:se:uu:diva-7853

ACTA
UNIVERSITATIS
UPSALIENSIS
UPPSALA
2007

Paper I

Development of a Force Field for Li_2SiF_6

ANTI LIIVAT,[1] ALVO AABLOO,[2] JOHN O. THOMAS[3]
[1]*Institute of Material Physics, University of Tartu, Tähe 4, 51010 Tartu, Estonia*
[2]*Institute of Technology, Tähe 4, 51010 Tartu, Estonia*
[3]*Department of Materials Chemistry, Box 538, Uppsala University, SE-75121 Uppsala, Sweden*

Received 20 July 2004; Accepted 21 December 2004
DOI 10.1002/jcc.20209
Published online in Wiley InterScience (www.interscience.wiley.com).

Abstract: A force field has been developed for Li_2SiF_6 for subsequent use in Molecular Dynamics (MD) simulations involving Li^+ and SiF_6^{2-} ions in a polymer electrolyte host. Both *ab initio* calculations and available empirical data have been used. The force field has been verified in simulations of the crystal structure of Li_2SiF_6 in two different space groups: *P321* and $P\bar{3}m1$. The use of MD simulation to assess the correct space group for Li_2SiF_6 shows that it is probably *P321*.

 J Comput Chem 26: 716–724, 2005

Key words: force field; molecular dynamics simulation; polymer electrolytes

Introduction

Large near-spherical polyatomic anions have attracted much attention as promising Li–salt anions in battery electrolytes through their ability to suppress ion-pairing. So far, singly charged anions such as PF_6^- have been adopted successfully in some Li–ion battery concepts. Recently, crystalline $(PEO)_6$–$LiXF_6$, X=P, As, Sb systems have been studied, in which the Li^+ ions are well separated, lying along the axes of cylindrical double hemi-helical PEO channels;[1] remarkably, somewhat better Li^+ conductivity has been found compared to their amorphous counterparts. In this present work, we treat the doubly charged anion SiF_6^{2-} in the Li_2SiF_6 salt. A ca. 1% substitution of the SiF_6^{2-} anion into these $(PEO)_6$–$LiXF_6$ systems permits the addition of the extra Li^+ ions into the system, and has been found to further improve the Li^+ conductivity.[2] A viable potential for the Li^+–SiF_6^{2-} system is thus needed for subsequent MD simulation to understand the Li^+ conductivity mechanism in these new ordered polymer electrolyte systems.

Ab initio quantum chemical calculations in combination with classical Molecular Dynamics (MD) simulation have earlier been used to produce reliable force fields for electrolyte salts involving the PF_6^- ion.[3] In these calculations, the MD force field for the salt was optimized for a polyethylene-oxide (PEO) polymer host environment. Here we take a different approach; we optimize the force field for the crystal structure of Li_2SiF_6. Although the crystal structure of this compound is not available, we have access to the isomorphous structure Na_2SiF_6.[4,5] Our derived potentials for the Li^+–SiF_6^{2-} system have subsequently been verified in MD simulations of the Li_2–SiF_6 crystal structure, and used to ascertain which of the originally proposed space groups for Na_2SiF_6 ($P\bar{3}m1$ or *P321*)[6] is correct.

Quantum Mechanical Studies

General Strategy

Calculations of the type discussed in ref. 3 for the O_h symmetric anion PF_6^- have inspired the approach taken in this work. Gaussian 98[7] software was used for all the quantum chemistry calculations. The Hartree–Fock (HF) calculations were complemented by Møller–Plesset perturbation (MP2) and DFT methods (BLYP,[8] B3LYP,[9] and B3PW91[10]), taking account of electron correlation.

Double-zeta (D95),[11] triple-zeta split valence (6-311G),[12] and correlation consistent (cc-VDZ)[13] basis sets (augmented with diffuse functions) were all tested for the anion. An optimized basis set in a reduced 5s2p1d form was used for Li^+.[14] With the exception

Correspondence to: J. O. Thomas; e-mail: josh.thomas@mkem.uu.se

Contract/grant sponsor: Swedish Science Council (V.R.)

Contract/grant sponsor: Swedish Institute (SI)

Contract/grant sponsor: Estonia Science Foundation (ETF); contract/grant number: 4513

Contract/grant sponsor: Swedish National Infrastructure for Computing (SNIC)

Contract/grant sponsor: Kami Research Foundation (Stipend to A.L.)

Contract/grant sponsor: World Federation of Scientists (WFS; Stipend to A.L.)

Table 1. Optimized Geometries and Partial Charges for SiF_6^{2-} Using Different Levels of Theory and Basis Sets.

Basis set		Level of theory	Si–F distance (Å)	Si charge (e)
Si	F			
D95+(2*d*)	D95+(*d*)	HF	1.699	2.201
		MP2	1.732	2.100
		BLYP	1.753	2.128
		B3LYP	1.730	2.127
		B3PW91	1.726	2.021
6-311+G(2*df*)	6-311+G(2*df*)	HF	1.692	2.129
		MP2	1.716	2.056
		BLYP	1.749	2.102
		B3LYP	1.725	2.094
		B3PW91	1.721	1.990
AUG-cc-pVDZ	AUG-cc-pVDZ	HF	1.720	2.097
		MP2	1.752	2.055
		BLYP	1.779	2.139
		B3LYP	1.754	2.100
		B3PW91	1.750	1.984

of the cc-VDZ set, the choice of basis set was identical to that used by Borodin et al.[3] In the MP2 calculations, the electron correlation is extended to the core electrons unless stated otherwise. Partial charges on the atoms were obtained using the CHELPG method[15] implemented in Gaussian 98. Conformational energies, partial charges, and polarizabilities obtained from the first-principle calculations were fitted to Buckingham and Coulomb potentials [see eqs. (1)–(3)] for the MD simulations. The program Origin 6.1 was used for data fitting.

The SiF_6^{2-} Anion: Geometry and Partial Charges

The geometry of the anion was optimized without constraints. An O_h symmetry state was obtained irrespective of the theory level used; the results are summarized in Table 1. The Si–F bond lengths obtained from the MP2, B3LYP, and B3PW91 calculations yield similar values using the same basis set. It would seem that a more complete basis set involving *f*-functions stabilizes the Si–F distance closer to their experimental values: 1.68–1.72 Å.[6] We can note here that Mulliken charges were rather close to the CHELPG results; for example, in HF/6-311+G(2*df*), Mulliken gave q_{Si} = 1.97 and CHELPG gave q_{Si} = 2.13. The higher ionicity of HF results in shorter bond lengths and higher charges, but the effect is not as large as for the PF_6^- anion. This suggests a smaller electron correlation contribution.

In the following calculations, we choose to exploit the B3PW91 functional because it gives lower partial ionic charges than HF and the shortest bond lengths of the DFT methods tested. The 6-311+(2*df*) basis was also preferred, because it best reproduced the experimental Si–F bond lengths (see above). This approach was used throughout unless otherwise stated.

Bonded Interactions

As in ref. 3, we limit ourselves to independent bond stretch and angle bend calculations. Starting from the geometry optimized in B3PW91/6-311+G(2*df*), the Si–F bond-stretching energy is probed in two different ways: (1) one of the six Si–F bonds is stretched, keeping the others fixed; the angles are also kept fixed; (2) all six Si–F bonds are stretched simultaneously; the energy for each bond is assumed to be 1/6 of the total energy. The resulting energy curves were fitted to harmonic potential functions with force constant k_r and equilibrium distance r_0:

$$E(r - r_0) = \frac{1}{2} k_r (r - r_0)^2 \quad (1)$$

The results are plotted in Figure 1. Within ±0.1 Å from equilibrium, the DFT energy can be fitted to a harmonic potential with a maximum deviation of 0.6 kcal/mol. The energy of the F–Si–F angle bend was probed by deforming the anion within two

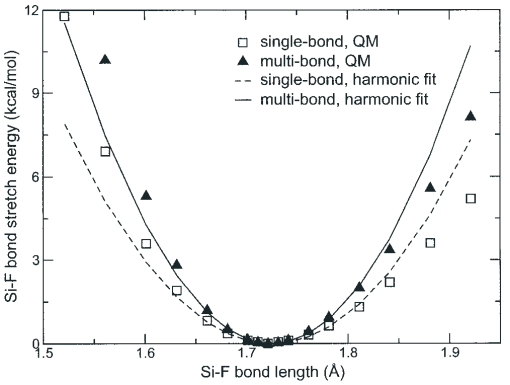

Figure 1. Si—F bond-stretch energy; the B3PW91/6-311+G(2*df*) values fitted to a harmonic potential function [eq. (1)].

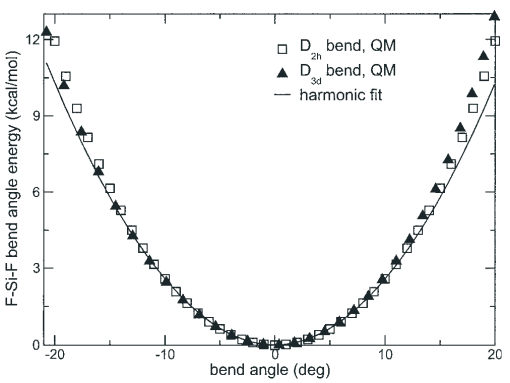

Figure 2. F—Si—F angle-bending energy (from 90°) from B3PW91/6-311+G(2*df*) calculations fitted to a harmonic potential [eq. (2)].

Table 2. Bonded Interaction Potential Parameters for the SiF_6^{2-} Anion; see eqs. (1) and (2) for the Potential Expressions.

Type	Parameter	Value	Unit	Comment
Harmonic stretch	k_r^s	380	kcal · mol^{-1} · Å^{-2}	Single-bond fit
Harmonic stretch	k_r^m	556	kcal · mol^{-1} · Å^{-2}	Multi-bond fit
Harmonic stretch	r_0	1.725	Å	Equilibrium Si–F distance
Harmonic bend	k_θ	169	kcal · mol^{-1} · rad^{-2}	D_{3d} and D_{2h}
Harmonic bend	θ_0	$\pi/2$	rad	D_{3d} and D_{2h}

symmetry conformations: D_{2h} and D_{3d}. In both cases, the Si–F bond lengths were fixed to values optimized in the O_h conformation. The resulting energy curves were fitted to the harmonic expression:

$$E(\theta - \theta_0) = \frac{1}{2} k_\theta (\theta - \theta_0)^2 \qquad (2)$$

where k_θ and θ_0 are adjustable parameters (Fig. 2). Note that the angle-bend potential [eq. (2)] is harmonic to within 1 kcal/mol at ±15° from equilibrium geometry. Parameters derived for the bonded interactions in MD force field are listed in Table 2.

The SiF_6^{2-} . . . SiF_6^{2-} Interaction

The repulsion energy between SiF_6^{2-} anions is probed here by calculating the interaction energy only in a C_{3v} symmetric close-packed configuration as a function of Si–Si distance. This local configuration is the most likely in a crystal structure. Both anions were constrained individually to maintain their O_h ground-state conformation. The calculations we performed at a DFT/B3PW91/6-311+G(2*df*) level and complemented by MP2-level calculations (using the same basis set and only valence electron correlation) to check long-range behavior. A counterpoise BSSE (Basis Set Superposition Error) correction was applied to the MP2 energies, while DFT energies are uncorrected. Surprisingly, the uncorrected DFT and the corrected MP2 energy curves almost coincide throughout the Si–Si distance range probed (Fig. 3).

The calculated energy points in Figure 4 were fitted to the force-field function:

$$E(r_{ij}) = A_{ij}\exp(-B_{ij}r_{ij}) - \frac{D_{ij}}{r_{ij}^4} - \frac{C_{ij}}{r_{ij}^6} + 332.07\,\frac{q_i q_j}{r_{ij}} \qquad (3)$$

Overparametrization has been avoided by eliminating parameters unlikely to contribute significantly to the calculated energy: (1) repulsion, induction, and dispersion terms for Si–Si and Si–F pairs have been omitted from the fitting procedure, because these are expected to be small (<1 kcal/mol); (2) attraction parameters D_{FF}, D_{SiF}, and C_{FF} were fixed; (3) fixed parameters were estimated from semiempirical data (see below).

High-quality Buckingham force-field parameters for Si were obtained from the thesis work of Gerdy:[16] A_{SiSi} = 678,890 kcal/mol, B_{SiSi} = 3.0414 Å^{-1}. Consistent with earlier calculations,[17] atomic charge partitioning in the current work (Table 1) predicts

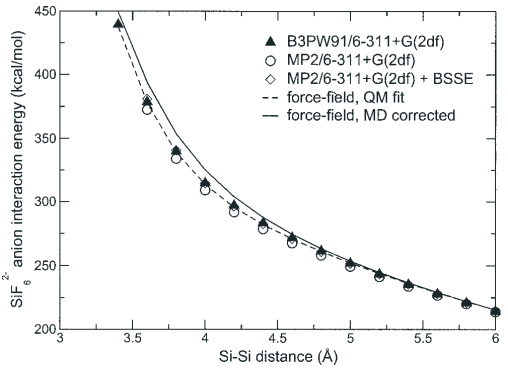

Figure 3. SiF_6^{2-} . . . SiF_6^{2-} interaction energy as a function of Si–Si distance; the force field [eq. (3)] is fitted to quantum chemical (QM) data (dashed line) and obtained from simulation-corrected parameters (solid line).

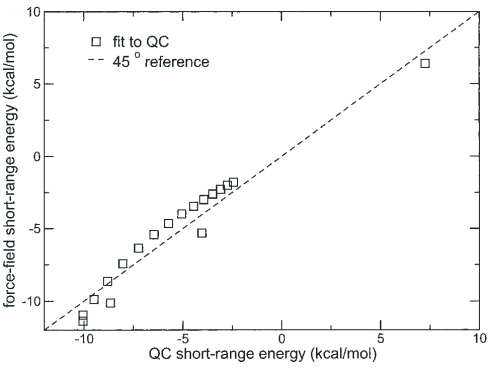

Figure 4. A plot showing the accuracy of the SiF_6^{-2} . . . SiF_6^{-2} short-range energy fit; the dashed line represents a perfect fit.

Table 3. Nonbonded Interaction Potential Parameters for SiF_6^{2-} Anions; see eq. (3) for the Potential Expression.

Atom pair		A (kcal · mol^{-1})	B (Å^{-1})	C (kcal · mol^{-1} Å^{-6})	D (kcal · mol^{-1} Å^{-4})	Comment
F	F	55010	3.8951	225	33	Fitted
Si	F	193250	4.9925	160	210	Combination rules
Si	Si	678890	6.0900	88	225	Semiempirical
F	F	14678	3.2008	225	33	Adjusted after MD
Si	F	99823	4.6454	160	210	Adjusted after MD

that hexa-coordinated Si carries a substantial (ca. +2) ionic charge. This is believed to be due to the strong electron-withdrawal effects of F atoms, making the 2d-orbitals in SiF_6^{2-} only slightly more populated than in covalently bonded SiF_4 (−0.55e vs. −0.40e). Accordingly, the Buckingham exponent parameter (B_{SiSi}) was scaled following the rule given in ref. 18: $B \sim a\sqrt{IP}$, IP implying an ionization potential for the atom (or ion), and giving the new parameter $B_{Si^{2+}Si^{2+}} \approx \frac{1}{2} B_{SiSi}$, because the third ionization potential IP(III) for Si is roughly four times higher than the first IP(I).

The attractive charge-induced dipole interactions are incorporated into the force field in the following mean-field approximation:[14]

$$E_{ind}(r_{ij}) = -\frac{D_{ij}}{r_{ij}^4} \tag{4}$$

where

$$D_{ij} = 332.07\,\frac{q_i^2\alpha_j + q_j^2\alpha_i}{2} \tag{5}$$

The *ab initio* B3PW91/6-311+G(2*df*) and HF/6-311+G(2*df*) calculations produce anion polarizabilities 5 Å^3 and 4 Å^3, respectively. It is likely that the HF value is better for an ion in a bulk environment; to estimate the D_{ij} coefficients, we partition them into the sum of atomic polarizabilities[19] by taking $\alpha(F) = 0.6$ Å^3,[3] to give $\alpha(Si) \approx 4 - 6 \cdot 0.6 = 0.4$ Å^3.

The initial C_{ij} parameters were estimated from the Slater–Kirkwood formula:[20]

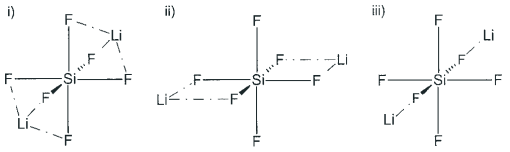

Figure 5. Local configurations for Li_2SiF_6; (1) threefold coordination of Li^+ to fluorines: D_{3d} and C_{3v} symmetries; (2) twofold coordination of Li^+ to fluorines: D_{2h} and C_{2v} symmetries; (3) onefold coordination of Li^+ to fluorines: D_{4h} and C_{4v} symmetries.

$$C = 657.2\,\frac{\alpha_i\alpha_j}{\left(\frac{\alpha_i}{N_i}\right)^{1/2} + \left(\frac{\alpha_j}{N_j}\right)^{1/2}}$$

Polarizabilities α_i are in Å^3 and the effective number of electrons N_i is calculated from eq. (6) in ref. 20:

$$\frac{N_i}{N_{ext}} = 1 + \left(1 - \frac{N_{ext}}{N_{int}}\right)\left(\frac{N_{int}}{N_{tot}}\right)^2 \tag{6}$$

where N_{int}, N_{ext}, and N_{tot} are the number of electrons in the core, the valance shells and in total. The effective number of electrons is an estimate of the number of electrons participating in long-range interactions: $N_{Si^{2+}} = 3.1$, $N_{F^-} = 6.7$, and $N_{Li^+} = 0.2$. The effective number of electrons in a molecule (N_{eff}) is estimated from eq. (8) in ref. 20:

$$\frac{N_{eff}}{N_{tot}} = 1 - \frac{N_{nb}N_b}{N_{tot}^2} \tag{7}$$

where N_b and N_{nb} are the number of bonded and nonbonded electrons in the molecule. For SiF_6^{2-}, this gives 39 (the same as for an SF_6 molecule); slightly less than the value of 43.5 obtained above from the partitioning.

The estimated force-field parameter values were scaled down to give a satisfactory fit to *ab initio* energies. The quality of the fit is shown in Figure 4. The final parameters are given in Table 3.

The B_{FF} parameter was later scaled down to maintain a realistic pressure in the MD simulation box.[21] A_{FF} was also scaled down on the basis of the Born–Mayer–Huggins potential model[22] with $A \sim \exp(d/B)$, where d is the size of the atom involved. The scaling was done because the anion–anion Potential Energy Surface (PES) was only scanned partially and could contain significant conformation-dependent errors. The other two parameters (A_{SiF} and B_{SiF}) were coupled to A_{FF}, B_{FF} via the combination rules.

The $Li^+ \ldots SiF_6^{-2}$ Interaction

The energies of the three main configurations of Li_2SiF_6, as shown in Figure 5, were calculated. These involve a threefold (D_{3d}), twofold (D_{2h}), and onefold (D_{4h}) arrangement of Li^+ coordinated by F^- ions.

Because the Li^+ cation itself is rather small, it makes only a minor dispersion contribution to the mutual interaction. On the other hand, its polarizing power can necessitate a polarization function

Table 4. Binding Energies, Geometries, and Charges for the $2Li^+/SiF_6^{2-}$ Unit at Different Levels of Theory (D_{3d} Symmetry).

Basis set[a]							
Li^+	Si	F	Level of theory	$2Li^+$ binding energy (kcal/mol)	BSSE (kcal/mol)	Li–Si dist. (Å)	Si charge (e)	Li charge (e)
(1)	(2)	(3)	HF	−412.7	0.29	2.37	1.81	0.89
			MP2	−407.4	0.83	2.40	1.62	0.88
			BLYP	−405.8	0.29	2.41	1.53	0.87
			B3LYP	−410.7	0.30	2.39	1.58	0.87
			B3PW91	−408.5	0.33	2.39	1.5	0.88
(1)	(4)	(4)	HF	−416.0	0.15	2.35	1.74	0.89
			MP2	−412.0	0.57	2.37	1.58	0.88
			BLYP	−409.5	0.13	2.39	1.53	0.86
			B3LYP	−414.4	0.14	2.36	1.57	0.87
			B3PW91	−412.2	0.18	2.37	1.49	0.87
(1)	(5)	(5)	HF	−419.2	0.20	2.34	1.64	0.86
			MP2	−412.2	0.53	2.37	1.50	0.86
			BLYP	−409.5	0.15	2.38	1.46	0.84
			B3LYP	−415.5	0.17	2.36	1.49	0.85
			B3PW91	−413.7	0.18	2.36	1.41	0.85

[a]Basis set key: (1) [5*s*2*p*1*d*] from [3]; (2) D95+(2*d*); (3) D95+(*d*); (4) 6-311+G(2*df*); (5) AUG-cc-pVDZ.

for the counteranion. The basis set for Li^+ [5*s*2*p*1*d*] was taken from ref. 14 because it gives a better description of the 1*s* electrons. Several methods and basis sets were tested (as above) in the optimization of the molecular geometry. The CHELPG charges, equilibrium Si–Li^+ distances and Li^+ binding energies with their counterpoise BSSE corrections are given for the D_{3d} symmetry case in Table 4. Note that the BSSE values are small (<0.1% of total binding energy) and can be neglected. With the basis set involving *f*-functions for the heavy atoms, the B3PW91 and MP2 energies are closest; whereas charges correspond better between B3LYP and MP2. Note that the energy to remove two Li^+ ions from the anion is rather high, ca. 410 kcal/mol. This also explains the short Li–Si distance: 2.37 Å.

The lowest energy conformation is D_{3d}, giving a global minimum, whereas the D_{2h} and D_{4h} conformations are unstable, giving 2 and 4 imaginary frequencies, respectively.

The $Li^+ \ldots SiF_6^{2-} \ldots Li^+$ Potential Energy Surface (PES)

The B3PW91/6-311+G(2*df*) method was chosen to probe the Li^+ interaction energy with the anion, because it gives MP2-level accuracy in energies at a low computational cost. Two approaches were made in constraining the Li^+ coordination to fluorine to three-, two-, and onefold: (1) D_{3d}, D_{2h}, and D_{4h} symmetries where superimposed; (2) C_{3v}, C_{2v}, and C_{4v} symmetries were superimposed with only one Li^+–Si distance varied.

Within these constraints, the rest of the geometry was optimized at every step. The energy of a $2Li^+/SiF_6^{2-}$ unit is defined as:

$$E = E(Li_2SiF_6) - 2E(Li^+) - E(SiF_6^{-2}) \quad (8)$$

The dependence on Si–Li distance is shown in Figures 6 and 7. As in the $LiPF_6$ case, there is a hierarchy of energetically stable symmetric configurations as the Li–Si distance increases, but the effect is less pronounced. The D_{3d} configuration is favored up to 2.75 Å. Up to 3.3 Å, two- and threefold coordinated configurations fall within a few kcal/mol, whereafter, D_{4h} dominates. The behavior is different in the asymmetric case where, for <2.85 Å and >3.0 Å, C_{3v} dominates; the C_{4v} configuration is energetically unfavorable at all distances. Note that the anion dissociates to form LiF_2 and SiF_4 in D_{4h} and C_{4v} configurations, respectively, at an Li–Si distance of around 3.5 Å.

The repulsive component was extracted from the complete QM data for all six configurations. This was done by replacing the Li^+ ions in all the energy calculations described above by positive

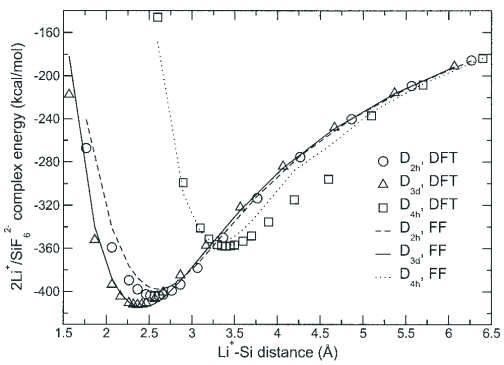

Figure 6. The $Li^+ \ldots SiF_6^{-2} \ldots Li^+$ potential energy surface from B3PW91/6-311+G(2*df*) level DFT calculations and fitted to force-field functions [eq. (3)]; the Li^+–Si distance is varied for threefold (D_{3d}), twofold (D_{2h}), and onefold (D_{4h}) Li–F coordination.

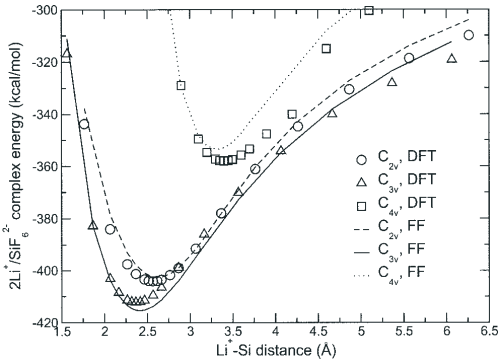

Figure 7. The $Li^+ \ldots SiF_6^{-2} \ldots Li^+$ potential energy surface from B3PW91/6-311+G(2*df*) level DFT calculations and fitted to force field (FF) [eq. (3)] functions; the Li^+–F distance is varied for threefold (C_{3v}), twofold (C_{2v}), and onefold (C_{4v}) Li–F coordination.

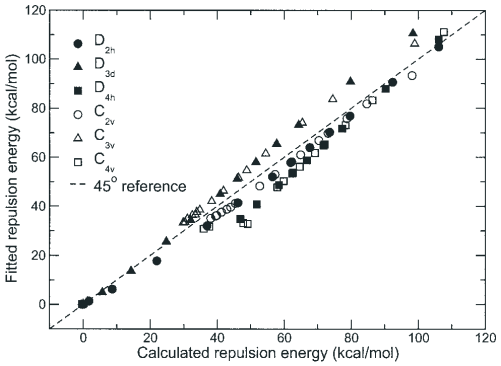

Figure 8. The accuracy of the $Li^+ \ldots SiF_6^{2-} \ldots Li^+$ repulsion energy fit; a dashed line represents a perfect fit.

unit charges ($+e$). The difference between two complex energies is assumed to be repulsive due to the overlapping orbitals of the cation and anion. The energy curves obtained were fitted to the Buckingham functions in eq. (3). The optimized parameters are given in Table 5. Only A_{Li^+Si}, A_{Li^+F}, B_{Li^+Si}, and B_{Li^+F} were optimized, whereas the Li^+–Li^+ force-field parameters are those given in ref. 3. Several data sets were fitted simultaneously to the same parameters, with the unwanted dissociation regions weighted out. This fit is shown in Figure 8. Deriving a simple force-field description involves making compromises; the best fit is here achieved for Si–Li^+ distances >2.9 Å; this is a typical distance in related crystal structures such as Li_2GeF_6.[23] and Li_2MnF_6.[24] The energy curves corresponding to our QM calculations are given in Figures 6 and 7. Apart from the dissociation path, the description of the system using our classical force field agrees qualitatively with QM predictions; deviations are within only a few kcal/mol in structurally relevant regions.

MD Simulation of the Li_2SiF_6 Structure

The Model and the Methods

The bulk system was studied using the Molecular Dynamics (MD) simulation method based on Newtonian dynamics for a many-particle system, where the time evolution of the positions and velocities of the atoms and ions is obtained by numerical integration of the equations of motion. Forces are obtained from the potential functions derived in the previous sections [eqs. (1), (2), and (3)] with the force-field parameters given in Tables 2, 3, and 5. Note that multibond harmonic stretch force constant was used in simulations.

MD simulations of Li_2SiF_6 were undertaken for a $2 \times 2 \times 3$ unit cell MD box; dimensions: $16.44 \times 16.44 \times 13.68$ Å^3 with periodic boundary conditions; the total number of atoms in the MD box was 324. Two different space groups were tested:[25] $P\bar{3}m1$ (No. 164) (Model A) and *P321* (No. 150) (Model B), following the published structures for Na_2SiF_6 (refs. 4 and 6, respectively). The P1 structure of Na_2SiF_6[26] was also tested, but no statistically significant differences were found compared to *P321*—the pair radial distribution functions were also indistinguishable.

The unit-cell parameters were rescaled to the values published in ref. 5: $a = 8.22$, $c = 4.56$ Å. The two structures are shown in Figure 9. The centrosymmetric structure (model A) differs from the noncentrosymmetric (model B) in the higher deformation of its SiF_6 octahedra and in the alignment of the Li^+-ions at $z = 0$.

All simulations were run in a NVT Nose–Hoover[27] thermostat heat-bath at 298 K for 600 ps following an equilibration period of 50 ps. Ewald summation was exploited to calculate the coulombic forces. The integration time step was 0.1 fs, and data were sampled every 1000 time steps. Under the simulation conditions chosen, longer simulation times were not motivated. Simulations were run both on a local Linux PC cluster and at the Linköping NSC computer Monolith. A total of 5500 CPU h were used, of which 3200 CPU h were consumed on Monolith. A local version of

Table 5. The Parameters in the Li^+/SiF_6^{2-} Force Field; see eq. (3).

Atom pair		A (kcal · mol^{-1})	B (Å^{-1})	C (kcal · mol^{-1} Å^{-6})	D (kcal · mol^{-1} Å^{-4})	Comment
Li	Li	44195	7.2770	0	6.6	From [3]
Si	Li	441133	6.0901	6.8	64.5	A, B fitted; C, D estimated
F	Li	19039	4.0099	11.7	75	A, B fitted; C, D estimated

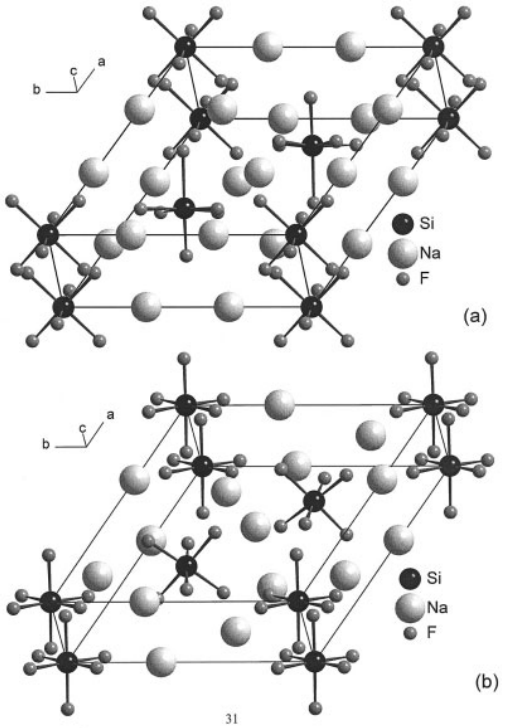

Figure 9. The Na_2SiF_6 structures: (a) space group $P\bar{3}m1$ (Model A); (b) space group *P321* (Model B). These are the start structures in the MD simulations.

DL_POLY[28] was used to perform the simulations. The DL_POLY implementation of the pressure profile is used for making adjustments in force-field parameters.

MD Simulation Results and Discussion

Force-Field Adjustments

The force field obtained from fitting the quantum chemical data was tested for Models A and B. The negative, rather uniform, pressure of ca. −50 kbar indicates that the interactions were too attractive. The potential parameter B_{FF} was adjusted to give pressures close to atmospheric. This was achieved by manually reducing the parameter and rerunning the simulation. The procedure was continued until the pressure was reduced to the magnitude of its root-mean-square fluctuation: 2.8 kbars for both models. This adjustment was similar for both structure models.

The validity of our approach was tested in the final stages in an NpT run; the average cell parameters did not differ from the reference values by more than 0.2% (valued obtained: $a = b = 8.21$ Å, $c = 4.55$ Å). This is equivalent to tuning the force-field parameters to fit the known MD box dimensions.

Structural and Energetical Comparison of the Models

During equilibration of Model A, the harmonic bond-stretch force field significantly reduces the distortion of SiF_6 octahedra and some Li^+ ions left the 001-plane to occupy the $z = 0.5$ sites. This phenomena is favored by the high electrostatic interaction between Li^+ ions and by their smaller size compared to Na^+ ions. The structure then remained stable throughout the rest of the simulation. After initially relaxing Si and Li positions by 0.025–0.055 Å, the positions remained stable in the Model B. The energies for both models are compared in Table 6. Both van der Waals and electrostatic energies, the dominant contributors to a total energy, are similar in Models A and B. No additional changes were therefore observed for Model A after the equilibration phase. The root-mean-square deviation of F–Si–F angles from 90° is 3° and 2° for Models A and B, respectively. Inspection of the bonding energies also reveals that anions are more distorted in Model A than Model B.

Analysis of the Simulated Asymmetric Units of the Models

Both MD models we subjected to a "folding-back" procedure in which the atom coordinates in the simulation boxes for 500 time steps where translated back into one unit cell; the symmetry operations for the modeled space groups were then applied to give a set of coordinates for each site in the original crystallographic asymmetric unit. New site coordinates were calculated as the average positions of the "folded" coordinates. Second-order anisotropic Atomic Displacement Factors (ADF) (U_{ij} in ref. 29) were then derived. This procedure could not be used directly on Model A because Li1 broke the initial Wyckoff 6g site symmetry. However, closer examination revealed that its new sites had 6h Wyckoff positions, which are allowed in the $P\bar{3}m1$ space group. About 25% the atoms at $(-x, -x, 0)$ sites and 75% of the atoms at $(x, x, 0)$ sites in the unit cell shift to $(-x, -x, 0.5)$ and $(x, x, 0.5)$

Table 6. MD Energy Profile Averages for Models A and B for Li_2SiF_6.

Model	van der Waals (kcal · mol^{-1})	Coulomb (kcal · mol^{-1})	Bond (kcal · mol^{-1})	Angle (kcal · mol^{-1})
A ($P\bar{3}m1$)	−29.6	−172.6	8.3	3.2
B (*P321*)	−33.8	−173.9	6.8	2.0

Note: Model A ($P\bar{3}m1$) broke its initial symmetry already during the equilibration phase. Energies are normalized to one Li_2SiF_6 molecule.

Table 7. The Asymmetric Unit for the Input Structure (Na_2SiF_6: expt.) (First Row) and the Simulated Structure (Li_2SiF_6: MD) (Second Row).

Model	Atom	Wyckoff position	Na_2SiF_6 (expt.)/Li_2SiF_6 (MD) x	y	z	Occ.
P$\bar{3}$m1	Si1	1a	0	0	0	1
	Si1	1a	0.000	0.000	0.000	1
	Si2	2d	$\frac{1}{3}$	$\frac{2}{3}$	0.50	1
	Si2	2d	0.333	0.665	0.497	1
	Na1	6g	$\frac{1}{3}$	0	0	1
	Li1	6g	0.351	0	0	$\frac{5}{6}$
	Na2	6h	$\frac{1}{3}$	0	$\frac{1}{2}$	0
	Li2	6h	0.307	0	0.500	$\frac{1}{6}$
	F1	6i	0.09	$-x$	0.24	1
	F1	6i	0.104	−0.103	0.202	1
	F2	6i	0.23	$-x$	0.76	1
	F2	6i	0.231	−0.232	0.728	1
	F3	6i	0.41	$-x$	0.24	1
	F3	6i	0.433	−0.433	0.273	1
P321	Si1	1a	0	0	0	1
	Si1	1a	0.000	0.000	0.000	1
	Si2	2d	$\frac{1}{3}$	$\frac{2}{3}$	0.5062	1
	Si2	2d	0.333	0.667	0.501	1
	Na1	3e	0.3790	x	0	1
	Li1	3e	0.374	0.374	0.000	1
	Na2	3f	0.7143	x	$\frac{1}{2}$	1
	Li2	3f	0.707	0.707	0.500	1
	F1	6g	0.0870	−0.0920	0.8099	1
	F1	6g	0.097	−0.106	0.780	1
	F2	6g	0.4442	−0.4010	0.7007	1
	F2	6g	0.449	−0.421	0.721	1
	F3	6g	0.2299	−0.260	0.3098	1
	F3	6g	0.221	−0.241	0.282	1

Table 8. Atomic Displacement Factors[a] (ADFs) (U_{ij} in Å^2) from MD Simulation in Space Groups *P321* and *P$\bar{3}$m1* for the Li_2SiF_6 Crystal Structure.

Space group	Site	Wyckoff position	U_{iso}	U_{11}	U_{22}	U_{33}	U_{12}	U_{13}	U_{23}
P$\bar{3}$m1	Si1	1a	0.006	0.004	0.004	0.010	0.002	0.0000	0.0000
	Si2	2d	0.008	0.008	0.009	0.005	0.003	0.0000	0.0000
	Li1	6g	0.017	0.018	0.018	0.016	0.009	0.0005	0.0010
	Li2	6h	0.010	0.009	0.008	0.013	0.004	−0.0005	−0.0010
	F1	6i	0.010	0.009	0.009	0.014	0.006	0.0000	0.0010
	F2	6i	0.012	0.0012	0.011	0.012	0.006	0.0010	−0.0023
	F3	6i	0.010	0.009	0.009	0.014	0.005	−0.0007	0.0008
P321	Si1	1a	0.004	0.004	0.004	0.005	0.002	0.0000	0.0000
	Si2	2d	0.004	0.004	0.004	0.005	0.002	0.0000	0.0000
	Li1	3e	0.009	0.009	0.009	0.008	0.004	−0.0003	0.0002
	Li2	3f	0.009	0.008	0.008	0.001	0.004	0.0005	−0.0006
	F1	6g	0.008	0.008	0.009	0.009	0.005	0.0020	−0.0003
	F2	6g	0.008	0.008	0.008	0.008	0.004	−0.0001	0.0012
	F3	6g	0.008	0.008	0.008	0.008	0.004	−0.0014	−0.0002

[a]Space group *P321* and *P$\bar{3}$m1* symmetry constraints would imply for positions 1a and 2d: $U_{11} = U_{22} \neq U_{33}$, $U_{12} = \frac{1}{2}U_{11}$, $U_{13} = U_{23} = 0$; for positions 3e and 3f: $U_{13} = -U_{23}$.[30]

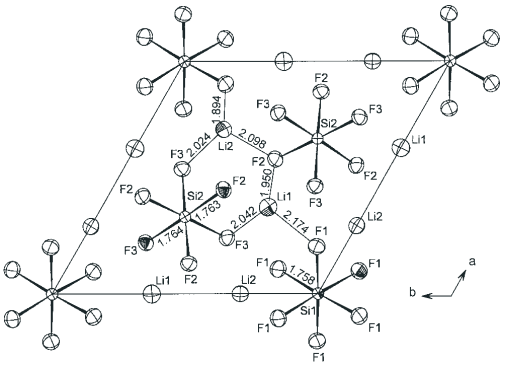

Figure 10. The Li_2SiF_6 structure from the MD simulation: Model B (space group: *P321;* No. 150). The *P321* space group symmetry operations (x, y, z; $-y, x - y, z$; $-x + y, -x, z$; $y, x, -z$; $x - y, -y, -z$; $-x, -x + y, -z$) were used to fold the entire MD simulation box back into an asymmetric unit (shaded atoms). Anisotropic displacement factors calculated from the MD data are plotted as ellipsoids (95% probability).

sites. This makes the 6g site-occupation 5/6 and the new 6h site-occupation 1/6. The folding of the MD box to produce an asymmetric unit and the calculation of ADFs for Model A therefore also includes the 6h site for Li1.

The original and the simulated structures are both listed in Table 7. The ADFs are given in Table 8. Both simulated crystal structures have reasonable coordinates and temperature factors, with ADF values for Model A somewhat larger than for Model B. The developed force field unambiguously rejected the original arrangement of Li1 atoms in Model A and supported the arrangement in Model B. Model B is preferred because the structure was stable throughout the simulation, the energy was lower, and the calculated ADFs in Table 8 are smaller. This suggests that the correct space group for Li_2SiF_6 is probably *P321;* Model B is shown in Figure 10.

References

1. Gadjourova, Z.; Mareo, D. M.; Andersen, K. H.; Andreev, Y. G.; Bruce, P. G. Chem Mater 2001, 13, 1282.
2. Staunton, E.; Christie, A. M.; Andreev, Y. G.; Bruce, P. G. Abstract 28, 12th International Meeting on Lithium Batteries, Nara, Japan, 27 June–2 July, 2004.
3. Borodin, O.; Smith, G. D.; Jaffe, R. L. J Comp Chem 2001, 22, 641.
4. Cipriani, C. R Soc Mineral Ital 1955, 11, 58.
5. Cox, B. J Chem Soc 1954, 3251.
6. Zalkin, A.; Forrester, J. D.; Templeton, D. H. Acta Crystallogr 1964, 17, 1408.
7. Frisch, M. J.; Trucks, G. W.; Schlegel, H. B.; Scuseria, G. E.; Robb, M. A.; Cheeseman, J. R.; Zakrzewski, V. G.; Montgomery, J. A., Jr.; Stratmann, R. E.; Burant, J. C.; Dapprich, S.; Millam, J. M.; Daniels, A. D.; Kuden, K. N.; Strain, M. C.; Farkas, O.; Tomas, J.; Barone, V.; Cossi, M.; Cammi, R.; Menucci, B.; Romelli, C.; Adamo, C.; Clifford, S.; Ochterski, J.; Petersson, G. A.; Ayala, P. Y.; Cui, Q.; Morokuma, K.; Salvador, P.; Dannenberg, J. J.; Malick, D. K.; Rabuck, A. D.; Raghavachari, K.; Foresman, J. B.; Cioslowski, J.; Ortiz, J. V.; Baboul, A. G.; Stefanov, B. B.; Liu, G.; Liashenko, A.; Piskorz, G.; Kormaromi, I.; Gomperts, R.; Martin, R. L.; Fox, D. J.; Keith, T.; Al-Laham, M. A.; Peng, C. Y.; Nanayakkara, A.; Challacombe, M.; Gill, P. M. W.; Johnson, B. G.; Chen, W.; Wong, M. W.; Andres, J. L.; Gonzalez, C.; Head–Gordon, M.; Replogle, E. S.; Pople, J. A. Gaussian 98 (Revision A.11); Gaussian Inc.: Pittsburgh, PA, USA, 2001.
8. Becke, A. D. Phys Rev A 1988, 38, 3098; Lee, C.; Yang, W.; Parr, R. G. Phys Rev B 1988, 37, 785.
9. Becke, A. D. J Chem Phys 1993, 98, 5648; Lee, C.; Yang, W.; Parr, R. G. Phys Rev B 1988, 37, 785.
10. Becke, A. D. J Chem Phys 1993, 98, 5648; Perdew, J. P.; Chevary, J. A.; Vosko, S. H.; Jackson, K. A.; Pederson, M. R.; Singh, D. J.; Fiolhais, C. Phys Rev B 1992, 46, 6671.
11. Dunning, T. H. J Chem Phys 1987, 98, 1007.
12. Krishman, R.; Binkley, J. S.; Seeger, R.; Pople, J. A. J Chem Phys 1980, 72, 650.
13. Dunning, T. H. J Chem Phys 1989, 90, 1007; Davidson, E. R. Chem Phys Lett 1996, 220, 514.
14. Smith, G. D.; Jaffe, R. L.; Patridge, H. J Phys Chem A 1997, 101, 1705.
15. Breneman, C. M.; Wiberg, K. B. J Comp Chem 1990, 11, 361.
16. Gerdy, J. J. PhD Thesis: Accurate Interatomic Potentials for Simulations, CalTech 1995, www.wag.caltech.edu/publications/theses/ ,downloaded: Sept 2003.
17. Gordon, M. S.; Carroll, M. T. J Phys Chem 1990, 94, 8125.
18. Rappe, A. K. J Am Chem Soc 1992, 114, 10035.
19. Shannon, R. D. J Appl Phys 1993, 73, 348.
20. Gambi, R.; Cappelletti, D.; Liuti, G.; Pirani, F. J Chem Phys 2003, 95, 1852.
21. Brown, D.; Neyertz, S. Mol Phys 1995, 84, 577.
22. Born, M. Z Physik 1932, 75, 1.
23. Averdunk, F.; Hoppe, R. Zeitschr Anorg Allgem Chem 1990, 582, 111.
24. Hoppe, W.; Liebe, W.; Daehne, W. Zeitschr Anorg Allgem Chem 1961, 307, 276.
25. Ed. Hahn, T. International Tables for Crystallography, Vol. A, Space-Group Symmetry; Dordrecht: Kluwer, 1996.
26. Schaefer, G. F. Z Kristallogr 1986, 175, 269.
27. Hoover, W. G. Phys Rev A 1985, 31, 1695.
28. DL_POLY is a package of molecular simulation routines written by W. Smith and T. R. Forester; copyright: The Council for the Central Laboratory of the Research Councils, Daresbury Laboratory at Daresbury, Warrington UK, 1996.
29. Grosse–Kunstleve, R. W.; Adams, P. D. J Appl Crystallogr 2002, 35, 477.
30. Ed. Ibers, J. A.; Hamilton, W. C. International Tables for X-ray Crystallography; Dordrecht: Kluwer, 1974, vol. iv.

Paper II

Molecular dynamics simulation of the crystalline short-chain polymer system $LiPF_6{\cdot}PEO_6$ ($M_w \sim 1000$)

D. Brandell,[a] A. Liivat,[a] A. Aabloo[b] and J. O. Thomas*[a]

Received 12th April 2005, Accepted 1st August 2005
First published as an Advance Article on the web 26th August 2005
DOI: 10.1039/b505091j

In an effort to probe the effect of chain length on the structure and properties of ionically conducting polymer electrolytes, the crystalline system $LiPF_6{\cdot}PEO_6$ has been simulated at 293 K using the Molecular Dynamics Simulation (MDS) technique. The specific system studied is short-chain poly(ethylene oxide) with the formulation CH_3–$(OCH_2CH_2)_{22}$–OCH_3; $M_w = 1015$, a commercially available mono-disperse short-chain PEO form resembling that studied experimentally (Stoeva *et al.*, *J. Am. Chem. Soc.*, 2003, **125**, 4619, ref. 27). The methoxy chain-ends have been arranged to reproduce smectic and nematic models. Calculated Li^+ ion coordination, polymer chain configuration, chain-end registry and diffraction profiles are compared both with experiment and with the results from earlier MD simulations of infinite PEO chain systems (Brandell *et al.*, *J. Mater. Chem.*, 2005, **15**, 1422, ref. 30). The differences found are interpreted in the terms of chain-end effects and polymer relaxation.

1 Introduction

Polymer electrolytes are complexes of salts, *e.g.*, NH_4SCN, $NaCF_3SO_3$, $LiN(SO_3CF_3)_2$, *etc.*, dissolved in a polymer matrix.[1,2] Since their discovery, the archetypal polymer host for these materials has been poly(ethylene oxide) (PEO), $–(CH_2CH_2O)_n–$.[3,4] These materials continue to hold interest since their mechanical properties recommend them for application in all-solid-state batteries.[5] Their ion conductivity has long been ascribed to their amorphous forms.[6] It is found, however, that such polymer electrolytes have poor ionic conductivities; around 10^{-5} S cm^{-1} under ambient conditions. Much research has therefore focused on trying to increase the amorphous content of these materials through different types of salt or polymer modification[7,8] or the use of polymer additives.[9]

It has been suggested more recently, however, that a possible route to improve ion conductivity in these systems is to focus instead on certain crystalline polymer electrolytes,[10] since these have been found to retain a high degree of local order in their amorphous phase.[11] The last decade has seen the structure determination of many salt–PEO complexes; the structures for systems with cation : EO ratios of 1 : 1, 1 : 3, 1 : 4, 1 : 6 and 1 : 8 are now known.[12–26] In this context, the $LiXF_6{\cdot}PEO_6$ (X = P, As or Sb) system has been thoroughly investigated,[27] since ion conduction in these crystalline phases has been found to be somewhat higher than in their amorphous counterparts.[28] This feature has been ascribed to the specific structure of the materials. It has been shown from diffraction studies that the PEO here forms hemi-helices (half-cylinders) which pairwise create channels for the Li^+-ions. The anions and cations are thereby structurally separated; a situation which can well promote ion mobility. The Li^+ ions each coordinate to five oxygen atoms, three belonging to the one PEO chain and two to the other.[21,22] The room temperature conductivity is *ca.* 10^{-8} S cm^{-1} in these complexes, and has been shown to increase by 1–2 orders of magnitude on isovalent doping with $\sim$5 mol% $N(SO_2CF_3)_2^-$ (TFSI) to replace AsF_6^-.[29]

In an earlier study,[30] we have simulated the structure of $LiPF_6{\cdot}PEO_6$ using Molecular Dynamics (MD) techniques. Apart from an increase in the Li^+–O_{et} coordination number from 5 to 6 and some changes occurring in the polymer dihedral angles, the double hemi-helical structure and ion-separation has been generally retained. As in the structural model determined from powder diffraction, the PEO-chain model used in these simulations was approximated to be infinite, and therefore lacking in end-groups. However, most of the experimental structure work, and especially the conductivity studies, have been performed using fairly short methoxy end-capped polymer chains, typically with M_w in the range 1000–2000. In these materials, a high concentration of end-group "defects" exists whose influence on both the structural and dynamical phenomena is hitherto quite unknown. Particularly, the structural arrangement of the end-groups has never been addressed previously.

In this present study, we therefore focus on how methoxy end-groups can influence the structure of $LiPF_6{\cdot}PEO_6$. We have chosen to work with a short-chain PEO of molecular weight 1015 ($n = 22$), since this is a commercially available mono-disperse system closely resembling that used in earlier experimental studies.[27] We have also chosen to simulate models which represent two types of chain-end arrangement, corresponding to *nematic* and *smectic* forms (see Fig. 1; also Fig. 10 in ref. 30).

2 The MD simulations

In MD simulations, the atomic motion in a chemical system is modelled in terms of classical mechanics by solving Newton's

[a]*Department of Materials Chemistry, Ångström Laboratory, Uppsala University, Box 538, SE-751 21 Uppsala, Sweden. E-mail: josh.thomas@mkem.uu.se*
[b]*Institute of Technology, Tartu University, Tähe 4, 51010 Tartu, Estonia*

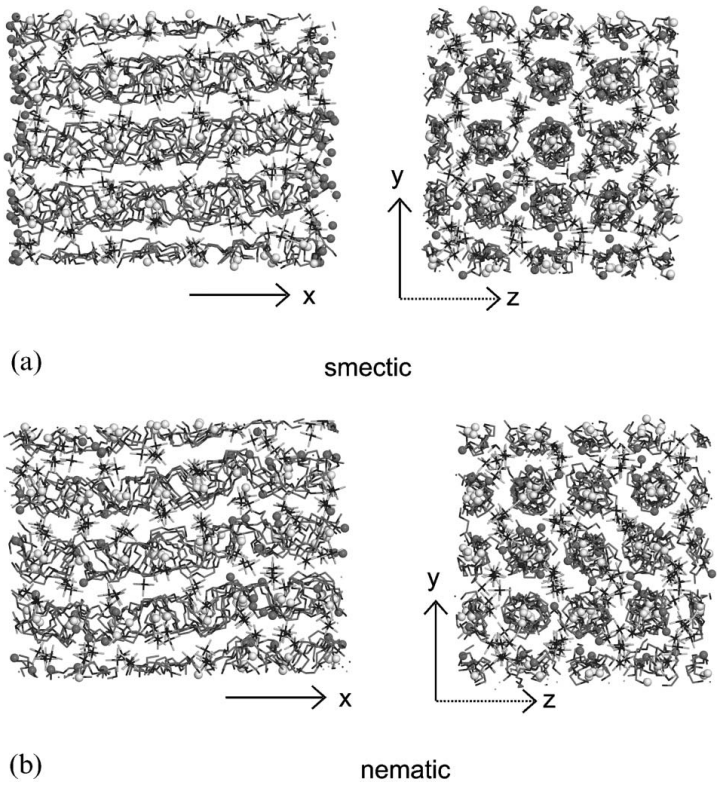

Fig. 1 The final MD-box for crystalline (a) smectic and (b) nematic $LiPF_6{\cdot}PEO_{5.75}$ (M_w = 1015 for "PEO"); Li^+ are white, P are black, F are light grey, O are dark grey, C are grey; end-group carbons and Li^+ are spheres and hydrogen atoms are omitted.

equations of motion simultaneously for each particle in an appropriately chosen periodic simulation box. The resulting atomic trajectories reflect implicitly the assumed description of the forces acting between the particles.

The intramolecular potentials for PEO describing bond vibrations and torsional motion in the polymer chain have here been taken from Neyertz *et al.*[31] This set of potentials was developed originally by Gejji *et al.*[32] from MP2/6-311++G**// HF/3-21G energy minimisation of the diglyme system and was validated for crystalline PEO,[31] $NaI{\cdot}PEO_3$[33] and for various amorphous polymer electrolytes.[34–40] The intermolecular potentials are described by Buckingham or Lennard-Jones electrostatic interactions:

$$U(r) = A\exp\left(-\frac{r}{B}\right) - \frac{C}{r^6} - \frac{D}{r^4} + \frac{q_1 q_2}{4\pi\varepsilon_0 r} \qquad \text{(Buckingham)}$$

$$U(r) = \frac{A}{r^{12}} - \frac{C}{r^6} + \frac{q_1 q_2}{4\pi\varepsilon_0 r} \qquad \text{(Lennard - Jones)}$$

A, *B*, *C* and *D* are here constants depending on the interacting atom types. The values of the constants for different interactions within the PEO were taken from Neyertz *et al.*,[33] while the intermolecular potentials involving $LiPF_6$ has been developed by Borodin *et al.*[41–43] These potentials take into account the polarisation contribution to the total energy, and have been scaled for use in condensed phase systems. The potentials for the methoxy end-groups were taken from the work of Borodin and Smith[44] using the model of Müller-Plathe.[45]

The MD simulations use periodic boundary conditions and an Ewald summation routine to treat the long-range electrostatic forces. The short-range cut-off used is 16 Å and the Verlet sphere used in the construction of the Verlet neighbour-list has a 0.5 Å radius. A NVT Nose-Hoover thermostat has been used consistently, since "fixed volume" is appropriate for comparison with crystallographic results. A multiple time-step technique was used, with a longer time-step of 0.5 fs for longer distances and a shorter time-step of 0.1 fs inside a sphere of radius 6 Å. The simulations were performed for a temperature of 293 K. The polymer MD simulation program used is DL_POLY.[46]

The start structures in the MD simulation boxes contained 4 × 2 × 4 unit cells of crystalline $LiPF_6{\cdot}PEO_6$ with dimensions a = 46.928 Å, b = 34.750 Å, c = 34.768 Å, β = 107.8°, involving 32 PEO hemi-helices of CH_3–$(OCH_2CH_2)_{22}$–OCH_3, along with 128 $LiPF_6$ units. The start structures used were

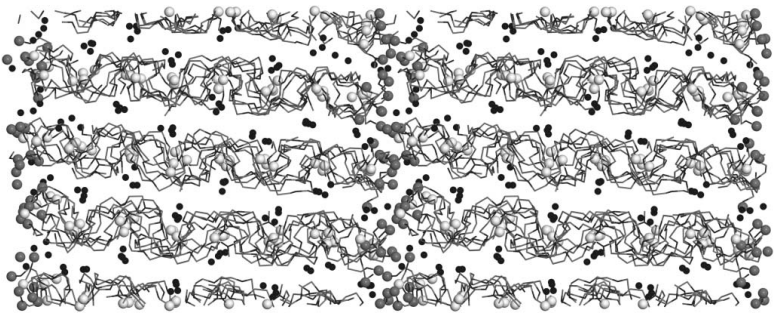

Fig. 2 A snapshot of the MD-box at the end of the simulation (doubled in the *x*-direction) for the smectic model of $LiPF_6{\cdot}PEO_{5.75}$ (M_w = 1015 for "PEO"); Atom shading as in Fig. 1; H and F are omitted for clarity.

created from the asymmetric unit resulting from the neutron diffraction study,[22] with no internal symmetry conditions imposed within the periodic simulation box. The end-groups were created by removing one EO unit from each chain and adding hydrogen atoms to maintain sp^3-hybridisation on the carbon atoms. The removal of ether oxygen atoms in this way resulted in an effective formula $LiPF_6{\cdot}PEO_{5.75}$ and a lowering of the density by 2.5%. This was felt to be an optimal compromise, since the model provides space for the end-groups to redistribute. A model with the exact formulation $LiPF_6{\cdot}PEO_6$ would result in structural anomalies in the hemi-helical cylinders; some of the hemi-helical polymer pairs and anion columns would contain spurious ion vacancies.

In the *smectic* model, all end-groups were initially situated in a plane perpendicular to the polymer-chain direction. In the *nematic* arrangement, one of each pair of hemi-helices in the smectic model were shifted by one crystallographic asymmetric unit (6 EO-units) in the positive or negative helical direction with respect to its hemi-helical partner, thus creating a system without chain-end pairs. The structures were each simulated for 1 ns, *i.e.*, 2×10^6 time-steps. The result structures appeared stable. The final 250 ps of these simulations were sampled to derive structural and dynamical properties.

3 Results and discussion

3.1 "Macroscopic" structure and dynamics

The total equilibrium energy is closely similar in the *nematic* and *smectic* models, indicating that both phases could coexist in the real material. The final snapshots for these two systems can be seen in Fig. 1. It is clear that the cylindrical structure of the PEO hemi-helices is retained in both simulations, and that almost all the lithium ions remain inside these "cylinders". It is striking how the anions approach the hemi-helices during the simulation; a phenomenon that was never observed for the infinite PEO-chain model.[30] This becomes a critical factor in our later discussion of ion-transport mechanisms.

It can also be noted from Fig. 1 (but is perhaps even more evident in Fig. 2, where the MD box is shown doubled along the *x*-direction) that the helical axes in the *smectic* model do not lie along the *x*-direction but undergo a tilt, corresponding to a lateral displacement of 4.9 Å approximately in the *y*-direction, which breaks the continuity of the short-chains across the space between the smectic layers. The lithium ions are thus less able to diffuse from helix to helix, and the anions cannot move from channel to channel. This clearly imposes a significant limitation on the conduction mechanism. The *nematic* model exhibits a somewhat different behaviour: the PEO cylinders are now forced to follow a common infinite polymer-chain axis, but each cylinder has a small kink (Fig. 3), giving the cylindrical structure a wave-like form. These kinks occur close to regions of PEO chain-breaking; either within the chain itself or in adjacent chains. The structural effect of such a kink extends up to 10 Å from the kink itself. These structural features clearly imply that ion mobility in a short-chain system differs from that in an infinite-chain system, since the lithium channels within the helices and the anionic columns between the helices become discontinuous and thus seriously obstructed.

Although the density is somewhat lower ($\sim$2.5%) in the short-chain system compared to the infinite system, the helices do not appear to expand much into the space created by the removal of PEO units and the addition of end-groups. The average C–C end-to-end distance increases from 44.55 Å in the start configuration to 45.05 Å in the *smectic* model, indicating some movement of the methoxy end-groups into the surface layer formed. In the *nematic* model, however, this average end-to-end distance is found to *decrease* to 43.97 Å. In both cases, the small variation in end-to-end distance gives evidence of negligible chain-end entanglement.

The chain-ends clearly also display more dynamical behaviour than the rest of the polymer, which can be seen from the mean-square-displacement (MSD) plots for the carbon atoms (Fig. 4). The diffusion coefficient (D) for the

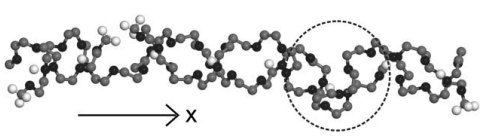

Fig. 3 A polymer double hemi-helix containing 8 Li^+ ions in the nematic model of $LiPF_6{\cdot}PEO_{5.75}$ (M_w = 1015 for "PEO"), showing (circled) a kink in the polymer channel.

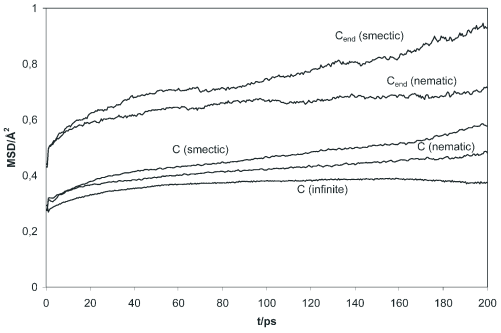

Fig. 4 Mean-square-displacement (MSD) functions for carbon atoms in crystalline $LiPF_6{\cdot}PEO_{5.75}$ (smectic and nematic models) and $LiPF_6{\cdot}PEO_6$ (infinite PEO chain).

Table 1 MD-derived local diffusion coefficients for different atom-types in short-chain $LiPF_6{\cdot}PEO_{5.75}$ ("PEO" M_w: 1015). Values in 10^{-12} m^2 s^{-1}

Atom type	Smectic model	Nematic model
C	1.9	1.2
$C_{end\text{-}group}$	3.0	2.7
H	2.3	1.3
$H_{end\text{-}group}$	3.0	2.4
O	0.9	0.8
Li	0.8	0.9
P	1.3	1.0
F	7.1	6.3

different atom types can be calculated from the slope of the MSD plots on the basis of: $D = \frac{1}{6Nt}\sum_{i=1}^{N}\left(\langle x_i^2\rangle + \langle y_i^2\rangle + \langle z_i^2\rangle\right)$

The values of the resulting diffusion coefficients are listed in Table 1. We see that the local diffusion of the end-group carbons is larger than for other backbone atoms; the end-groups in the smectic model are also more mobile. This is presumably a surface phenomenon—there is more space in the interface regions between the liquid-crystal layers of the smectic model, allowing the chain-ends to move around more freely.

Not surprisingly, it can also be seen in Fig. 4 that the short chains can diffuse more freely than infinite chains. This is observed for all atom types in the short chains, suggesting an overall higher mobility. Higher chain mobility is an indication of greater chain relaxation and more liquid-like behaviour in the low molecular-weight systems. On the other hand, we should note that there is negligible net transport of material in these systems. The MSDs for Li^+, P and O_{et} (not shown) imply the same local diffusion (see Table 1). The larger values of the diffusion coefficient (D) for the fluorine atoms are not related to actual "diffusion", but rather to PF_6^- rotation; *cf.*, Fig. 9 in ref. 30.

3.2 Chain-end conformations

The mobile chain-ends exhibit a broad variety of local conformations which are difficult to characterise systematically. In Fig. 5, the positions of the end-group carbons are

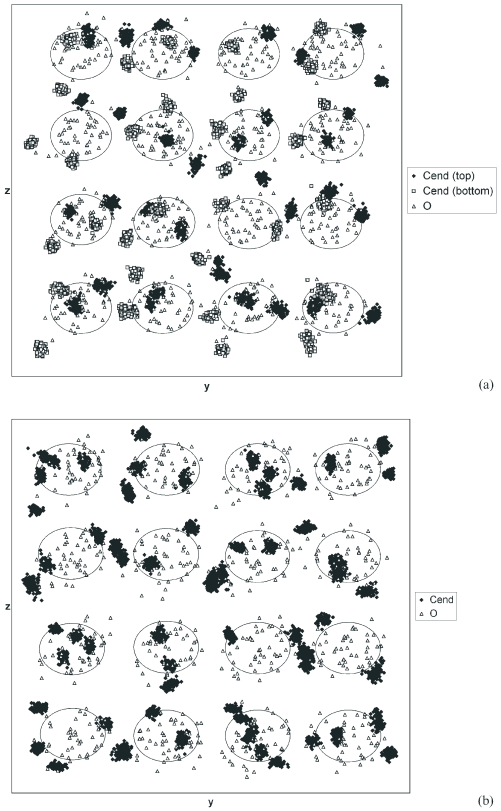

Fig. 5 Projections of the methoxy end-groups onto the *yz*-plane for the last 100 sampling points of the MD simulation of (a) smectic $LiPF_6{\cdot}PEO_{5.75}$ and (b) nematic $LiPF_6{\cdot}PEO_{5.75}$. Ether oxygen atoms from the last snapshot have also been included for clarity; ellipsoids representing the extent of the polymer double hemi-helices are also drawn.

shown on the *yz*-plane for the last 100 sampling points for both the nematic and smectic models. It is evident that the distribution of chain-ends lies closer to the helical axis in the nematic model, although no effective space-group is apparent. This is consistent with the lower dynamics of the nematic model system. End-group displacements are larger in the smectic system (also in the *x*-direction), as evidenced by the larger average end-to-end distance (45.05 Å compared to 43.97 Å).

Fig. 5 also provides information on the linkage and registry between chain end-groups. In several cases, terminal methyl groups on two adjacent short-chains within the same double-hemi helix (a situation which can only occur in the smectic model) tend to approach one another. The effective average distance between these neighbouring groups decreases somewhat during the simulation (from 5.02 to 4.80 Å), despite the fact that some of these distances actually become much greater due to chain-end migration. The situation is controlled by

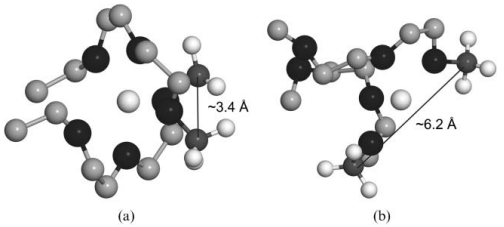

Fig. 6 Two types of local environments at the ends of the hemihelices in the smectic model of $LiPF_6{\cdot}PEO_{5.75}$: (a) end-groups close to one another, (b) end-groups distant from one another.

Li^+ ions close to the ends of the helices; when a Li^+ ion remains close to, yet within, the end of a helix, the methoxy groups tend to wrap themselves around it, resulting in short distances between the methyl groups (Fig. 6a). When a Li^+ ion either leaves a helix and migrates into the space between the smectic layers, or drifts in towards the centre of the helix, the chain-end pairs drift apart (Fig. 6b).

Another aspect of chain-end registry relates to neighbouring ends on different sides of a chain break, especially across the space between the smectic layers. This distance increases from an average value of 4.8 Å at the start of the simulation to 6.2 Å at equilibrium. This is partly a result of a shift of the entire helix in the *yz*-plane, and can be ascribed to the weak repulsive forces acting between the methyl groups. The corresponding average distance increases to 4.9 Å in the nematic model. Another factor to consider in this connection, however, is the possibility that the true *a*-axis can actually be shorter in the mono- compared to the polydisperse system from which our cell parameters are taken.

Surprisingly, it is found that the librational/rotational dynamics of the terminal methoxy groups is not significantly greater than that throughout the rest of the polymer: segmental motion has a characteristic time-scale of the order of 10^{-10} s; a figure which corresponds well with calculated and experimental values in amorphous systems.[47] On the other hand, the CH_3 methyl groups themselves indeed undergo more frequent reorientations (hindered rotations), with the methyl hydrogen atoms interchanging position at an average rate of *ca.* 1.4×10^{11} s^{-1} in the smectic, and *ca.* 1.2×10^{11} s^{-1} in the nematic system. This comparatively slow reorientation of the methoxy groups can nonetheless serve to promote ionic conductivity in the system, especially in the interlayer space of the smectic system. These phenomena can be better investigated for a system with higher ion mobility, *e.g.*, by imposing an external electric field on the MD simulation box.

3.3 Coordination

The coordination number (CNF) functions and radial distribution (RDF) functions for Li–Li, Li–O and Li–P are plotted in Fig. 7 for the smectic, nematic and infinite-chain models. The immediate impression is that the smectic and nematic models resemble one another more than they do the infinite-chain model; and also that the associated RDF peaks

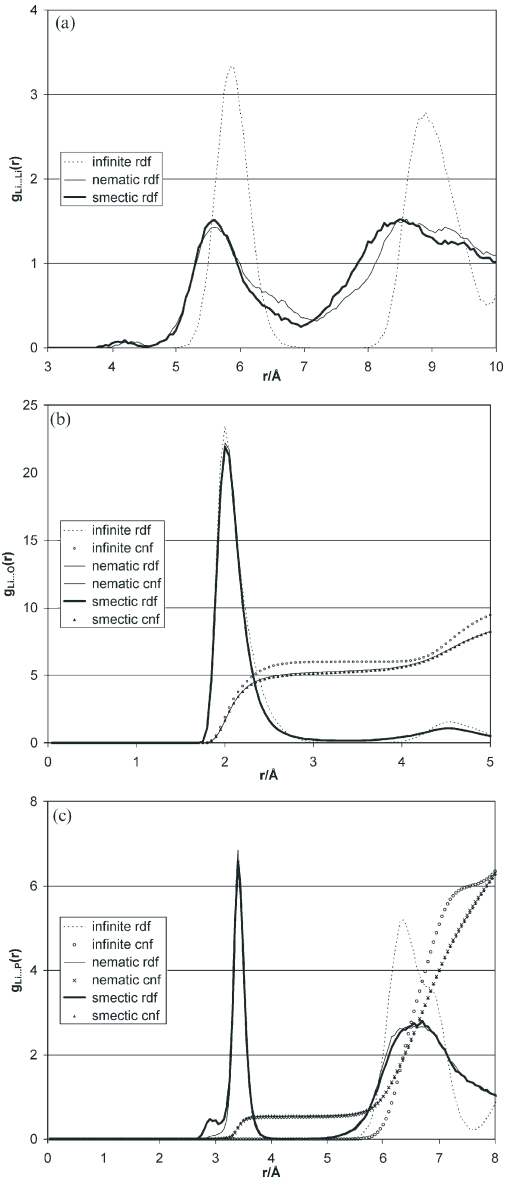

Fig. 7 Radial distribution (rdf) and coordination number (cnf) function for: (a) Li–Li, (b) Li–O_{et} and (c) Li–P in crystalline $LiPF_6{\cdot}PEO_{5.75}$ (smectic and nematic models) and $LiPF_6{\cdot}PEO_6$ (infinite PEO model). Note that curves for the smectic and nematic systems almost totally overlap in (b) and (c).

are much broader in both short-chain systems. This liquid-like peak broadening indicates greater structural relaxation in the short chains, where the Li–Li distances are also found to decrease to an average value of 5.6 Å compared to 5.9 Å in the

infinite-chain system. Even shorter Li–Li distances (as short as *ca.* 4.3 Å) are also detected in both short-chain systems. This behaviour is best ascribed to the (short) finite length of the polymer chains, which reduces the number of available coordination sites for Li^+ ions: the Li^+–O_{et} coordination number in the short-chain system is 5 compared to 6 for the infinite-chain system. This is also reflected in CN (O_{et}–Li^+) values: *ca.* 0.8 at 3 Å for short chains, compared to 1.0 at the same distance in the infinite-chain system—an unexpected and significant result considering the higher Li concentration in the short-chain systems. The lower CN (Li^+–O_{et}) value is consistent with the neutron diffraction determined structure,[22] but is compensated for in the short-chain systems by the presence of Li^+–PF_6^- contact pairs (Fig. 7c). The CN (Li–P) value is *ca.* 0.5 at 4.0–5.0 Å in short-chain systems, implying that half the Li^+ ions form ion-pairs or -clusters with the PF_6^- anions; the Li–P distance is *ca.* 3.4 Å. This is clearly different from the infinite-chain system and from the experimentally determined structure, where the Li–P separation is >6 Å.[22]

A small but perhaps significant difference appears between the smectic and nematic models in the form of a small peak in the Li–P RDF plot at 3 Å for the smectic system (Fig. 7c). This is found to correspond to extra Li^+–PF_6^- pairing (in both C_{2v} and C_{3v} configurations) near the surface of our mono-disperse smectic layers.

3.4 PEO backbone structure

The experimental sequence of dihedral angles along the asymmetric unit was *tggttgctgttgggctc*,[22] while our MD-derived sequence is *ttctgcgtcttcgctc* (NPT simulation) and *ttctgggtgttctggtc* (NVT simulation) for the infinite PEO model (where dihedral angles in the range 0 ± 45° are defined as *cis* (*c*), 180 ± 45° as *trans* (*t*), and the remainder as either *gauche* (*g*) or *anti-gauche* ($\bar{g}$)).[30] That this same sequence length of 6 EO units was found both from MD and from the diffraction studies is strong confirmation of the validity of the experimental crystallographic space group ($P2_1/a$). In *both* short-chain models, however, no such repeat unit is found. Each dihedral angle is relatively stable, implying that the *t*/*g*/$\bar{g}$ sequence is generally retained, although occasional shifts in some backbone units appear. Fig. 8 displays the mean distribution of dihedral angles over all 66 polymer backbones in the MD box (from methyl group to methyl group) in both short-chain systems. It is clear that the CCOC and COCC dihedral angles are generally *t*, while they are either *g* or $\bar{g}$ for the OCCO dihedral angles. This so-called "gauche effect"[48,49] for the OCCO dihedral angles is found in many crystalline and amorphous polymer systems, and is indeed implicit in the form of our backbone force-field model.[32] The OCCO double peaks in Fig. 8 are an effect of the method of summation, rather than of any dynamical effects in the individual angles.

An interesting feature is that some OCCO dihedral-angle sequences show alternating behaviour, switching between *g* and $\bar{g}$ every second EO-unit for as many as 10 EO-units. This type of situation is found for sequences degree of uncoordinated O_{et}'s, where the chain can more easily adopt its most energetically favourable conformation; see Fig. 9.

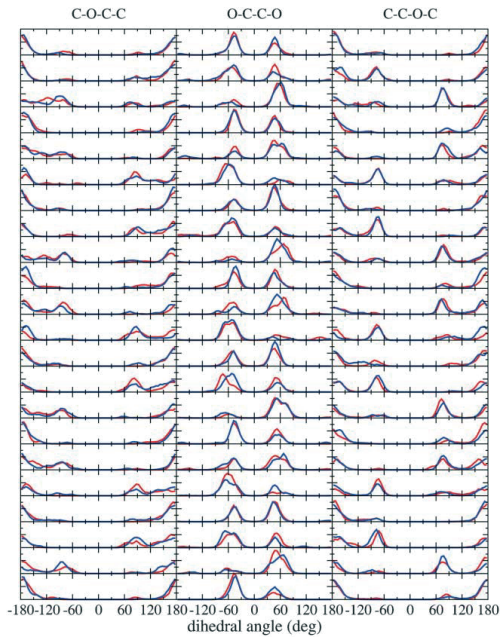

Fig. 8 Distribution of dihedral angles for PEO in $LiPF_6$·$PEO_{5.75}$ ("PEO" M_w = 1015) at 293 K. The boxes show sequentially (from top left to bottom right) each individual dihedral angle from the first methyl carbon to the last, summed over all 32 polymer chains. Smectic model in red; nematic in blue.

3.5 Simulated diffraction profile

The variations in structure between the different polymer helices in the MD box make it impossible to identify any periodic sub-unit within the box, *i.e.*, no effective crystallographic asymmetric unit can be found. However, a significant level of periodicity nevertheless exists in the structure; the helices are arranged in a regular array, and non-randomicity certainly exists in the distribution of the Li^+ ions. This justifies a closer comparison between the MD- and experimentally-derived structures.

An effective diffraction pattern has been calculated by accumulating the scattering contributions from 500 MD-generated "snapshots" of the positions of the 6240 atoms in the MD box. This is done using the program DISCUS[50] for

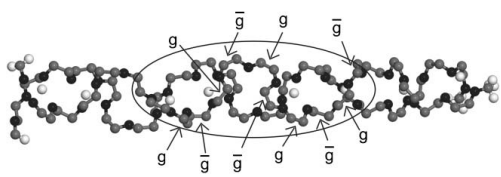

Fig. 9 A polymer double hemi-helix in the smectic model of $LiPF_6$·$PEO_{5.75}$ showing an extended sequence of OCCO dihedral angles which alternate between *g* and $\bar{g}$.

the two short-chain and the infinite-chain models. The results are compared with the experimental diffractogram in Fig. 10. It must be remembered that no symmetry constraints are applied to the system during this calculation—the program treats the entire MD box as a primitive unit-cell. A minor problem with this comparison is that the simulated structure is modelled using cell parameters taken from a neutron diffraction study of a *deuterated* system; hence the small shifts in some of the peak positions.

The immediate impression is that the *infinite* MD structure reproduces the experimental diffractogram quite well; the four main peaks found in the diffractograms have reasonably similar intensities, although the peak at $2\theta = 21.9^\circ$ is clearly split into at least two peaks ($21\bar{1}/230/23\bar{1}$) as a direct result of the different cell parameters used. The calculated profiles for the smectic and nematic short-chain structures (which have the same M_w as the experimental material) agree less well with experiment, although the two strongest experimental peaks (at $2\theta = 14.4^\circ$ and 21.9°) are also dominant in the calculated diffractograms; the slightly weaker experimental peaks at $2\theta = 16.5^\circ$ and 22.8° also appear from the MD simulation. Most disappointing, however, is the striking incidence of spurious noise peaks in the calculated short-chain model profiles. Clearly, the size of our MD box is inadequate to reproduce crystallographic periodicity in a polymeric material of this type involving such a rich variety of conformations. A significantly larger box and much longer simulation times are needed to represent the true long-range periodicity in the structure. In spite of this (and disregarding the noise level), the *relative* intensities for the four main peaks in the experimental diffractogram are well reproduced for the *smectic* model. This can be taken as strong evidence that our smectic model comes closest in representing the real short-chain material. Interestingly, the effective thermal motion correction built into the DISCUS calculation of the X-ray diffractogram (summation over 6240 sets of coordinates and 500 snapshots) would appear to give a reasonable description of thermal motion; see Fig. 10.

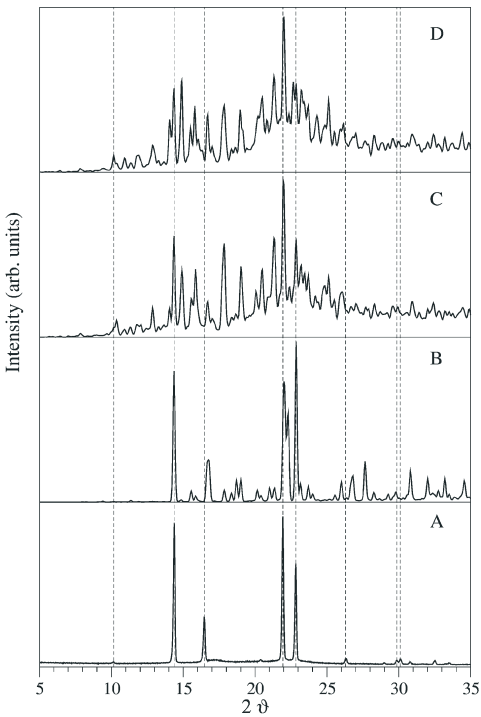

Fig. 10 Experimental (A) and calculated X-ray diffractograms for infinite PEO chain (B), smectic (C) and nematic (D) models of $LiPF_6{\cdot}PEO_6$. The major experimental peaks are indicated by vertical lines. *Note*: the small discrepancies in peak positions (most noticeable for the $21\bar{1}$ reflection at $2\theta = 16.5^\circ$) result from using cell parameters taken from a neutron diffraction study of a deuterated sample.

Table 2 MD-derived isotropic thermal displacement parameters (U_{iso} in Å^2) for different atom-types in the smectic and nematic models of $LiPF_6{\cdot}PEO_{5.75}$ (''PEO'' M_w: 1015) and in an infinite-chain $LiPF_6{\cdot}PEO_6$ system[a]

Atom type	Smectic model	Nematic model	Infinite PEO
Li	0.051	0.047	0.037
P	0.061	0.061	0.051
F	0.519	0.552	0.127
C	0.076	0.070	0.076
O	0.060	0.057	0.050

[a] Experimental temperature factors (B) were fixed in the refinements[22] to unrealistically low overall values; no meaningful comparison is therefore possible.

The short-chain MD data has also been used to derive the isotropic thermal displacement factors (U_{iso}) for the different systems; see Table 2. Since the MD box contains no internal symmetry operations, the mean-square-displacements, σ_α^2, must first be calculated for each individual atom in the box by summing over N time-steps using $\sigma_\alpha^2 = \frac{1}{N}\sum_{k=1}^{N} \langle r_{\alpha,k} - \bar{r}_\alpha \rangle^2$ for $\alpha = x, y, z$ for atom k; resulting in $U_{iso} = \frac{1}{3}\left(\sigma_x^2 + \sigma_y^2 + \sigma_z^2\right)$. The overall thermal displacement parameters can then be estimated from the average U_{iso} for each atom-type. A comparison with the calculated thermal displacement parameters for the infinite-chain system (included in Table 2) shows a reasonable correspondence. Notably, the thermal parameters in the smectic and nematic systems are essentially identical, and systematically larger than for the infinite system. Moreover, the MD simulation indicates significantly higher thermal motion in the F-atoms in the short-chain compared to the infinite-chain systems. This clearly reflects the higher rotational freedom in the short-chain system. In our MD simulation of the infinite-chain system, rotation was hindered around the x-axis of the PF_6^- anion (parallel to the axis of the hemi-helices; see Fig. 9 in 30) – this effect disappears in the short-chain systems, where the chain-backbone is more able to relax.

4 Summary

It is interesting to note that the infinite polymer chain model gives good agreement with experiment. This is presumably because the ''infinite-chain''-like regions of the finite-chain

systems are those which actually contribute to the diffraction data; scattering from chain-end defect regions goes into the background, rendering these regions effectively unobservable. Of the two short-chain models, the *smectic* model seems to give the better fit. Importantly, our MD treatment is successful in distinguishing dynamics in a short-chain system from that in an infinite-chain system. This gives some indication as to how we should proceed in our efforts to probe this complex system further. In on-going work, we are trying to acquire a more definitive picture of how local structure and polymer relaxation influences ion dynamics. This we are doing by studying the effect of an imposed electric field on ion mobility in the same short-chain systems as we have studied here.

Acknowledgements

This work has been supported by grants from The Swedish Research Council (VR). The excellent service provided by The Center for Parallel Computers (PDC) at KTH, Stockholm is also gratefully acknowledged, as is a stipend for AL from The Archimedes Foundation (No. T.05-04/08), and a number of useful discussions with Dr David Brown, Université de Savoie, Campus Scientifique, Savoie Technolac, France.

References

1 F. M. Gray, *Polymer Electrolytes*, The Royal Society of Chemistry, Cambridge, 1997.
2 P. G. Bruce, *Solid State Electrochemistry*, Cambridge University Press, Cambridge, 1995.
3 D. E. Fenton, J. M. Parker and P. V. Wright, *Polymer*, 1973, **14**, 589.
4 J. M. Tarascon and M. Armand, *Nature*, 2001, **414**, 359.
5 M. Winter, J. O. Besenhard, M. E. Spahar and P. Novák, *Adv. Mater.*, 1998, **10**, 725.
6 C. Berthier, W. Gorecki, M. Minier, M. B. Armand, J. M. Chabagno and P. Rigaud, *Solid State Ionics*, 1983, **11**, 91.
7 M. A. S. A. Samir, F. Alloin, J.-Y. Sanchez and A. Dufresne, *Macromolecules*, 2004, **37**, 4839.
8 L. Ding, *Polymer*, 1997, **38**, 4267.
9 D. Golodnitsky, G. Ardel and E. Peled, *Solid State Ionics*, 2002, **147**, 141.
10 Y. Andreev and P. G. Bruce, *Electrochim. Acta*, 2000, **45**, 1417.
11 R. Frech, S. Chintapalli, P. G. Bruce and C. A. Vincent, *Chem. Commun.*, 1997, 157.
12 Y. Chatani and S. Okamura, *Polymer*, 1987, **28**, 1815.
13 Y. Chatani, Y. Fujii, T. Takayanagi and A. Honma, *Polymer*, 1990, **31**, 2238.
14 P. Lightfoot, M. A. Mehta and P. G. Bruce, *J. Mater. Chem.*, 1992, **2**, 379.
15 P. Lightfoot, M. A. Mehta and P. G. Bruce, *Science*, 1993, **262**, 883.
16 P. Lightfoot, J. L. Nowinski and P. G. Bruce, *J. Am. Chem. Soc.*, 1994, **116**, 7469.
17 J. B. Thomson, P. Lightfoot and P. G. Bruce, *Solid State Ionics*, 1996, **85**, 203.
18 Y. G. Andreev, P. Lightfoot and P. G. Bruce, *J. Appl. Cryst.*, 1997, **30**, 294.
19 Y. G. Andreev, G. S. MacGlashan and P. G. Bruce, *Phys. Rev. B*, 1997, **55**, 12011.
20 G. S. MacGlashan, Y. G. Andreev and P. G. Bruce, *J. Chem. Soc., Dalton Trans.*, 1998, 1073.
21 G. S. MacGlashan, Y. G. Andreev and P. G. Bruce, *Nature*, 1999, **398**, 792.
22 Z. Gadjourova, D. Matrín y Marero, K. H. Andersen, Y. G. Andreev and P. G. Bruce, *Chem. Mater.*, 2001, **13**, 1282.
23 I. Martin-Litas, Y. G. Andreev and P. G. Bruce, *Chem. Mater.*, 2002, **14**, 2166.
24 E. Staunton, A. M. Christie, Y. G. Andreev, A. M. Z. Slawin and P. G. Bruce, *Chem. Commun.*, 2004, 148.
25 E. Staunton, A. M. Christie, I. Martin-Litas, Y. G. Andreev, A. M. Z. Slawin and P. G. Bruce, *Angew. Chem., Int. Ed.*, 2004, **48**, 2103.
26 Y. G. Andreev, V. Seneviratne, M. Khan, W. A. Henderson, R. E. Frech and P. G. Bruce, *Chem. Mater.*, 2005, **17**, 767.
27 Z. Stoeva, I. Martin-Litas, E. Staunton, Y. G. Andreev and P. G. Bruce, *J. Am. Chem. Soc.*, 2003, **125**, 4619.
28 Z. Gadjourova, Y. G. Andreev, D. P. Tunstall and P. G. Bruce, *Nature*, 2001, **412**, 520.
29 A. M. Christie, S. J. Lilley, E. Staunton, Y. G. Andreev and P. G. Bruce, *Nature*, 2005, **433**, 50.
30 D. Brandell, A. Liivat, H. Kasemägi, A. Aabloo and J. O. Thomas, *J. Mater. Chem.*, 2005, **15**, 1422.
31 S. Neyertz, D. Brown and J. O. Thomas, *J. Chem. Phys.*, 1994, **101**, 10064.
32 S. P. Gejji, J. Tegenfeldt and J. Lindgren, *Chem. Phys. Lett.*, 1994, **226**, 427.
33 S. Neyertz, D. Brown and J. O. Thomas, *Electrochim. Acta*, 1995, **40**, 2063.
34 S. Neyertz and J. O. Thomas, *Comput. Polym. Sci.*, 1995, **5**, 107.
35 D. Brandell, M. Klintenberg, A. Aabloo and J. O. Thomas, *Int. J. Quantum Chem.*, 2000, **80**, 799.
36 D. Brandell, M. Klintenberg, A. Aabloo and J. O. Thomas, *J. Mater. Chem.*, 2002, **12**, 565.
37 D. Brandell, M. Klintenberg, A. Aabloo and J. O. Thomas, *Macromol. Symp.*, 2002, **18**, 51.
38 H. Kasemägi, M. Klintenberg, A. Aabloo and J. O. Thomas, *J. Mater. Chem.*, 2001, **11**, 3191.
39 H. Kasemägi, M. Klintenberg, A. Aabloo and J. O. Thomas, *Solid State Ionics*, 2002, **147**, 367.
40 H. Kasemägi, M. Klintenberg, A. Aabloo and J. O. Thomas, *Electrochim. Acta*, 2003, **48**, 2273.
41 O. Borodin, G. D. Smith and R. L. Jaffe, *J. Comput. Chem.*, 2001, **22**, 641.
42 O. Borodin and G. D. Smith, *Macromolecules*, 1998, **31**, 8396.
43 O. Borodin and G. D. Smith, *Macromolecules*, 2000, **33**, 2273.
44 O. Borodin and G. D. Smith, *J. Phys. Chem.*, 2003, **107**, 6801.
45 F. Müller-Plathe, *Acta Polym.*, 1994, **45**, 259.
46 The DL_POLY Project. W. Smith and T. Forester, TCS Division, Daresbury Laboratory, Daresbury, Warrington, WA4 4AD, UK.
47 M. A. Ratner, in, *Polymer Electrolyte Reviews 1*, ed. J.R. MacCallum and C.A. Vincent, Elsevier, London, 1987, p. 173.
48 J. E. Mark and P. J. Flory, *J. Am. Chem. Soc.*, 1965, **87**, 1415.
49 A. Abe and J. E. Mark, *J. Am. Chem. Soc.*, 1976, **98**, 6468.
50 Th. Proffen and R. B. Neder, *J. Appl. Cryst.*, 1997, **30**, 171.

Paper III

A Molecular Dynamics Study of Short-Chain Ordering in Crystalline $LiPF_6 \cdot PEO_6$

A. Liivat[a], D. Brandell[a,*], A. Aabloo[b] and J.O. Thomas[a]

[a] *Department of Materials Chemistry, Ångström Laboratory, Uppsala University, Box 538, SE-751 21 Uppsala, Sweden.*
[b] *Institute of Technology, Tartu University, Nooruse 1, 50411 Tartu, Estonia.*

[*] *For correspondence:* brandell@vt.edu
Present address: Macromolecular and Interfaces Institute, Chemistry Department, Virginia Tech, Blacksburg, VA 24061, USA

Abstract
Molecular Dynamics (MD) simulations have been made of the crystalline short-chain $LiPF_6 \cdot PEO_6$ system to probe structural ordering for different chain-end arrangements for a methyl-terminated monodisperse poly(ethylene oxide) (EO_{23} M_w=1059) host polymer. Five different start-structures have been studied, two "smectic" and three "nematic", to represent different types of relative alignment of the end-groups between adjacent PEO chains, and different chain-end coordination situations to the Li ions. One particular situation is found to result effectively in Li-ion bridging between PEO chains along the chain axes, thereby creating continuous ion-transport pathways across the chain-breaks. This situation is also found to give rise to Li^+-$LiPF_6^-$ ion-pairing and Li-O coordination instabilities in the end-group regions, where coordination to Li ions would appear to have a more radical influence on local structure than the issue of smectic *vs.* nematic end-group alignment. It could be that such structural situations involving bridging Li ions (in both smectic and nematic arrangements) are a necessary condition for the promotion of Li-ion transport in the chain direction. Comparison of simulated and experimental XRD profiles is concluded to be an inappropriately crude and uncertain technique for distinguishing between possible short-chain ordering models.

Keywords: molecular dynamics, polymer electrolytes, ordering, crystallinity, short-chain PEO, methyl end-groups, $LiPF_6 \cdot PEO_6$

1 Introduction

Poly(ethylene oxide)-based solid polymer electrolytes have been studied considerably for 30 years as promising materials for all-solid-state rechargeable Li-ion batteries [1, 2]. By the mid 1980s, it had become widely accepted that only amorphous phases of PEO-based electrolytes conduct ions. Much of the research since then has therefore focused on suppressing crystallinity in PEO-salt complexes below their glass-transition temperature around 60 °C.

More recently, however, the discovery of new crystalline phases of $LiXF_6{\cdot}PEO_6$ (X = P, As or Sb) [3, 4] with higher conductivity than their amorphous counterparts have challenged this conventional wisdom, and raised questions as to the ionic conductivity mechanisms in these materials [5]. An increase by more that an order of magnitude in the rather low conductivity ($<10^{-7}$ $S{\cdot}cm^{-1}$) at ambient temperatures has also been reported through doping with aliovalent SiF_6^{2-} anions [6]. This effect has been modelled in our earlier work [7]. We can note that the structures of these compounds differ distinctly from other crystalline PEO-salt complexes in that they involve complete structural dissociation of the ionic species. The Li-ions are confined to lie along the tunnels formed by two PEO hemi-helices (Fig. 1). NMR data has suggested a Li^+-dominated ion transport [8]. This has been challenged in our subsequent Molecular Dynamics (MD) simulation study [7].

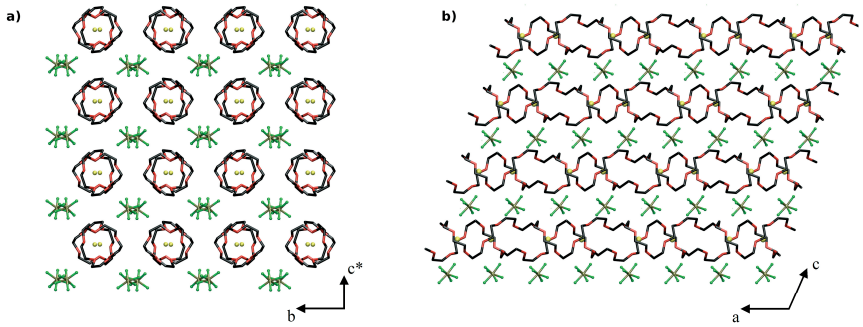

Figure 1. The structure of crystalline $LiPF_6{\cdot}PEO_6$. *a)* view along the polymer channel axis, showing the Li ions inside the channels and the PF_6^- outside; *b)* view along the unique monoclinic axis (only top layer shown for clarity), showing the cation and anion positions and chain configuration.

Unfortunately, the structural model resulting from the refinement of Neutron Diffraction (ND) data for long-chain PEO (M_w = 28400) [4] - the basis of our original infinite-chain MD model [9] - contains no information about local defects such as chain-ends, site vacancies and crystallite interfaces. It is precisely these defects which can determine the prevalence of anion or cation transport. In the absence of experimental structural data, it is therefore important to understand the role of these chain-end defect regions.

The observed increase in ionic conductivity on decreasing the PEO chain-length in crystalline phases of $LiPF_6{\cdot}PEO_6$ has previously been attributed to the increase in crystallite size [8], thereby facilitating longer pathways for ion transport and lower grain-boundary resistance. However, the experimental evidence to support this increase in crystallite size (from 200 to 250 nm) on decreasing the M_w of the PEO chains from 2000 to 1000 was based on peakwidth analysis (using the Scherrer equation) of a single XRD peak – the (0 2 1) reflection. Since this reflection is insensitive to crystallite size along the *a*-axis, which is the direction of the PEO

channels (see Fig. 1), all this tells us is that crystallite size increases slightly in directions perpendicular to the PEO channels.

We have earlier performed MD simulations for *smectic* and *nematic* arrangements of PEO chain-ends, as representing extremes of order and disorder in the spatial distributions of the methoxy end-groups [10]. In a recent paper [11], Bruce *et al.* specifically address these models when interpreting XRD and impedance spectroscopy data for crystalline systems containing poly- and monodisperse methoxy-capped (M_w ~1000) PEO chains. They attribute the lower observed ionic conductivity in the monodisperse system to a more ordered distribution of end-groups [11]; such order is clearly unfeasible in polydisperse systems. It has therefore now become highly relevant to consider the effect of increasing the concentration of chain-end defects as we go to shorter-chain PEO-salt systems. In this study, we extend our earlier MD simulations of the short-chain polymer-salt system $LiPF_6{\cdot}PEO_6$ [9] to probe a variety of spatial arrangements of polymer end-groups in $LiPF_6{\cdot}PEO_6$ crystals for the case of short-chain monodisperse PEO (M_w=1059).

2 MD methods and models

The Molecular Dynamics (MD) simulation technique involves the routine integration of classical Newton's equations of motion or a many-atom system. If this is done sequentially at sufficiently short time intervals, the procedure should result in a complete history of atomic trajectories over a limited time period. The interatomic forces are described by simple analytical functions (the force-field) involving parameters evaluated empirically or from quantum mechanical calculations. This methodology has been well established for PEO-based polymer electrolytes [12, 13].

The simulation details here are generally the same as in our earlier work [7, 9, 10]. All inter- and intramolecular force-field parameters for PEO were taken from Neyertz *et al.* [12], except for the bond-stretching and methyl-group rotation potentials; these are adapted from Jaffe *et al.* [14] and Borodin *et al.* [15]. The parameters for the interaction of PEO, Li^+ and PF_6^- are taken from [16, 17]. Simulations were run using the DL_POLY [18] program at 293K, employing a Nosé-Hoover thermostat with temperature relaxation time of 0.1ps. A constant volume ensemble (NVT) was used for 1 ns, followed by a constant anisotropic pressure (NσT) simulation for 1ns, with a corresponding relaxation time 0.3ps. Trajectory data were sampled at 0.1ps intervals for subsequent analysis.

The start structures in the MD simulation boxes comprised 4 × 2 × 4 unit cells of crystalline $LiPF_6{\cdot}PEO_6$ [4] (see Fig. 1), with dimensions: a = 46.928 Å, b = 34.750 Å, c = 34.768 Å, β = 107.8°, involving 32 PEO hemi-helices of CH_3-$(OCH_2CH_2)_{23}$-OCH_3, along with 128 $LiPF_6$ units. Terminal methyl groups were incorporated by breaking a C-C bond in the chain and attaching an extra hydrogen atom to each end-carbon, with H-C-H angles constrained to 109.45^o and C-H distances to 1.1 Å. Both CH_3-groups were constrained to preserve (C_{3v}) symmetry, and rotated both about the C-O and O-C_{meth} bonds using a Monte-Carlo procedure to arrive at an orientation free from steric hindrance.

As in our earlier simulations, it was found that Li-ion jump events were virtually non-existent in the absence of an imposed electric field. To learn anything about the structural conditions which relate to ion mobility, it was there necessary to create a range of models to represent different structural situations we might reasonably expect to encounter in this type of system. A related approach has been used by Vouyovitch *et al.* to try to predict the 3D structure of a novel polythiophene, where no

crystallographic structure determination was possible [19]. In total, five models were simulated: two *smectic* and three *nematic*; see models **1-5** in Fig. 2:

Smectic-A (**1** in Fig. 2): the chain-ends are here all arranged in planes to form a common interface, with the Li ions all 6-fold coordinated to ether oxygens within the same PEO double hemi-helix (three from each); see also the upper figures in Fig. 2.

Smectic-B (**2** in Fig. 2): same as *Smectic-A* except that Li ions now bridge the interface and are coordinated to PEO chains on both sides of the *smectic* plane. In this way, we introduce a disorder feature into the Li-ion coordination at the interface. Again, see the upper figures in Fig. 2.

Nematic-A and *Nematic-B* (**3** and **4** in Fig. 2): these models derive from their corresponding *smectic* counterparts through random displacement of neighbouring hemi-helical PEO pairs along the channel direction. These types of configuration were suggested by Bruce *et al.* to best represent the crystal structure for monodisperse systems [11].

Nematic-R (**5** in Fig. 2): this is the most disordered of the models simulated in which all chain-breaks occur randomly throughout the structure. This model corresponds to that proposed in [11] as the most rational structure for polydisperse systems.

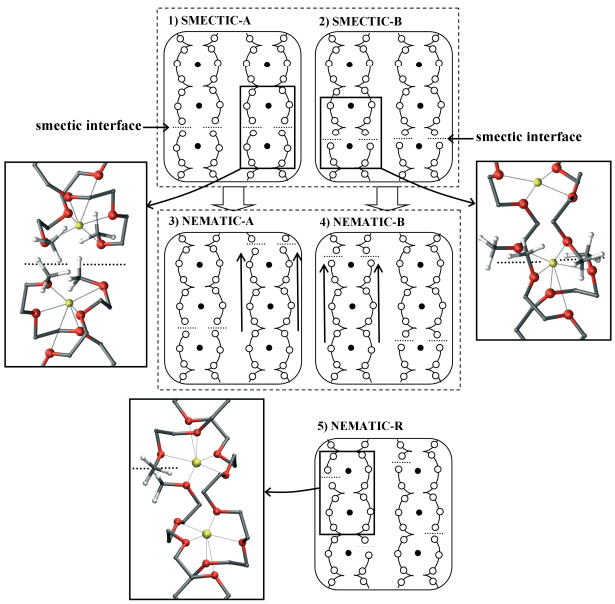

Figure 2. A schematic representation of the models simulated for $LiPF_6{\cdot}PEO_6$; 1) *Smectic-A* with the chain-breaks outside the 6-fold Li-O coordination sphere; 2) *Smectic-B* with the chain-breaks perturbing the 6-fold Li-O coordination; 3) and 4) *Nematic-A* and *Nematic-B*, derived from the corresponding *smectic* models by shifting adjacent PEO channels along their axes (see arrows); 5) *Nematic-R* has randomised chain-break locations. Typical snapshots of structural detail within chain-break regions are given at the top of the figure.

Within this *smectic*/*nematic* classification of start structures, we also distinguish two types of chain-end coordination around the Li ions: *ideal* coordination, in which chain termination does not disrupt either of the polymer chains involved in the 6-fold coordination sphere of a Li ion, and *broken* coordination, where this is not the case. *Smectic-A*, and *Nematic-A* thus involve *ideal* coordination, while *Smectic-B* and *Nematic-B* contain *broken* coordination. *Nematic-A* involves both types of coordination, but where the majority are broken.

This issue of order/disorder in Li-ion coordination has largely been overlooked earlier because the crystalline oligoether-salt complexes studied have involved either very short monodisperse PEO oligomers [20-23], where the coordination in stoichiometric complexes is well defined, or much longer polydisperse chains, where the lower concentration of chain-ends renders them of minor significance. However, a study of single crystals of PEO_3(MW~500)$LiCF_3SO_3$ has revealed a high selectivity to polymer chain-lengths on crystal formation [24]. Chain ordering is therefore analysed in terms of two distinct structural features: *(i)* ordering of neighbouring chain-ends; and ii) the coordination (*ideal* or *broken*) of Li ions to the polymer chain, since short-chain ordering has been proposed to be a significant factor in determining ion transport mechanisms in these materials [11].

3 Results and discussion

Visual inspection of sampled snapshots could readily confirm that all the simulated systems maintained the general characteristics of their start structures – with cylindrical double hemi-helical PEO channels still separating the Li^+ ions within the channels from the PF_6^- anions outside the channels. All structural disruption is located in the vicinity of the end-groups. A modest incidence of ion-pairing is also noted in the systems involving broken Li-ion coordination in the defect regions.

Another observation is that the shape and size of all MD boxes are generally retained for all models when their geometry is released on going from NVT to NσT ensemble simulation. Interestingly, all boxes tend to shift in the same general way: the *a*-axes (the polymer-chain direct) all expand (on average by 2.5%), which could reflect that the attractive forces between chain-ends are too weak, while the *b*- and *c*-axes both contract by roughly the same amount (on average by 2.6 and 2.7%, resp.), clearly indicating that the attractive forces between the polymer chains are too strong. It is clearly not meaningful to attempt to extract any more detailed information than this from these observed discrepancies; the relationship between the NσT MD-box shape/size and individual structural features is so complex.

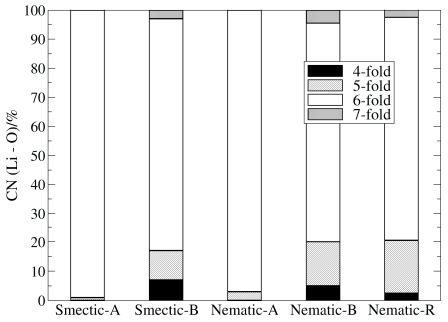

Figure 3. Distribution of Li coordination numbers CN(Li-O) for the five simulated $LiPF_6{\cdot}PEO_6$ systems (see Figure 2).

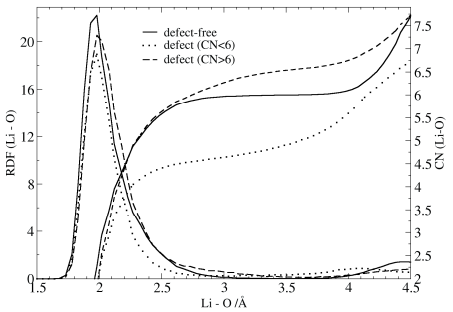

Figure 4. Li-O radial distribution functions RDF(Li-O) and coordination numbers CN(Li-O) for the *Nematic-B* $LiPF_6{\cdot}PEO_6$ model with defect-free and defect regions plotted separately.

3.1 Li-O coordination and ion-pairing

The models involving ideal 6-fold Li-O coordination all maintain this coordination number (CN) throughout the simulations, even in defect regions (see Fig. 3; *Smectic-A* and *Nematic-A*), while CN(Li-O) is seen to vary from 4 to 7 in the remainder of the systems simulated. Such variations in broken-coordination situations occur mainly in defect regions involving 2-3 Li-ions (Fig. 4). The 7-fold Li-O coordination (dashed line in Fig. 4) is unstable, with the 7th coordinating oxygen spending typically < 5 ps at a Li-O distance less than 3Å. A typical *Smectic-B* broken-coordination situation is demonstrated in Fig. 5: in the left-hand channel, the Li-ion on the lower side of the defect region remains coordinated by one end-group oxygen belonging to the next polymer chain (**A**), whereas another oxygen has migrated to coordinate to the Li-ion on the upper side of the defect (**B**). In the right-hand channel, however, both chain-ends from the polymer channel at the upper end of the defect have left the coordination sphere of the Li-ion on the lower side of the defect, resulting in two uncoordinated methoxy-groups in the defect region (**C**). This deficit of coordinating oxygens around the Li-ion on the lower side of the gap causes this channel end-region to contract, thus allowing ion-pair formation (**D**). The persistence of the "Li-bridging"

coordination (**A**) shown in Fig. 5 can have an important impact on the overall stability of the structure.

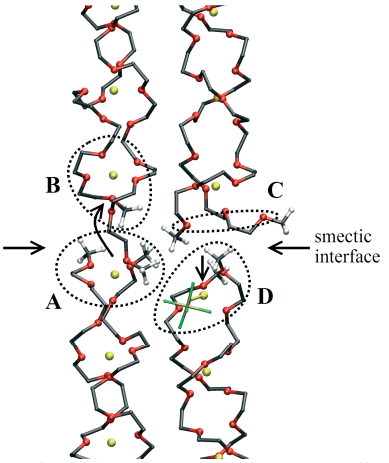

Figure 5. PEO-chain conformation rearrangements and corresponding Li coordination in the defect region of the *Smectic-B* model of $LiPF_6{\cdot}PEO_6$.

Ion-pairing thus occurs predominantly in coordination situations which involve exclusively Li-ions with low CN(Li-O); see Fig. 6*a*. Through competition with the coordinating ether oxygens, Li-F coordination is always 1-fold, unless the Li-ion has migrated outside the PEO channel. Since defect regions contain uncoordinated methoxy groups (Fig. 5 **C**), ion-pairs occasionally dissociate, thereby restoring the bridging configuration **A** shown in Fig. 5. These ion association-dissociation events occur on a nanosecond time-scale and correlate with changes in CN(Li-O); pair formation leads to a decrease in CN(Li-O) and *vice versa*.

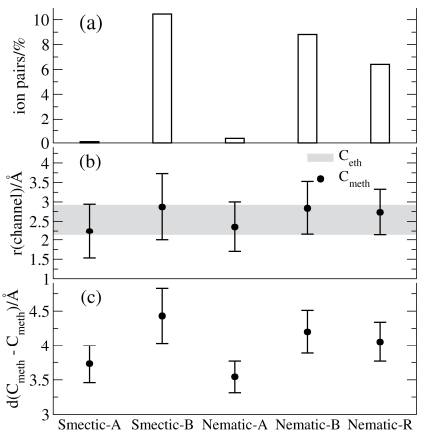

Figure 6. (a) Percentage of Li-ions participating in ion-pairing for the five simulated models for $LiPF_6{\cdot}PEO_6$ as described in Fig. 2; *(b)* chain-end methyl carbon (C_{meth}) displacements from the PEO channel axes compared to the displacements in defect-free PEO (C_{eth}); and *(c)* corresponding C_{meth}-C_{meth} separations across the chain-break regions.

The proportion of Li ions with 4-fold coordination decreases in the systems simulated in the order: *Smectic-B* > *Nematic-B* > *Nematic-A*, which correlates well with the observed decrease in ion-pair concentration. The *Nematic-A* system incorporates predominantly situations in which only one of the PEO hemi-helices in any Li-O coordination sphere is broken; as illustrated in Fig. 2. This reduces the possibilities for lower Li-O coordination, and thus leads to a higher incidence of 5-fold coordinated Li (Fig. 3). In the *Nematic-A* system, almost 50% of the ion pairs form outside the defect region, which corresponds well with the more dispersed nature of the imposed isolated defect distribution. The somewhat higher incidence of ion-pairing in the *Smectic-B vs. Nematic-B* cases is almost certainly a consequence of the more extended ordered arrangement of defects in the *smectic* case, whereby a complete defect "layer" is created in which ion-pairs are able to form more readily.

Considering the specific role of terminal groups in promoting ion-pair formation, we see that the further the methyl-group pairs move away from their positions along the channel walls (Fig. 6*c*), the more they avoid one another and thereby provide more space for ion-pair formation. From Figs. 6*a-c*, we see that the methyl end-group separation correlates well with the incidence of ion-pair formation.

3.2 The channel structure

Let us first consider how the channel structures differ in the *smectic* and *nematic* models depending on the nature of the break-defect (A, B or R) (Fig. 2). The Li-Li distances are found to reflect well the different structural situations for the Li ions, especially in the chain-break regions. In the *Smectic-A* and *Nematic-A* systems, the average distance from a Li ion in a defect region to its nearest Li neighbour is closely similar to that in a defect-free region (5.8 Å compared to 5.9 Å), while the Li-Li distance across the defect region is *ca.* 7.5 Å. This appears as an extra peak in the rdf(Li-Li) plot for the *Nematic*-A case; Fig. 7*a*. This peak is also present for the *Smectic-A* case (not shown), where a slight lateral displacement was noted in successive PEO channels in adjacent blocks (Fig. 8). This was also observed in our earlier study of a short-chain (n = 23) PEO system [9].

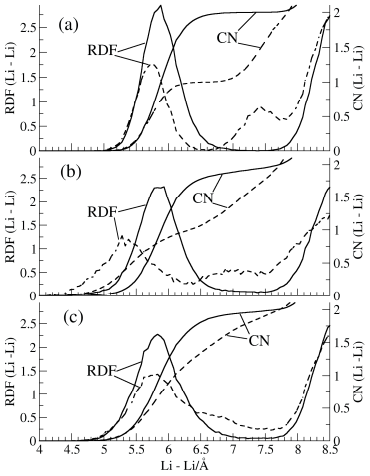

Figure 7. Li-Li radial distribution functions RDF(Li-Li) and coordination numbers CN(Li-Li) in defect-free (solid lines) and chain-defect (dashed lines) regions for different conformations of $LiPF_6{\cdot}PEO_6$: *(a) Nematic-A*; *(b) Nematic-B* and (c) *Nematic-R*.

Li ions in channel-end defect regions for CN(Li-O) < 6 (*i.e.,* B-type systems) tend to move closer to the Li ions in the end-regions of successive PEO channels; with Li-Li distances *ca.* 5.2 Å compared to 5.9 Å in defect-free regions (Fig 8*c*). The Li-Li distances *across* the defect region vary over a broad range (6-8 Å) compared to this distance in A-type systems (Fig. 7*c*), with the shorter *ca.* 6 Å Li-Li distance corresponding to the "chain-bridging" configuration shown in Fig. 5. This type of local structural arrangement provides regular continuity in the Li-ion sequence across a channel break, and could therefore facilitate the experimentally observed enhanced Li-ion transport [8]. On the basis of such structural considerations, the B-type defect would therefore seem the more reasonable.

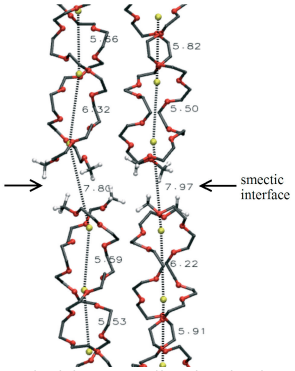

Figure 8. Chain conformations and Li-ion coordination in the chain-defect region of the *Smectic-A* model of $LiPF_6{\cdot}PEO_6$; typical Li-Li distances are indicated.

Chain defects in the *Nematic-R* model situation rarely involve both hemi-helices around a given Li ion. This appears to cause Li-Li distances in these defect regions to

vary less than in the *Smectic-B* and *Nematic-B* models; typically 2 Å *vs.* 3 Å. This is also evident from the rdf(Li-Li) plots (Figs. 7*a-c*).

In *A-type* models involving 6-fold coordinated Li ions, the methyl-groups also remain somewhat closer to the PEO channel axis compared to the B- and R-type situations (Fig. 6*a*). The shorter distance of methoxy- compared to ethoxy-carbons from the central channel-axis indicates that the Li ions in the defect regions are tightly bound to the surrounding polymers, and may well be immobilised by high activation-energy barriers to Li transport. Interestingly, even if the Li-Li distances across the gap in the *A-type* models (as discussed above) are larger than in *B-type* systems, the distance between the methyl-groups across the defect are consistently shorter (Fig. 6*c*). This is because the methoxy-groups in *B-type* systems are not coordinated to Li ions and are therefore free to migrate away from their normal positions near the PEO channel walls into the space outside the channels (see Fig. 9).

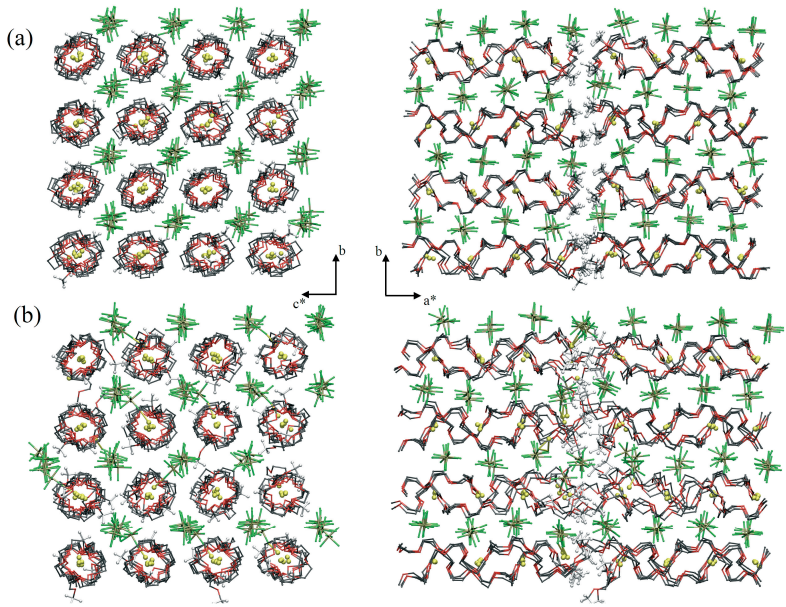

Figure 9. MD snapshots for *(a) Smectic-A* and *(b) Smectic-B* models of short-chain $LiPF_6$·PEO_6 as viewed along the *a*- and *c*-directions.

3.3 The smectic surface

One of the prime goals of this study has been to endeavour to set up what could be best be described as a smectic interfaces. This has been done by setting up an MD box in which registry has been established between an array of parallel monodisperse short-chain (n = 23) PEO double hemi-helices, thereby creating an extended plane of methyl chain-ends at either end of "nano-crystalline blocks". The periodic symmetry relating the blocks generates the required smectic interface; see Fig. 9. Clearly, interfaces are also formed on the four sides of each block, each involving sets of parallel PEO chains. As described earlier, two types of smectic model (*A* and *B*) are studied, differing only in the position of the chain-breaks with respect to the Li-ions. The behaviour of the two models is found to be quite different: in the *Smectic-B* model (Fig. 9*b*), the PEO-tunnels link together *via* "bridging" methoxy groups, and

the defect region involves disordered Li ions, which could favour ion transport. In contrast, the *Smectic-A* system (Fig. 9*a*) exhibits neither bridging groups nor disordered Li ions. Furthermore, the double hemi-helical PEO channels in the *Smectic-A* system show only small (~ 0.5 Å) lateral displacements which slightly perturb the translational symmetry of the crystallite; see Figs. 8 and 9.

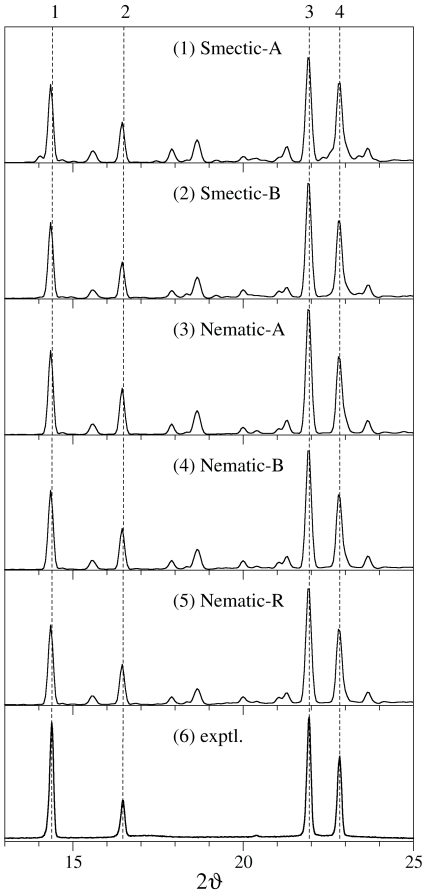

Figure 10. Calculated XRD "powder profiles" for the five MD models simulated for $LiPF_6{\cdot}PEO_6$ (1-5) as summarised in Fig. 2, using cell parameters constrained to values determined from the experimental XRD profile in the bottom figure. Peak widths have all been constrained to 0.16^o (in 2Θ) to roughly match the experimental values.

3.4 Simulated XRD profiles

XRD profiles have been calculated from trajectory data from NVT simulations (Fig. 10) for each of the system simulated, using an adapted version of the DISCUS program [25]. These can be compared with the experimental XRD profile (Fig. 10: bottom figure) [26]. In this context, however, it is most important that we first consider the basis for the appearance of particularly the experimental profile. Since experimental XRD intensities (to a good approximation) only contain information

regarding translational features in the unit-cell structure, they will therefore not contain any direct information relating to surface or chain-end features present in the material. Two interesting situations thus arise:

- The experimental XRD data will lack information on such "defect regions" lying at the surfaces of the effective diffracting mosaic blocks in the real material, and refinement of the data will therefore only reflect the structure of the defect-free regions inside these blocks. This is the situation for a *smectic* arrangement; or
- When these "defect regions" are more or less randomly distributed throughout the real structure (as is the case for the various *nematic* models simulated), then the XRD data will actually contain partial information on these defects, and refinement of the resulting XRD data will include an "averaged-in" weighted component of the defect regions superposed on the defect-free structure. In other words, the resulting refined model will fit less well to the data – but will, in this case, actually include the averaged-in effect of the defect distribution.

We are left therefore with the paradoxical situation that a better fit with experimental data could imply a *smectic* situation but would actually tell us little about the end-chain defects in the system, whereas a poorer fit could imply a *nematic*-type structure, since the effect of defects is now present in the experimental data but not in the refined model.

In practise, however, we see no significant differences in agreement with experiment for the *smectic* and *nematic* models. There are, however, added complications, *e.g.,* there is no direct correspondence between MD-box dimensions and the size of the scattering "mosaic blocks"; nor have we considered the coherence length of the diffraction process itself in relation to the size of the MD-box or the "mosaic blocks". In short, XRD is an inappropriately crude and uncertain technique for distinguishing between possible short-chain ordering models.

4 Conclusions

The effect of different imposed distributions of methoxy chain-ends in short-chain crystalline monodisperse $LiPF_6{\cdot}PEO_6$ has been studied using the MD technique. Two *smectic* and three *nematic* models have been simulated for different types of order in the chain-end registry. Rather than attempting here to identify the "correct" local structure, in view of the almost total lack of Li-ion mobility in the simulations in the absence of an electric field, it is more realistic to draw upon the somewhat fragmentary evidence available from the simulation of each of the five different models investigated, and endeavour to piece together some picture of the nature of the disorder in the material. Indeed, it is most unlikely that any genuinely "correct" structure exists – for two prime reasons:

- The low Li-ion mobility implies the probable superposition of many different metastable local structures. Our MD time-scale does not yet permit us to probe such phenomena.
- The inherent inadequacy of the XRD technique to provide definitive structural information regarding order/disorder in the system (see above).

Nevertheless, two interesting features emerge from our simulations:

- The *Nematic-R*, *Nematic-B* and *Smectic-B* models all provide a structural basis for continuous transport of Li-ions along discontinuous short-chain PEO molecules. However, it is difficult to assess the stability of this "bridging" arrangement on a macroscopic scale. It cannot be ruled out that the more *ideal* 6-fold Li-ion

coordination is adopted at chain-ends on a longer time-scale (outside the range of present-day MD simulation), through conformational rearrangement of the polymer channels.

- Simulated XRD peak intensities for all models with chain-break defects in the cation coordination sphere (*Nematic-R*, *Nematic-B* and *Smectic-B*) agrees reasonably well with experimental data.

It is possible that comparative *vibrational spectroscopy* data for mono- and polydisperse systems could distinguish ion-pairing and Li-O coordination for the different models simulated. All broken Li-O coordination regions should involve a detectable number of ion-pairs. Several spectroscopic studies have already addressed structural issues regarding $LiPF_6{\cdot}PEO_6$ and its iso-structural crystal forms [27-29]; and there is some evidence to suggest "spectroscopically free" anions in these materials.

Our simulation work in this area continues with more extensive studies of the same types of model addressed here, but under the influence of high electric fields to induced a higher degree of ion mobility.

Acknowlegements

We would like to acknowledge the support provided for this work by the *Swedish Science Council (VR)*; and DB would like to acknowledge stipends from Wenner-Gren Foundations and The Royal Swedish Academy of Sciences. The research has also been supported by a grant from the *Estonian Science Foundation (ETF)* (Grant No. 6763), and a stipend for AL from the *Archimedes Foundation.* The excellent service provided by the *UPPMAX Supercomputing Centre* is also gratefully acknowledged.

References

[1] J.M. Tarascon, M. Armand, *Nature*, 414 (2001) 359.
[2] W. van Schalwijk, B. Scrosati, *Advances in Lithium-Ion Batteries*, Kluwer Academic/Plenum Publishers, New York, 2002.
[3] G.S. MacGlashan, Y.G. Andreev, P.G. Bruce, *Nature*, 398 (1999) 792.
[4] Z. Gadjourova, D. Martin y Marero, K.H. Andersen, Y.G. Andreev, P.G. Bruce, *Chem. Mater.*, 13 (2001) 1282.
[5] Z. Gadjourova, Y.G. Andreev, D.P. Tunstall, P.G. Bruce, *Nature*, 412 (2001) 520.
[6] C. Zhang, E. Staunton, Y.G. Andreev, P.G. Bruce, *JACS*, 127 (2005) 18305.
[7] D. Brandell, A. Liivat, A. Aabloo, J.O. Thomas, *Chem. Mater.*, 17 (2005) 3673.
[8] Z. Stoeva, I. Martin-Litas, E. Staunton, Y.G. Andreev, P.G. Bruce, *JACS*, 125 (2003) 4619.
[9] D. Brandell, A. Liivat, H. Kasemägi, A. Aabloo, J.O. Thomas, *J. Mater. Chem.*, 15 (2005) 1422.
[10] D. Brandell, A. Liivat, A. Aabloo, J.O. Thomas, *J. Mater. Chem.*, 15 (2005) 4338.
[11] E. Staunton, Y.G. Andreev, P.G. Bruce, *Faraday Discuss.*, 134 (2007) 143.
[12] S. Neyertz, D. Brown, J.O. Thomas, *J. Chem. Phys.*, 101 (1994) 10064.
[13] O. Borodin, G.D. Smith, *Computational Materials Chemistry: Methods and Applications*, Ch. 2, Kluwer Academic Publishing, 2004.
[14] R.L. Jaffe, G.D. Smith, D.Y. Yoon, *J. Phys. Chem.*, 97 (1993) 12752.
[15] O. Borodin, G.D. Smith, *J. Phys. Chem.*, B 107 (2003) 6801.
[16] G.D. Smith, R.L. Jaffe, H. Partridge, *J. Phys. Chem.*, A 101 (1997) 1705.
[17] O. Borodin, G.D. Smith, R.L. Jaffe, *J. Comput. Chem.*, 22 (2001) 641.
[18] W. Smith, T. Forester, *The DL_POLY project.*, Technical report, TCS Division, Daresbury Laboratory, Daresbury, Warrington, WA4 4AD, UK.
[19] L. Vouyovitch, D. Brown, S. Neyertz, B. Gallot, *Soft Mater.*, 1 (2002) 93.
[20] W.A. Henderson, N.R. Brooks, W.W. Brennessel, V.G. Young, *Chem. Mater.*, 15 (2003) 4679.
[21] Y.G. Andreev, V. Seneviratne, M. Khan, W.A. Henderson, R.E. Frech, P.G. Bruce, *Chem. Mater.*, 17 (2005) 767.
[22] W.A. Henderson, N.R. Brooks, V.G. Young, *Chem. Mater.*, 15 (2003) 4685.
[23] V. Seneviratne, R. Frech, J. Furneaux, M. Khan, *J. Phys. Chem.*, B 108 (2004) 8124.
[24] W.A. Henderson, N.R. Brooks, V.G. Young, *JACS*, 125 (2003) 12098.
[25] T. Proffen, R.B. Neder, *J. Appl. Crystallogr.*, 30 (1997) 171.
[26] Y.G. Andreev, *Private Communication*.
[27] C. Burba, R. Frech, *J. Phys. Chem.*, B 109 (2005) 15161.
[28] J. Grondin, L. Ducasse, J.L. Bruneel, L. Servant, J.C. Lassègues, *Solid State Ionics*, 166 (2004) 441.
[29] L. Ducasse, M. Dussauze, J. Grondin, J.C. Lassègues, C. Naudin, L. Servant, *Phys. Chem. Chem. Phys.*, 5 (2003) 567.

Paper IV

A molecular dynamics study of ion conduction mechanisms in crystalline low-M_w $LiPF_6$·PEO_6

A. Liivat, D. Brandell and J.O. Thomas*

Department of Materials Chemistry, Ångström Laboratory, Uppsala University, Box 538, SE-751 21 Uppsala, Sweden.

Abstract

Molecular Dynamics (MD) simulation has been used to probe ion conduction mechanisms in crystalline $LiPF_6$·PEO_6 for smectic and nematic ordered models of methyl-terminated short-chain monodisperse poly(ethylene oxide) chains with formulation CH_3-$(OCH_2CH_2)_{23}$-OCH_3; M_w = 1059. The effect of aliovalent substitution of the PF_6^- anion by ca. 1% SiF_6^{2-} has also been studied. External electric fields in the range 3-6 × 10^6 V/m have been imposed along and perpendicular to the chain direction in an effort to promote ion transport during the short time-span of the simulation. Ion migration barriers along the polymer channel are lower for the nematic models than for the smectic, with anions migrating along the channels more readily than Li-ions. Ion mobility within the smectic interface could also be confirmed, but at a higher field-strength threshold than along the chain direction. Li-ion migration within the smectic plane appears to be suppressed by ion-pairing, while Li-ion transport across the smectic gap is facilitated by uncoordinated methoxy end-groups. Interstitial Li-ions introduced into the PEO channel through SiF_6^{2-} doping is also shown to enhance Li-ion conduction.

Keywords: molecular dynamics simulation, polymer electrolyte, conductivity mechanism, polymer chain length, methoxy end-groups, aliovalent anion substitution

**For correspondence:* josh.thomas@mkem.uu.se

1. Introduction

Solid polymer electrolytes, formed by dissolving lithium salts in a polymer matrix, have long been the object of intense research, largely because of their potential for providing relatively high levels of ionic conductivity [1-3]. Among their many applications, the most attractive is in high energy-density rechargeable Li-ion polymer batteries [4]. Poly(ethylene oxide), PEO, $(CH_2CH_2O)_n$, is especially suitable as a host-polymer through its ability to dissolve a wide variety of lithium salts, although it only exhibits a relatively low ionic conductivity; *ca.* 10^{-4} S. cm^{-1} at ambient temperatures [5].

Ionic conductivity has long been ascribed to the amorphous parts of these materials, while crystalline regions have generally been assumed to conduct ions considerably less well [6]. However, it was shown in 2001 that crystalline $LiXF_6{\cdot}PEO_6$ (X = P, As and Sb) exhibited higher conductivity than its amorphous counterparts [7]. Furthermore, diffraction studies showed that the polymer chains form hemi-helices, which arrange pairwise to provide channels for the Li-ions, with the anions situated outside these channels [8, 9]. NMR studies suggested the ion conductivity to be dominated by *cation* transport; *i.e.,* t_+ close to unity [7].

In three recent papers [10-12], we have endeavoured to model the $LiPF_6{\cdot}PEO_6$ system in a series of MD simulations. The first involved an infinite PEO chain [10] - the very same model that had been derived from the refinement of the diffraction data. Apart from an increase in the ether-oxygen (O_{et}) coordination number for Li from 5 to 6, and some minor differences in polymer dihedral angles, the hemi-helical structure and ion distribution was generally retained. Ion conduction mechanisms were then studied by imposing a range of external electric fields along the chain-axis direction [11]. Contrary to the earlier experimental result, the conduction was found to be dominated by the PF_6^- anions with $t_- = 0.9$-1.0. In this same study, the experimentally observed increase in conductivity through aliovalent anion doping [13, 14] could be confirmed for 1% substitution of PF_6^- by SiF_6^{2-} and SF_6. More recently, we have studied the structural effect of using shorter chain-lengths on these transport phenomena. An equivalent system with short-chain monodisperse CH_3-$(OCH_2CH_2)_{23}$-OCH_3 (M_w = 1059) was investigated, which closely resembled that used in recent experimental studies [15]. While still retaining well-ordered hemi-helices, the shorter chains (in one smectic and two nematic ordered models; see Fig. 1) were shown to relax more than in the infinite-chain model [12, 16] and promote higher Li-ion mobility.

Our earlier simulations of the $LiPF_6{\cdot}PEO_6$ systems addressed only one type of polymer-chain ordering – involving chain-end registry in a smectic arrangement. This is not an unreasonable model to choose, considering the large energy contribution from the formation of end-group layers. Indeed, such ordering modes occur in a broad variety of chemical and biological systems; *e.g.,* phospholipid layers, liquid crystals, bio-membranes, *etc*. However, if this smectic model actually corresponds to the true chain-ordering, then the possibility also opens for ion conductivity in the chain-end planes so formed.

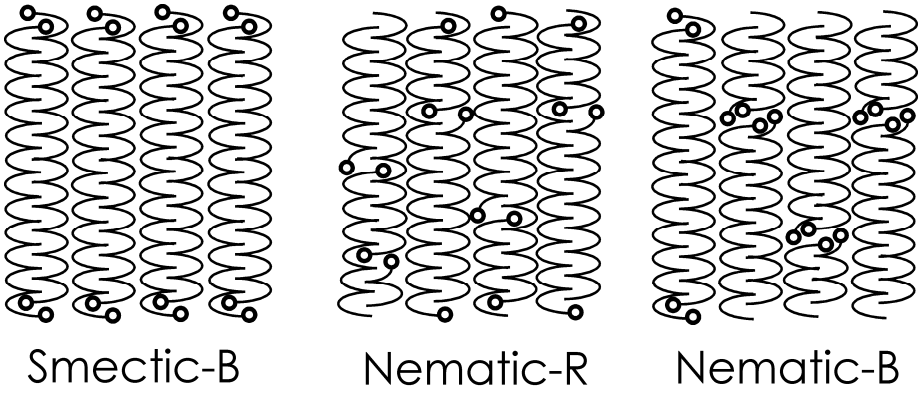

Figure 1. Schematic representation of the smectic and nematic models for short-chain monodisperse PEO; *Smectic-B* corresponds to the local situation in Fig. 8, and *Nematic-B* to that in Fig. 6.

In this present study, we apply a range of external electric fields both parallel to the chain-axis for all systems, and in the plane of the smectic interface for the short-chain systems studied in [16] (see Fig. 1). We do this with the goal of gaining new insights into the structural and dynamical basis for the ion conductivity in these ordered systems. The enhancement in conductivity following aliovalent anion substitution with SiF_6^{2-} anions is also investigated for all systems.

2. The simulated models

MD simulation is a method for modelling molecular structure and dynamics in a chemical system by generating atomic trajectories using classical mechanics within an appropriately selected periodic box. The viability of the simulation depends implicitly on the quality of the force-field description, *i.e.,* the interaction potentials between the particles in the system.

All potentials used in the simulations presented here have been used in previous studies [10-12]. All inter- and intramolecular potentials for PEO were taken from Neyertz *et al.* [17], except for those involving methoxy end-groups; these were taken from Borodin *et al.* [18] and Müller-Plathe [19]. The potentials involving $LiPF_6$ have been developed by Borodin *et al.* [20-22], while those involving SiF_6^{2-} have been developed locally [23]. The MD simulations used periodic boundary conditions and an Ewald summation routine to treat the long-range electrostatic forces. The short-range cut-off was 15 Å and the Verlet sphere used in the construction of the Verlet neighbour-list had a 0.5 Å radius. An NVT Nose-Hoover thermostat has been used consistently. A multiple time-step technique was used, with a time-step of 1.0 fs for longer distances, and a shorter time-step of 0.2 fs inside a 6 Å-radius sphere. The simulations were all performed at 328 K (to match the experimental temperature used in [14]), and the polymer simulation program used was DL_POLY [24].

The start structures in the MD simulation boxes were taken from our earlier work [16] and had been prepared as follows: a $4 \times 2 \times 4$ unit-cell the box containing the crystallographically determined structure [9] of $LiPF_6 \cdot PEO_6$ was generated with dimensions a = 46.928 Å, b = 34.750 Å, c = 34.768 Å, β = 107.8°, involving 32 CH_3-

$(OCH_2CH_2)_{23}$-OCH_3 hemi-helices, along with 128 $LiPF_6$ units; corresponding to an effective Li:EO ratio of 1:6. The structure was then relaxed in a 1 ns NVT MD simulation. Methoxy chain-ends were then incorporated into the three generated models to create *smectic-B*, *nematic-R* and *nematic-B* models, as shown in Fig. 1. Finally, 1ns NσT simulations were run to allow the structures to relax further; this led to minor (~2.5%) changes in box edge-size. As discussed in [16], these three models represent the most reasonable representations of the materials studied experimentally [15, 25], and are simpler to generate for MD simulation than the systems with PEO(M_w = 1015) studied in [12]. The *nematic-B* system represents a situation somewhere between *smectic-B* and *nematic-R,* with chain-end registry maintained only within each individual PEO channel. *Nematic-B* was proposed by Bruce *et al.* as the most likely structure for the crystal with monodisperse PEO (M_w = 1015) [25]. The infinite polymer-chain system studied in [10, 11] will be referred to as *infinite*. Three types of simulation were then made:

- A series of external fields (ranging from 3 to 6×10^6 V/m) was applied to all three $LiPF_6$·PEO_6 models (see above) parallel to the hemi-helical axes, and simulated for a further 300 ps.
- One of the PF_6^- ions in the MD box (again for all three models) was then replaced by an SiF_6^{2-} ion, and a compensating Li-ion was inserted at a metastable 4-fold site within one of the double hemi-helical channels. This corresponds to an anion-dopant concentration of ~1%, which corresponds well with that shown experimentally to result in the highest ionic conductivity [14]. The insertion of the extra Li-ion was made as far away as possible in the MD box from the SiF_6^{2-} ion to avoid spontaneous ion-pair formation [11]. All three systems were first relaxed for 300 ps, and external fields (from 3 to 6×10^6 V/m) again applied in the *x*-direction for another 300 ps.
- A series of external fields (again ranging from 3 to 6×10^6 V/m) were finally also applied in the *c*-direction parallel to the end-plane of the *smectic-B* model of $LiPF_6$·PEO_6, and simulated for another 300 ps. Some tests were made of also applying the fields in the *b*-direction within the smectic plane; these gave qualitatively identical results to the *c*-direction results.

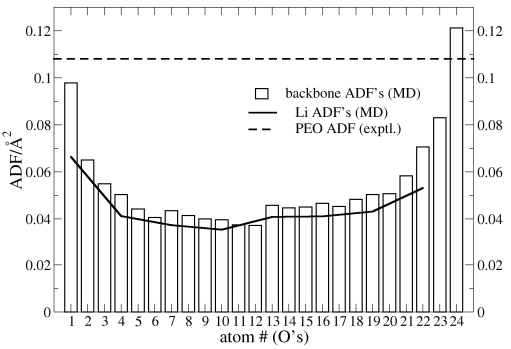

Figure 2 The atomic displacement factors (ADF's) for the backbone oxygens along the chain (n=23); the lines show our MD values for Li-ions and the experimental value for long-chain crystalline PEO [26].

3. Results and discussion

As in our earlier study [16], the general form of the "infinite-chain" structure is retained throughout all the simulations of the n=23 system despite the high concentration of end-group "defects". Isotropic atomic displacement factors (ADF's) averaged over all 32 PEO chains in the MD box have been extracted for the backbone ether oxygen atoms along the chain (see Fig. 2). Higher displacements at the chain ends are clearly reproduced, and agree well with the overall experimental value for salt-free PEO (*ca.* 0.11 $Å^2$).

3.1 Structural stability under an imposed electric field

The stability of the structure can be estimated crudely by probing the threshold value of the applied external electric field at which the structure begins to distort. As in our earlier simulations of ion transport in an *infinite* system [11], translational symmetry was lost above a certain threshold field, which varied from system to system (see the right-hand column of Table 1). Two main conclusions can be drawn:
(*a*) The *smectic-B* model is the most stable, and the *nematic-R* model the least stable.
(*b*) The crystalline structure is less stable when the electric field is applied in the direction of the PEO channel compared to perpendicular to the channel. All types of double hemi-helices modelled undergo breakdown within the 300 ps simulation sampling time under fields greater than the structural instability threshold value (right-hand column in Table 1). No significant differences in stability could be detected between the doped and undoped systems.

Table 1. Stability of the models simulated under the effect of an electric field applied along the *a*-axis (the PEO-chain direction), and in the *c*-direction perpendicular to the chain-direction within the smectic surface; sampling time: 300ps.

System	Field direction	Lower threshold /10^6V/m (no jumps)	Upper threshold /10^6V/m (unstable)
Smectic-B	c	>5.0	>6.0
	a	<4.75	5.0
Nematic-B	a	4.25	>4.5
Nematic-R	a	<4.0	<4.25

The *infinite* systems studied earlier [11] were all stable up to an applied field of 5×10^6 V/m. The breakdown process when the system became amorphous could be correlated to the extraction of Li-ions from inside the double hemi-helices. Two of the short-chain systems studied here are found to be less sensitive than the *infinite* system to the extraction of Li-ions from the polymer channels. For example, in the *smectic-B* case, as many as 8 Li-ions within the simulation box can leave their hemi-helices over 300 ps period without structural breakdown occurring. The corresponding number for the *infinite* system was only 2-3 Li-ions for a field strength greater than 5×10^6 V/m. The *nematic-B* model was also less sensitive to Li migration (4 Li-ions could be withdrawn from the helices without it losing its structure) than the *infinite* case, though not as stable as the *smectic-B* model. The least stable in this respect is the *nematic-R* sys-

tem, where structural distortion begins as soon as Li-ions exit the PEO channels. Generally, when two adjacent Li-ions leave a channel, this region of the polymer loses it original conformation, and the individual chains straighten out and separate from one another; see the dashed region in Fig. 3. It was also pointed out earlier by Henderson *et al.* [27] that the cylindrical two-chain configuration is unlikely to be preserved if ether oxygens do not coordinate Li-ions. This is a clear indication that the two more ordered short-chain systems (*smectic-B* and *nematic-B*) are less dependent on the presence of Li-ions for their structural stability, while an *infinite* system is highly reliant on Li-ions to hold its hemi-helices together. This type of chain relaxation in short-chain systems makes them more stable, despite the fact that they host fewer Li-ions within their channels.

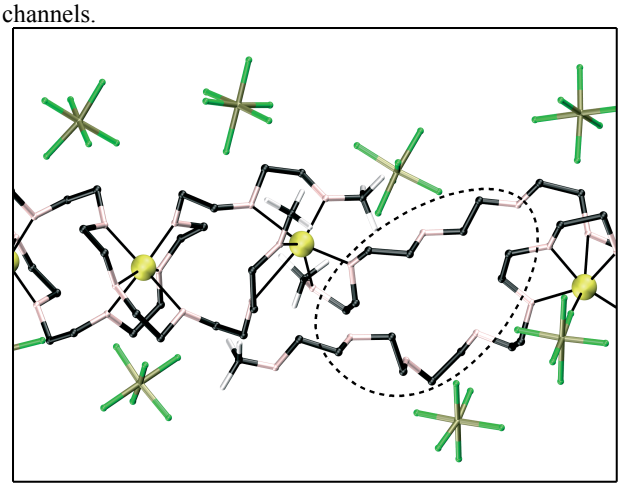

Figure 3. An example of the breakdown in continuity of the double hemi-helical chain structure (the circled region) across a defect under the effect of an applied electric field.

Those Li-ions which actually leave their hemi-helices in the *smectic-B* case move into the extended interlayer regions between the blocks to form ion-pairs or -clusters with the PF_6^- ions [12]. Similarly, in the *nematic-R* system, Li-ions leave the PEO channels near the chain-ends, where they also pair-up with anions. At the same time, the methoxy end-groups tend to retain their coordination to the Li-ions, and are dragged away from their normal locations into the anion channel. Given the more uniform distribution of chain-ends in the *nematic-R* arrangement, chain breakdown is initiated simultaneously at a number of sites throughout the structure. This explains why the *nematic-R* system has such a low tolerance to Li-ion migration from the channel.

3.2 Ionic conductivity

Rather than calculating ionic conductivity values from diffusion coefficients derived from mean-square displacements of different ion-types (a most unreliable procedure in view of the poor statistics from short simulation times), comparative values are derived for the different systems by counting *ion-jumps* in the direction of the imposed field. Ion conductivity (σ) in electric field E can be derived from the frequency of ion jumps (n) for the 1-D case using the expression:

$$\sigma = \frac{j}{E} = \frac{\Delta q}{\Delta t \cdot s \cdot E} = n \cdot \frac{r \cdot e}{a} \cdot \frac{1}{\Delta t \cdot b \cdot c \cdot \sin\beta \cdot E} \approx 5 \cdot 10^3 \, \frac{n}{E} \left[\frac{S}{cm} \right]$$

where we use the MD-box geometry (*a, b, c,* sin β), the characteristic Li jump-length (r = 2Å) and $E = 10^8$ V/m (an estimate of the thermal excitation at the temperature of the simulation: 328K); the value of r corresponds to a Li-ion propagation distance of one O_{et} - O_{et} distance. This gives an estimated jump frequency (n) of 0.05 jumps/ns for a conductivity (σ) of 10^{-6} S.cm^{-1}. Under these circumstances, it is quite unrealistic to hope to quantify conductivity values on the basis of observed jump frequency; it is preferable to establish the most likely pathways for ion transport, as evidenced by observed ion migration modes under the effect of electric field. However, local conductivity measurements in amorphous polymer electrolytes using microelectrodes suggest that conductivities along the most conducting pathways can be 10^3 times higher than macroscopically measured average conductivities [28].

It was established from several test simulations that a very narrow window of electric field strength exists within which ion migration can be observed without structural instability. The lower electric field threshold values are shown in the Table 1. Ion conductivities have therefore been quantified for the different short-chain systems modelled at the electric field-strength threshold values where ion jumps clearly begin to occur.

Two types of ion-jump can be distinguished *in the direction of the PEO channels*: longer jumps corresponding to typical Li-Li distances in the material (~6 Å), and shorter jumps of around 2-3 Å (see Fig. 4). These short jumps correspond to Li migration within the PEO channel involving only a few (up to 4) O_{et} atoms. From Table 2, it is clear that shorter jumps are more common for Li-ions, whereas anions tend to undergo longer jumps (also ~6 Å). These occur cooperatively, involving a sequence of neighbouring anions. Similar jump correlation is also observed in the shorter jumps, but these are typically separated by time intervals of typically ~10 ps**.**

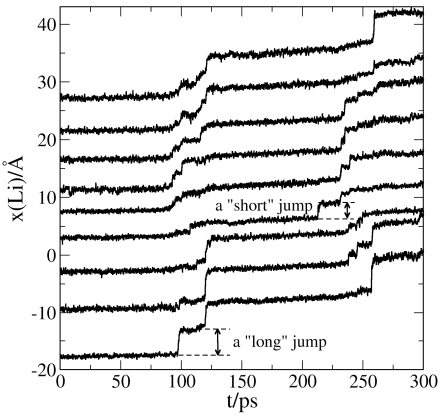

Figure 4. The x-coordinates (along the polymer-chain direction) for the Li-ions along a PEO channel plotted over 300 ps for the short-chain $LiPF_6{\cdot}PEO_6$ (n=23) system at E=4.5 × 10^6 V/m.

Some similarities to the *infinite* system are seen in Table 2. Firstly, the electric fields values for the onset of ion transport are similar (above 4 × 10^6 V/m). Secondly, longer anion jumps clearly dominate. However, there are also some important differences: large variations in anion jump-rates occur from system to system; this must be explained later. More importantly, the number of short Li-jumps as compared to the

number of anion jumps increases significantly in going from the *infinite* system (where it was at best ~25 /ns) to the short-chain systems.

Li-ion conductivity appears to benefit most from the short-chain relaxation. It was noted earlier for the case of Li-ion transport in infinite-chain systems [11] that Li-ions hardly migrate along the polymer double hemi-helices. In most of the models simulated here, Li-ions undergo fewer longer jumps than the PF_6^- ions since longer jumps require a collective sequence of participating sites, which is inhibited by strong local Li-O_{et} interactions. Predominantly short Li-ion jumps were also seen in the infinite-chain system [11], but in the short-chain situations simulated here, they clearly dominate even over short anion jumps. This raises the question as to whether it would be possible to observe only short jumps at lower electric fields if longer simulation times were feasible. Indeed, only short jumps occurred in the undoped *nematic-R* simulation (Table 2), which would appear to support the notion of the dominance of Li-ion transport, as suggested by Bruce *et al*. on the basis of NMR measurements [7]. It is certainly clear that the transport number for Li-ions is here considerably higher than in the infinite-chain systems, where it was only 0-0.1 [11], but where poor statistics disallowed any attempt at further quantification.

Table 2. Number of ion-jumps/300 ps for the systems simulated.

System		Field/ 10^6 V/m		Li^+ jumps < 4.5 Å	Li^+ jumps > 4.5 Å	PF_6^- jumps < 4.5 Å	PF_6^- jumps > 4.5 Å
Smectic-B	Undoped	∥	4.75	13	2	9	33
		⊥	6	12	0	8	4
	SiF_6^{2-} -doped	∥	4.75	18	1	16	15
		⊥	6	11	3	11	6
Nematic-B	Undoped	4.5		18	3	6	48
	SiF_6^{2-} -doped	4.5		18	7	0	4
Nematic-R	Undoped	4.0		7	0	2	0
	SiF_6^{2-} -doped	4.0		12	1	1	9

Two types of jump also occur *within the smectic plane:* shorter jumps of up to 4.5 Å, and long jumps of ~8 Å (Table 2). These distances correspond to the half and full distance between neighbouring channels (anion or cation), with longer jumps occurring considerably more infrequently. Longer anion jumps are also correlated, but the higher degree of disorder in the smectic plane means that this correlation and also the types of site occupied are less well defined than within the more ordered channels. There is also the problem that the majority of shorter jumps are ineffectual in the sense that many ions subsequently jump back to their original sites and therefore do not contribute to the overall transport of charge. Clearly, ion conduction is less in the smectic plane than along the PEO channels, as indicated by the higher electric field needed to induce it (see Table 2). This is not unexpected, since there is no structural continuity in these planes (typically in the form of ion channels), especially for Li-ions which have to cross the gap between two approximately aligned PEO channels. The limiting factor for this to occur is ion-pairing in the interchannel space. Mobile methoxy groups within the smectic plane clearly assist Li-ion transfer by coordinating

to them from both sides of the gap. However, such interactions are too weak to facilitate efficient migration.

3.3 Li-ion conduction mechanisms within the PEO channels

It is seen that Li-ion jumps occur near to Li-PF_6 pairs or in regions where the PEO-chain conformation has become perturbed under the action of the crystal field. A basic requirement seems to be the availability of a low CN(Li-O). In our earlier study, we found generally that more ion-pairs and uncoordinated ether oxygens are found near the chain-ends [16]. In *smectic-B* system, these lower CN(Li-O) values are therefore confined to the smectic interface, separated by highly ordered regions; while they are more uniformally distributed throughout the *nematic* systems. The concentration of 5-fold coordinated Li-ions is found to be highest in the *nematic-R* (18%) and lowest in the *smectic-B* case (10%) [16]. Unlike in the *smectic-B* case, however, a substantial number of Li-ions with CN(Li-O)<6 are found in defect-free regions of the *nematic* systems. Li-ion coordination would appear to be more stable in the ordered regions of the *smectic-B* system. This would all suggest that Li-ion conductivity within the PEO channels is lower in the *smectic-B* than in the *nematic-B* and *nematic-R* systems, which is consistent with the higher electric field needed to trigger Li-ion migration in the *smectic-B* system.

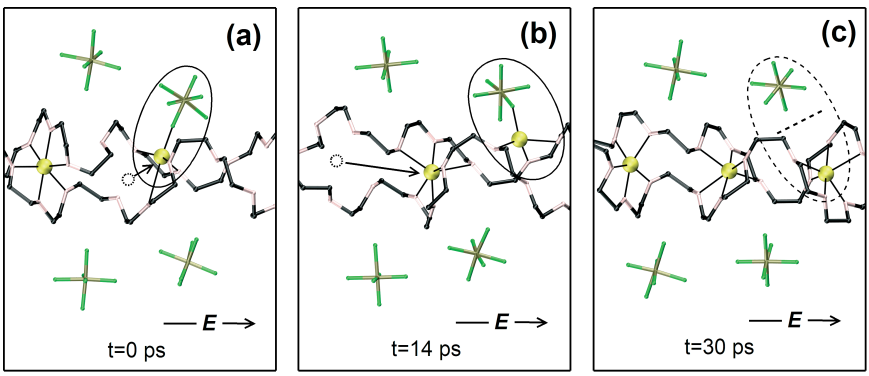

Figure 5. An anion-mediated Li-ion conduction mechanism inside a PEO channel: (a) ion-pair formation followed by (b) ion-pair migration and simultaneous Li-occupation of the vacancy site left as a result of the pair formation; and finally (c) ion-pair breaking and Li-occupation of an available vacancy site.

A new Li-ion conduction mechanism also appears in the short-chain systems which was not seen in the earlier infinite-chain model simulations; namely, anion-mediated Li-ion transport as seen, for example, in the *nematic-B* model. This resembles the anion conduction mechanism first seen in the *infinite* system, where short-lived ion-pairs at the PEO channel edge create free space for the anions to migrate. However, the picture is reversed for Li ions which move along the PEO channel *via* the types of step illustrated in Fig. 5. Li-ion displacement to create an ion-pair leaves behind a vacancy and an uncoordinated O_{et} atom (Fig. 5*a*). This vacancy is subsequently occupied by a Li-ion (Fig. 5*b*), and the ion-pair finally breaks (Fig. 5*c*). In this way, a sequence of Li-ions moves along the channel. The important difference compared to the Li-ion conduction mechanism described for the *infinite* system is that longer jumps occur here, as seen in Table 2.

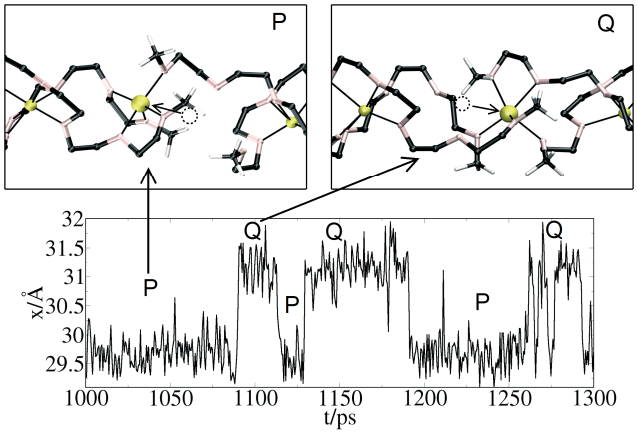

Figure 6. Li-ion dynamics (without external electric field) in the defect region; P and Q are snapshots of two Li positions before (P) and after (Q) jumps across the defect gap. The lower figure shows typical times spent in these two types of site.

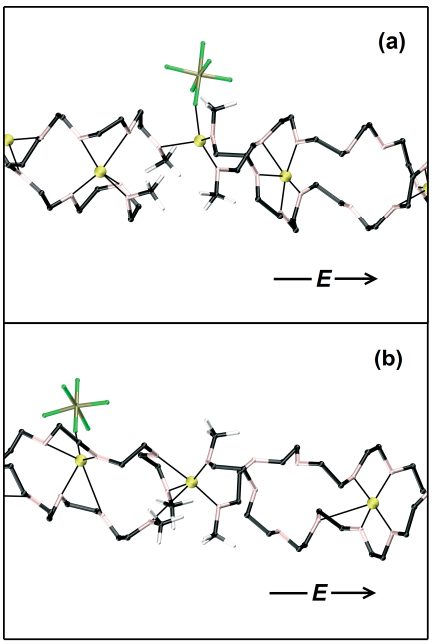

Figure 7. Li-ion migration mechanisms across the defect gap under an imposed electric field along the chains: (a) when mediated by ion-pair formation, and (b) direct migration into an available vacancy site.

Poor statistics in the Li-ion jump count makes it difficult to compare the barriers for Li-ion migration across the two types of defect gap (Fig. 1; *nematic-B* and *nematic-R*). This barrier can be low in *nematic-B* systems (Fig. 6), where local hopping (Fig. 6; P⇔Q) occurs across the gap during the 300ps sample time under zero applied external field. Generally, Li-ion migration is observed for 3-6 available (uncoordinated) O_{et}

in the jump-destination region (Fig. 7*b*). With less available O_{et}, ion-pair formation is more likely (see Fig. 7*a*). When a vacancy extends over more than one Li site, *i.e.,* when we have > 6 uncoordinated O_{et} atoms, Li-ion migration is suppressed, since the PEO double hemi-helical channels breaks down; as shown in Fig. 3.

3.4 Anion conduction mechanisms outside the PEO channels

In the *infinite* system, the longer *anion* jumps always occurred sequentially for a row of PF_6^- ions along the inter-helical channels. This mechanism was shown to be related to ion displacements perpendicular to the polymer chains (the *yz*-direction), whereby one anion is paired with a Li-ion still within the double hemi-helix. Such *yz*-displacements of the anions are often precursors to motion in the channel-direction, thereby creating a vacancy into which a neighbouring anion can move. Long PF_6^- jumps still occur predominately between different anion sites, but the sequential movement is always interrupted somewhere along the anion column. In the *smectic-B* case, this often occurs at the interface region in conjunction with ion-pair formation. As shown earlier (Fig. 7*a*), an ion-pair formed at the interface can dissociate and re-open the channel for subsequent ion motion, but high carrier concentration at the smectic interface promotes aggregation of ionic species, and the ion-clusters so formed block migration in the corresponding anion channel (Fig. 8).

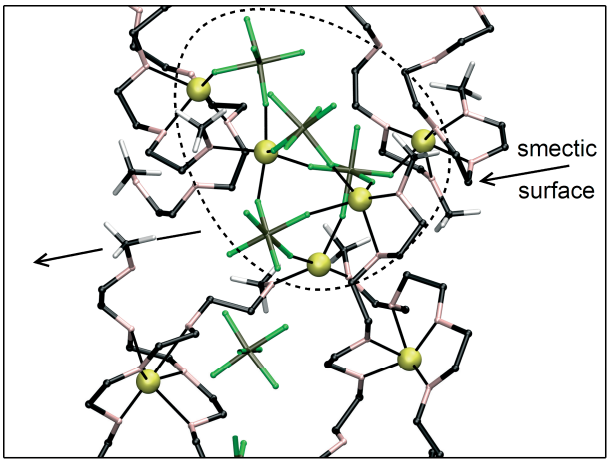

Figure 8. Ion-clustering in the smectic interface, which suppresses anion migration along the channel. The dashed region marks the boundary of a +1-charged ion-cluster region involving 5 Li-ions and 4 anions.

In the *short-chain* systems, in addition to long correlated anion jumps, shorter un-correlated anion jumps occur in isolation or sequentially in pairs. This process has two origins: *(i)* the more mobile methoxy groups create space near the chain-end defects for anions close to the PEO channel walls (Fig. 9b Q) and *(ii)* ion-pairs are formed near the chain-end defects with longer lifetimes than in the *infinite* system; these influence the available positions for the neighbouring anions. A typical anion transport sequence is shown in Fig. 9, taken from the *nematic-B* simulation; uncoordinated methoxy groups move deep into the anion channel, but do not block it. Instead, space is provided into which anions can migrate, thereby leaving vacancies behind them.

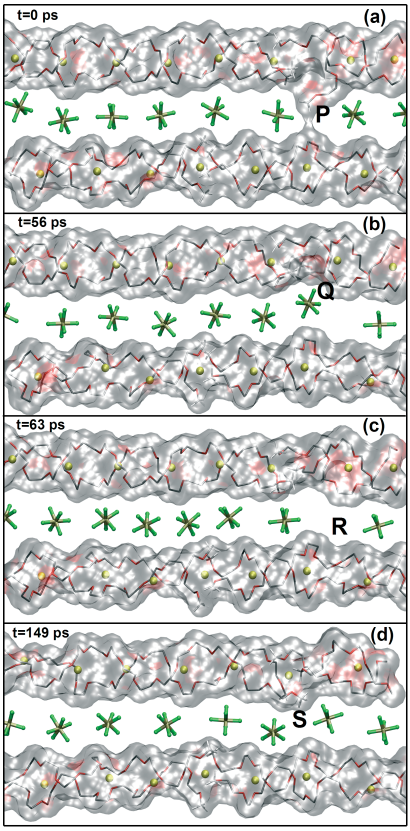

Figure 9. Typical events in the anion and Li/PEO channels (shown as excluded volumes) in the *Nematic-B* model: (a) an uncoordinated methoxy group (P) moves into the anion channel; (b) a mobile chain-end provides space which becomes occupied by an anion (Q) and leaves behind a vacancy; (c) the vacancy-site (R) is not occupied immediately because of a structural blockage; (d) the vacancy-site is then occupied by an anion, but the anion channel is blocked as a result of structural chain rearrangements.

3.5 Conduction mechanisms within the smectic plane

Conduction within the smectic plane begins at higher electric fields than along the tunnels (as discussed in Section 3.3), implying a higher activation barrier to ion motion. For Li-ions, this barrier corresponds to that for exiting the PEO channel and breaking ion-pairs. For anions, this barrier is greater due to the steric hindrance with respect to the polymer. The migration of Li-ions within the smectic plane is governed by two mechanisms: *(i)* direct migration, where PEO chain-ends move far enough into the anion channel to come into contact with one another - allowing Li-ions to use this as a bridge; and *(ii)* indirect migration involving ion-pair formation as an intermediate step. Direct Li-ion migration is a fast process, while Li-ions are immobilised in the anion channel for the full duration of the simulation in the course of indirect migration. The first process is much less frequent, from which we can conclude that Li-ion conduction is very low.

Anions appear to migrate more easily within the smectic interface than Li-ions (Table 2). This process involves two steps: anion migration into the gap between the

two PEO chain-ends and transient pairing with Li-ions, followed by breaking the ion-pair and migrating into the neighbouring anion channel. This process appears to involve local correlation – a vacant site is needed nearby to which the anion can migrate.

It is interesting to compare the PEO (n=23) (M_w=1059) system studied here and in [16] with the PEO (n=22) (M_w=1015) situation modelled in [12]. The major difference lies in the behaviour of the smectic models, where more space is left in the n=22 case for the chain-terminating methoxy groups. In the earlier n=22 smectic model, the end-group layer served as a bottleneck for ion conduction along the direction of the applied field, through the formation of stable ion-pairs/-clusters (Fig. 10). Fewer ions could migrate across this surface than within the "bulk" regions free from end-groups. Anion transport occurs across the interface only when the end-groups move aside to create the necessary free volume. A similar bottleneck was found in the earlier n=22 *nematic* systems, where "kinks" occurring close to the end-group regions blocked anion movement. However, the n=22 systems conduct ions at lower electric fields than in the n=23 systems [29].

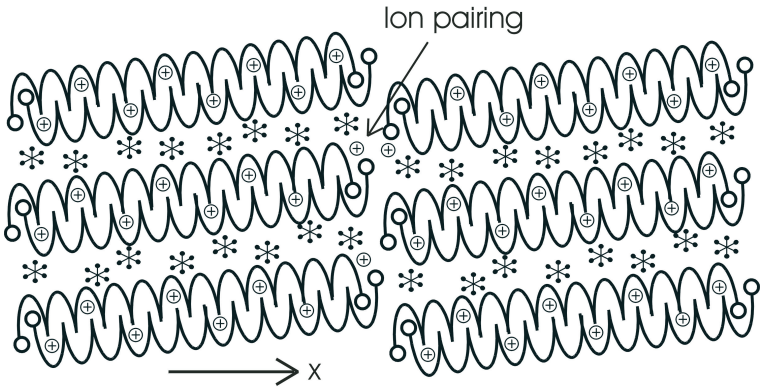

Figure 10. The "bottleneck" effect seen in the n=22 smectic model as a result of tilting of PEO-channels.

We can also note a clear difference in ordering within the smectic interface: the coordination of Li-ions in the interface region is lower (<6) in the *smectic-B* system studied in [16]. This leads here to ion-clustering, which involves typically three or more anions and cations (see Fig. 8), since the electric field forces them more easily out of their normal positions. The ion-exchange rate between these clusters and the solvating polymer appears to be a limiting factor for ion transport. We can compare this behaviour with that in the more ordered *smectic-A* interface in [16] under the same in-plane electric field; much longer anion jumps were observed and no ion-clustering, since the Li-ions could not leave their sites (Fig. 11).

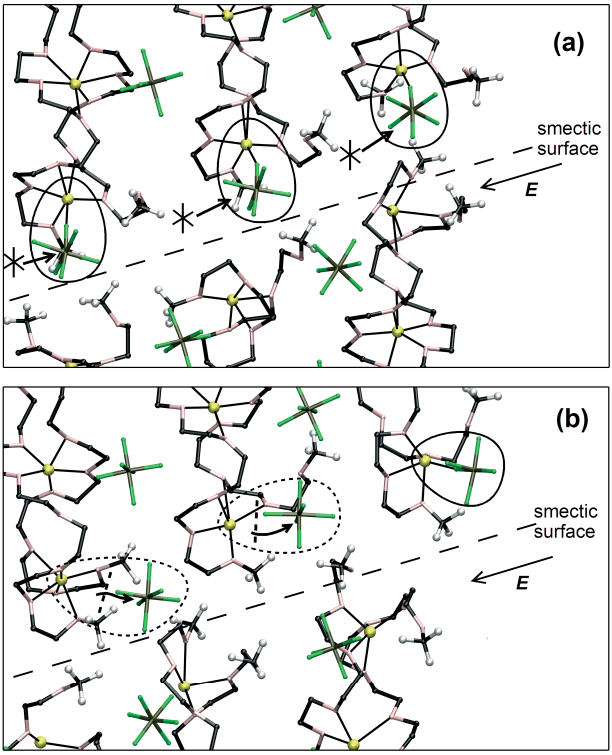

Figure 11. The two significant steps in the anion migration mechanism within the smectic plane: (a) anions move into the gap between the chain-ends to form ion-pairs (this can be accompanied by a change in CN (Li-O) and chain-end movement into the space of the anion channel); (b) these ion-pairs break and the anions move into the next anion channel.

3.6 The effect of doping

Doping $LiPF_6{\cdot}PEO_6$ with ~1% SiF_6^{2-} ions has been shown experimentally to enhance its ionic conductivity [13, 14]. This was seen in MD simulations of the *infinite* system as a lowering of the threshold field needed for ion motion [11]. The effect is less clear for the short-chain case (Table 2), with all systems exhibiting ion mobility irrespective of doping. The only significantly higher conductivity is seen for the *nematic-B* model, where a sequence of Li-ion jumps occurs in the channel containing the compensating Li-ion (Fig. 12). The mechanism is of the "anion-mediated" type discussed earlier.

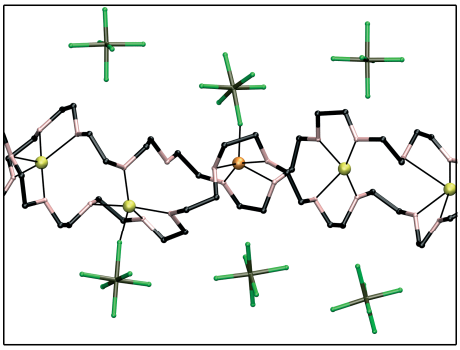

Figure 12. The situation for an extra Li-ion (orange) introduced through doping with SiF_6^{2-}; it occupies a metastable site coordinating to 4 ether oxygens and one fluorine atom. This pair is broken when this Li-ion migrates along the channel.

The SiF_6^{2-} dopant ion itself does not actively participate in the conduction process, but remains immobile or diffuses to defect regions throughout the simulations. It remains uncoordinated if far away from a structural defect, *i.e.,* away from chain-ends. However, Li-ions which have migrated to a metastable site within the PEO channels form ion-pairs with SiF_6^{2-} in defect-free regions. If the SiF_6^{2-} dopant is close to the defect region, it either forms an ion-pair with one Li-ion in an energetically favourable C_{3v} conformation [23], or a cluster involving two Li-ions - one in C_{3v} and another in C_{2v} conformation; see Fig. 13. This behaviour would appear to have a significant effect on anion mobility along the channels; the number of long anion jumps in the undoped and SiF_6^{2-}-doped *nematic-B* systems is 48 and 4, respectively, under the influence of the same electric field (see Section 3.5).

For CN(Li-O)<6, Li ions are pulled out from the channel, but continue to coordinate to ether oxygens, causing them to point outwards from the channel. This configuration appears to suppress nearest-neighbour Li-ion migration, since there are no ether oxygens available for coordination.

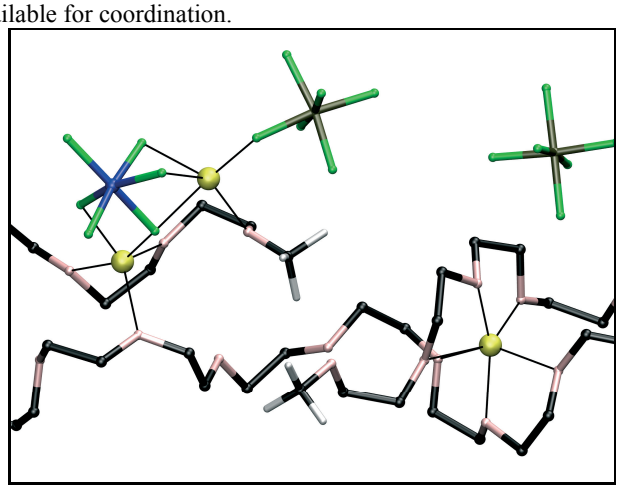

Figure 13. A typical ion-pairing situation for the SiF_6^{2-} dopant near the defect region, shown for the nematic-R system.

4. Conclusions

A number of general conclusions can be drawn from our simulations:

- Ion migration barriers along the channels are lowest in the *nematic-R* and highest in the *smectic-B* case.
- Anions tend to migrate more than Li-ions along the PEO channels, but ion migration through short jumps (seen at lower field strengths) is dominated by Li-ions.
- Ion conduction within the smectic interface is lower than along the PEO channels.
- Anions tend to be more mobile than Li-ions within the smectic interface.
- Uncoordinated methoxy groups support Li-ion migration.
- Aliovalent anion doping introduces extra Li-ions into the system. When such a Li-ion lies inside a PEO channel, this channel becomes more conducting; when outside the channel or in a defect region, it forms an ion-pair.

5. Acknowledgements

This work has been supported by grants from *The Swedish Research Council* (VR) and *The Swedish Institute* (SI). One of the authors (DB) would also like to acknowledge the receipt of stipends from Wenner-Gren Foundations and The Royal Swedish Academy of Sciences.

References

[1] J. MacCallum, C. Vincent (eds.), *Polymer Electrolyte Reviews 1 and 2*, Elsevier, London, 1987.
[2] F. Gray, *Polymer Electrolytes*, The Royal Society of Chemistry, Cambridge, 1997.
[3] P. Bruce (ed.), *Solid State Electrochemistry*, Cambridge University Press, Cambridge, 1995.
[4] J.M. Tarascon, M.B Armand, *Nature*, 414 (2001) 359.
[5] W. van Schalwijk, B. Scrosati, *Advances in Lithium-Ion Batteries*, Kluwer Academic/Plenum Publishers, New York, 2002.
[6] M.B. Armand, *Polymer Electrolyte Reviews-1*, Ch. 1, Elsevier, London, 1987.
[7] Z. Gadjourova, Y.G. Andreev, D.P. Tunstall, P.G. Bruce, *Nature*, 412 (2001) 520.
[8] G.S. MacGlashan, Y.G. Andreev, P.G. Bruce, *Nature*, 398 (1999) 792.
[9] Z. Gadjourova, D. Martin y Marero, K.H. Andersen, Y.G. Andreev, P.G. Bruce, *Chem. Mater.*, 13 (2001) 1282.
[10] D. Brandell, A. Liivat, H. Kasemägi, A. Aabloo, J.O. Thomas, *J. Mater. Chem.*, 15 (2005) 1422.
[11] D. Brandell, A. Liivat, A. Aabloo, J.O Thomas, *Chem. Mater.*, 17 (2005) 3673.
[12] D. Brandell, A. Liivat, A. Aabloo, J.O. Thomas, *J. Mater. Chem.*, 15 (2005) 4338.
[13] A.M. Christie, S.J. Lilley, E. Staunton, Y.G. Andreev, P.G. Bruce, *Nature*, 433 (2005) 50.
[14] C. Zhang, E. Staunton, Y.G. Andreev, P.G. Bruce, *JACS*, 127 (2005) 18305.
[15] Z. Stoeva, I. Martin-Litas, E. Staunton, Y.G. Andreev, P.G. Bruce, *JACS*, 125 (2003) 4619.

[16] A. Liivat, D. Brandell, J.O. Thomas, *Submitted to Electrochimica Acta*.
[17] S. Neyertz, D. Brown, J.O. Thomas, *J. Chem. Phys.*, 101 (1994) 10064.
[18] O. Borodin, G.D. Smith, *J. Phys. Chem.*, B 107 (2003) 6801.
[19] F. Müller-Plathe, *Acta Polymer.*, 45 (1994) 259.
[20] O. Borodin, G.D. Smith, R.L. Jaffe, *J. Comput. Chem.*, 22 (2001) 641.
[21] O. Borodin, G.D. Smith, *Macromolecules*, 33 (2000) 2273.
[22] O. Borodin, G.D. Smith, *Macromolecules*, 31 (1998) 8396.
[23] A. Liivat, A. Aabloo, J.O. Thomas, *J. Comput. Chem.*, 26 (2005) 716.
[24] W. Smith, T. Forester, *The DL_POLY project.*, Technical report, TCS Division, Daresbury Laboratory, Daresbury, Warrington, WA4 4AD, UK. Warrington, WA4 4AD, UK.
[25] E. Staunton, Y.G. Andreev, P.G. Bruce, *Faraday Discuss.*, 134 (2007) 143.
[26] Y. Takahashi, H. Tadokoro, *Macromolecules*, 6 (1969) 672.
[27] W.A. Henderson, N.R. Brooks, V.G. Young, *Chem. Mater.*, 15 (2003) 4685.
[28] A. Bhattacharyya, J. Fleig, Y.G. Guo, J. Maier, *Adv. Mater.*, 17 (2005) 2630.
[29] D. Brandell, *Understanding Ionic Conductivity in Crystalline Polymer Electrolytes*, Ph.D. thesis, Uppsala University, 2005.